TABLE OF CONTENTS

LIST OF TABLES

LIST OF FIGURES

XX

LIST OF ABREVIATIONS

ABD	Laminate Stiffness Matrix
AClass	A Class Catamaran
AC Class	Americas Cup Class Catamaran
ASTM	American Society for Testing and Materials
AR	I-Beam Aspect Ratio
BM	Bending Moment
$°C$	Celsius Degree
CAD	Computed Aided Design
CAE	Computed Aided Engineering
CFD	Computational Fluid Dynamics
CClass	C Class Catamaran
CFRP	Carbon Fiber Reinforced Polymer
CLT	Classic Laminates Theory
CREPEC	Research Center for High Performance Polymer and Composite Systems
DOF	Degrees Of Freedom
ETS	École de Technologie Supérieure
FBD	Free Body Diagram
FEM	Finite Element Model
FEA	Finite Element Analysis

FHNW	University of Applied Sciences and Arts Northwestern Switzerland
FI	Failure Index
GUI	Graphical User Interface
GBE	Generalized Beam Element
IKT	Institute of Polymer Engineering
IPPE	Institute for Product and Production Engineering
kt	Knots (wind or boat speed)
NASA	National Aeronautics and Space Administration
NiTi	Nickel Titanium Alloy
NiTiNOL	Nickel Titanium-Naval Ordnance Laboratory
Nm	Newton-Meter (bending moment)
OOA	Out Of Autoclave
PCP	Proof of Concept Prototype
PD	Proposed Design
SC	Safety Coefficient
SL	Shear Load
SMA	Shape Memory Alloy
SME	Shape Memory Effect
SEE	Superelastic Effect
TFW	The Foiling Week
UI	User Interface

LISTE OF SYMBOLS AND UNITS OF MEASUREMENTS

[A]	N/m	Laminate tension stiffness matrix
A_{ij}	N/m	Laminate tension stiffness matrix element
A_s	$°C$	SMA Austenite transformation start temperature
A_f	$°C$	SMA Austenite transformation final temperature
$[B]$	N	Laminate coupling matrix
B_{ij}	N	Laminate coupling matrix element
C_L	$-$	Airfoil Lift coefficient
C_D	$-$	Airfoil Drag coefficient
[D]	Nm	Laminate bending matrix
D_{ij}	Nm	Laminate bending matrix element
d_{crew}	m	Sailing crew lever length
ε	mm/mm	Strain
ε_{sma}	mm/mm	SMA member strain
E_1	N/m^2	Fiber orientation tensile modulus (0°)
E_2	N/m^2	Transverse fiber orientation tensile modulus (90°)
E_{fx}	N/m^2	CFRP Flexural modulus on x direction
E_{sma}	N/m^2	SMA elastic modulus
EI	Nm^2	Bending stiffness
$\widehat{EI}_{beam}$	Nm^2	Beam bending stiffness

$\widehat{EI}_{cfrp}$	Nm^2	CFRP bending stiffness
$\widehat{EA}$	N/m^2	Composite beam equivalent tensile stiffness
$\widehat{EA}_{cfrp}$	N/m^2	Composite beam tensile stiffness
G_{12}	N/m^2	1-2 direction Shear Modulus
F_x	N	Force in x component
F_y	N	Force in y component
F_z	N	Force in z component
F_c	N	Force acting on the centerboard
F_{crew}	N	Gravitational force of the sailing crew
F_w	N	Force of the wind
F_{sma}	N	Force on SMA member
f_w	m	I-Beam flange width
f_l	m	I-Beam flange length
h_w	m	Wind force lever height
h_c	m	Centerboard lever height
h	m	Distance between SMA and CFRP Neutral Axis
I_x	mm^4	Second moment of inertia
k_x	Nm	Spring constant around x component
κ_x	m^{-1}	Curvature around x component
L_{cfrp}	m	CFRP member length in compliant Beam

L_{sma}	m	SMA member length in compliant Beam
M_s	$°C$	SMA Martensite transformation start temperature
M_f	$°C$	SMA Martensite transformation final temperature
M_{Beam}	Nm	Bending Moment applied to a Beam
M_{cfrp}	Nm	Bending Moment applied to CFRP member
M_{sma}	Nm	Bending Moment applied to SMA member
M_x	Nm	Moment in x component
M_y	Nm	Moment in y component
M_z	Nm	Moment in z component
N_{cfrp}	N	Applied force on CFRP member
ν_{12}	$-$	Lamina Poisson ratio in 1-2 direction
$Ratio_{sma}$	mm/mm	Relation between L_{sma} and L_{cfrp}
σ_{sma}	MPa	Constraint on SMA
S_{sma}	m^2	SMA member section area
$\sigma_{x,y}$	MPa	Constraint on x,y orientations
$\sigma_{1,2}$	MPa	Constraint on $1,2$ orientations
S_L^-	MPa	Failure stress in Compression in σ_1 direction
S_L^+	MPa	Failure stress in Tension in σ_1 direction
S_T^-	MPa	Failure stress in Compression in σ_2 direction
S_T^+	MPa	Failure stress in Tension in σ_2 direction

w_t	mm	I-Beam web thickness
w_z	mm	Displacement in z component direction
$\bar{y}$	mm	Distance from Neutral Axis of Beam element
$\bar{y}_{sma}$	mm	Distance from Neutral Axis to SMA member

INTRODUCTION

Traditionally, sailboats relied on the *Archimedes principle* to move on the water surface. This method has been used and successfully proven for many thousands of years, with the earliest known depiction found on an Egyptian clay and dating from around 3100 B.C. This civilization used the force of the wind as one of their methods for powering their vessels and move along the Nile river (Figure 0.1).
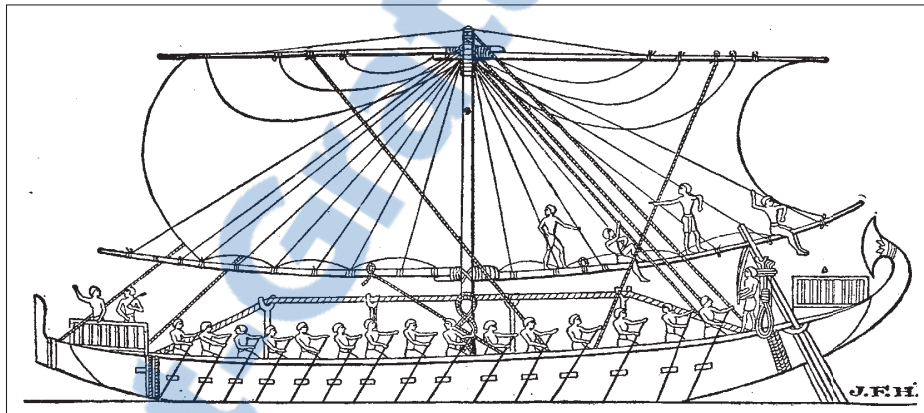
Figure 0.1   Egyptian ship on the Red Sea (1250 B.C.)
Image from Torr's "Ancient Ships"

With the advancement of technology and the vast historical experience, yacht designers and engineers have been developing more refined structures to increase the efficiency of sailing vessels by reducing the hydro-dynamic resistance of the hulls and appendages in contact with the water (Figure 0.2a).

In the past decades, the concept of sailing has changed drastically. The Archimedes principle is no longer the only responsible for keeping a boat afloat. By using aerospace design and manufacturing techniques, as well as implementing an airplane-like concept, nowadays, the most efficient and fastest sailboats are able to *"fly"* above the water surface by the means of *hydrofoils*.

A *hydrofoil* is a wing-like structure whose objective is to increase a boat efficiency. With this kind of appendage, a boat will go from a traditional *Archimedean* mode at low speeds, to a "flying" *Foiling* mode at higher speeds. These two states depend strongly on the design characteristics of the boat and hydrofoils. During the 34th *Americas' Cup* in 2013, the word *foiling* became a common term in the sailing community. With impressive 22 meter long ($\approx$ 72ft.) catamarans, strongly inspired by *CClass Catamarans* design, achieving speeds of up to 81 km/h ($\approx$ 45 kt.), it was proven that *foiling* was the most efficient way for a vessel to move.

| a) Refitted J-Class boat from 1930 | b) ETNZ - 35th America's Cup 2017 |
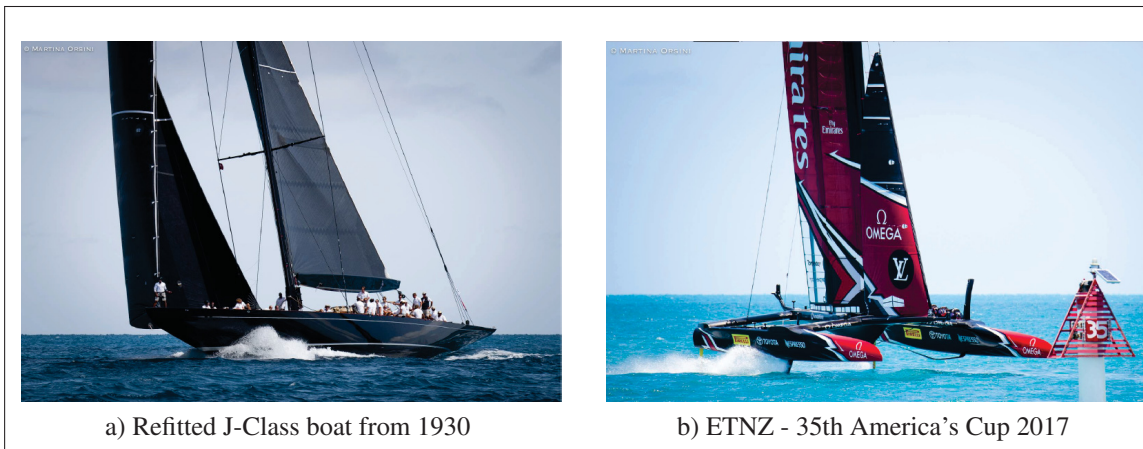
Figure 0.2   America's Cup evolution, from $1930's$ J-Class to 2017 ACC
Images from Martina Orsini, using with authorization

The *foiling* principle can be explained by using the airplane principle analogy. While taxiing on the runway before take-off at lower speeds, an airplane relies on its wheels to move, since higher speeds are needed for the wings to generate lift. As the speed increases, the weight of an airplane is gradually transferred from the landing gear to its wings until it leaves the ground. Using a similar principle, a hydro-foiling boat will rely on its hulls when moving at low speeds, applying the *Archimedes* principle, and when the speed is increased, these *wing-like* structures are capable of producing enough vertical lift to keep the hulls of the sailboat above the water surface, and with this, drastically reduce the drag created by the *water-hulls* interface. This sailing state is commonly known as *Foiling*.

Airplanes, in their majority, have the capacity to adjust their speed by the means of the engines, but on a sailboat, the boat speed is directly related to the speed of the wind. When sailing on a light breeze day, *hydrofoils* are unable to generate the necessary vertical lift to release the hulls from the water surface. In this case the section of the *hydrofoils* responsible to generate the vertical lift is useless and generates unnecessary drag, reducing the overall efficiency of the sail-boat.

The objective of this work is to propose a hydrofoil concept capable of passively adapting its geometry to increase the overall efficiency of sailing catamarans at different sailing conditions. This deformations' goal is to increase the lift to drag ratio depending on the boat *speed (V)* and hydrofoil *loading (L)*. The compliance on the hydrofoil structure will be possible by the means of *Shape Memory Alloys (SMA)* to achieve a *passively controlled non-linear deformation*, as seen on Figure 0.3, where the structure will go from an unloaded state (1), to a lightly loaded state in (2) while accelerating, then deforming significantly at a specific loading state (3), and finally achieving a *Foiling* state at high bending loads on (4).
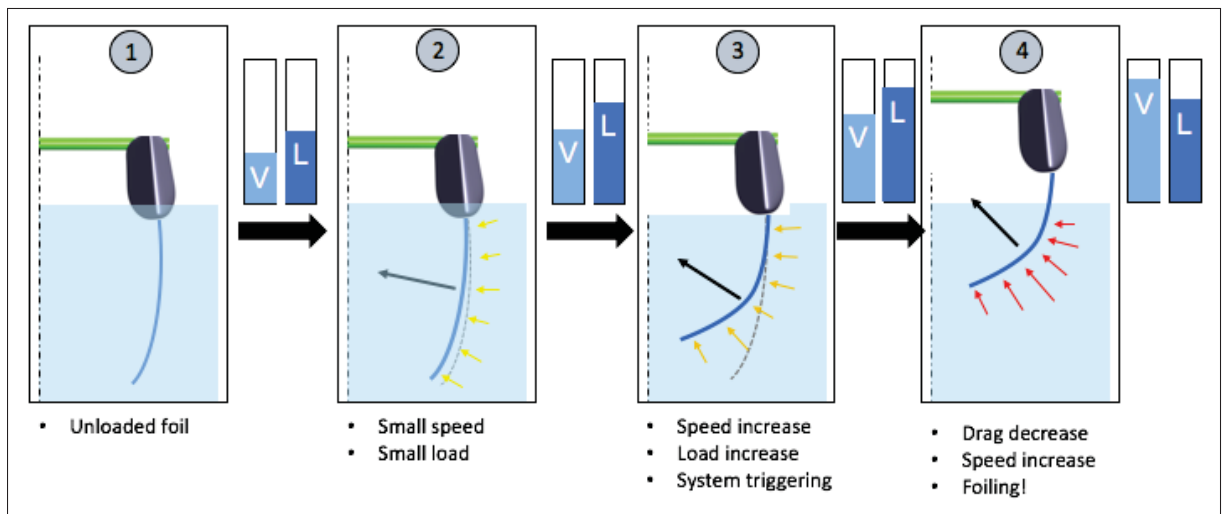
Figure 0.3 Geometrical evolution of Non-Linear Compliant hydrofoil

To achieve the main goal of developing a passive non linear compliant hydrofoil, three intermediate objectives were defined. The first one being the development of a non-linear beam model representing the internal hydrofoil structure to evaluate the hydrofoils global behaviour under a hydro static load. Continuing with the design and evaluation of a structure capable of achieving large deformations representing the hydrofoils passive non-linear compliant section. And finally the manufacturing and testing of a section prototype to validate the theoretical calculations.

The study was conducted with the geometry and load-case boundary conditions of an AClass catamaran. This single handed 18 footer ($\approx$5.49 m.) sailing catamaran is one of the most popular *open* development class, where professional and amateur sailors compete with fully customized systems to increase the technical performances while respecting the restrictive rules. This kind of boat was chosen for the potential small scale application, and the challenging class rules (ISAF, 2010). Therefore, all the design parameters used in this thesis are in the magnitude of such vessels, nonetheless, the presented methodology could be generalized and potentially used for different load-cases and geometries.

This thesis is sub-divided in four chapters, allowing to articulate the work to achieve a *Passive-Selective Non-Linear Compliant Hydrofoil* designed and tested prototype section, as well as a proposed hydrofoil conceptual design.

A literature review is presented in Chapter 1, where the sailing notions and terms, the *hydrofoil* principle and a synthesis of a variety of *non-linear compliant* structures are described, as well as the technical references needed to complete this work.

In Chapter 2, the load-case, the design envelope and the assumed boundary conditions for the study are presented, along with the developed tools and models for a preliminary design. These scripts were used to develop the *Proof of Concept Prototype (PCP)* and *Proposed Design (PD)*, described and explained in Chapters 3 and 4.

The 3rd Chapter describes the full design process on the design, manufacturing and testing of the *Proof of Concept Prototype (PCP)*, as well as the comparison between the calculated and experimental results. Finally, in Chapter 4, an *AClass* catamaran hydrofoil *Proposed design (PD)* is presented.

Following to this last chapter a conclusion where the practical appreciation of the work and potential next steps to develop a functional *Non-Linear Compliant hydrofoil* structure are discussed.

This work was accomplished in parallel to the EHYCOMP project from FHNW, whose aim is to optimize the performances of sailing catamarans by using non-linear compliant structures for hydrofoils.

CHAPTER 1

LITERATURE REVIEW

The conducted review of concepts and literature in this chapter aims to present the basic theoretical background needed to understand this work, focusing on the principles of hydrofoils, morphing structures and Shape Memory Alloys.

1.1 The physics of sailing

Sailing can be defined as moving by the means of the power of the wind. Usually, the term is related to *sailboats* (Fig. 1.1a), moving on the water surface. Some other concepts moving on hard surfaces, such as *iceboats* (Fig. 1.1b) and *sailcars or windbuggys* (Fig. 1.1c) also exist. The physics principles allowing these vehicles to function using the power of the wind, remain identical in all cases. This review of concepts will focus on the sailboats, most precisely on the classical displacement boats, depending exclusively on the *Archimedes* principle to remain afloat, and the ones using *hydrofoils*.

a) Sailboat   b) Iceboat   c) Sailcar

Figure 1.1   Illustrations of sailing crafts
Images from *Wikipedia.com*

1.1.1 Displacement boats

Archimedean or *Displacement* boats rely on the principle of buoyancy, derived form the *Archimedes* Principle and the static equilibrium of forces, where the *Buoyancy* force is expressed in equation 1.1 and illustrated on Figure 1.2.

$$Buoyancy_{force} = \rho_{fluid} \; x \; Gravity \; x \; Volume_{displaced} \tag{1.1}$$
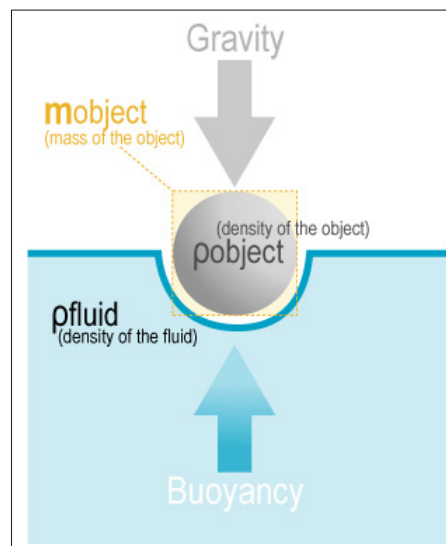
Figure 1.2   Buoyancy principle
Image adapted from wikidot.com

On any conventional boat, the *buoyancy* is obtained by the hull or hulls, depending on the configuration of the vessel. The case of a *sailboat* is no different, and it is mainly composed by four elemental parts, as shown on Figure 1.3 where an *Optimist* dinghy, the most popular sailboat for kids competition is illustrated. Starting with the *Hull (1)* responsible to generate the needed Archimedean lifting force to stay afloat, the *Sail (2)*, used to exploit the wind energy, the *Rudder (3)*, an articulated surface to control the boat direction on the water plane and finally the *Centerboard (4)*, a fixed surface resisting the side force generated by the sail.

a) Optimist illustration   b) Optimist Sailing
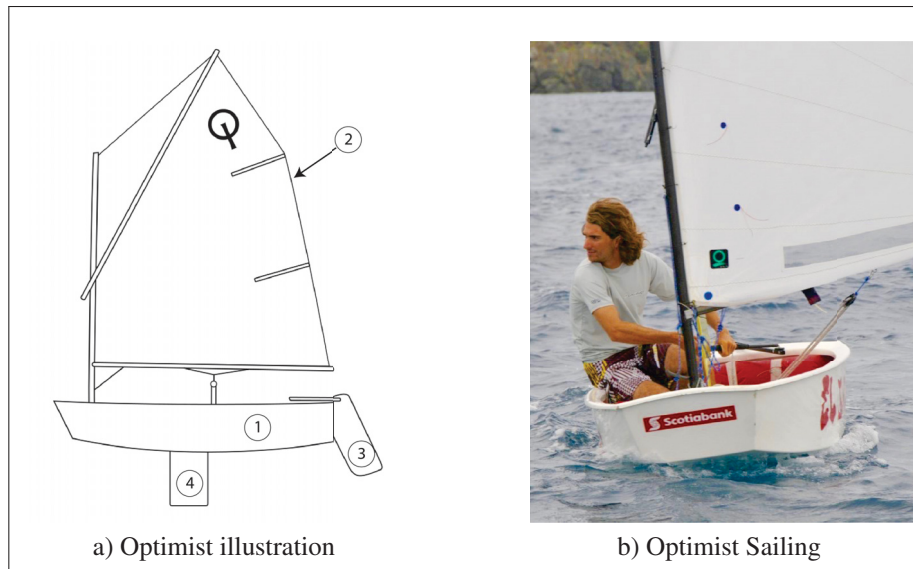
Figure 1.3   Optimist sailboat

The simplified forces acting on an *Archimedean* sailboat can be seen on Figure 1.4, where the equilibrium is achieved by the forces and levers acting on the boat. The wind and centerboard forces contribute for the *heeling moment* $(H_m = F_w\ h_w + F_c\ h_c)$ and the *crew weight* for the *righting moment* $(R_m = F_{crew}\ d_{crew})$ of the boat. These two being opposite, the greater the *Righting moment*, the greater the boatspeed. Since the weight of the sailor remains constant, his role is to maneuver the sails and boat direction to maximize the R_m in all sailing conditions.
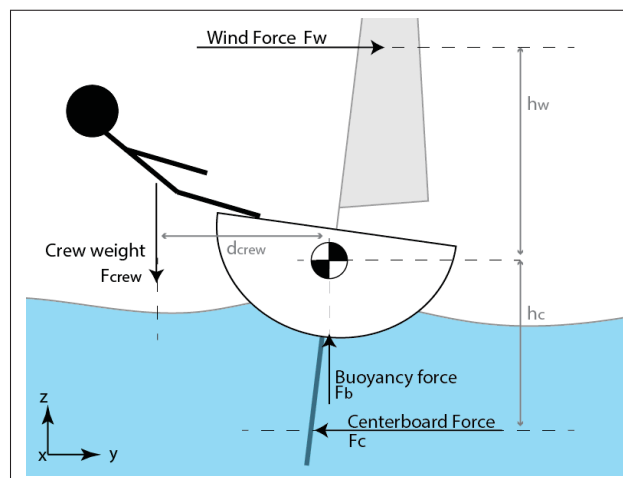
Figure 1.4   Simplified illustration of a sailing
boat, the acting forces and levers

The equilibrium of a sailing boat can be expressed as seen in equation 1.2, where the sum of moments around the *x* axis passing through the centre of gravity of the boat should always be 0 for the boat to remain afloat and avoid capsizing.

$$\sum M_x = 0 \Rightarrow \sum M_x = F_{crew}\, d_{crew} - F_w\, h_w - F_c\, h_c = 0 \qquad (1.2)$$

1.1.2 Hydrofoils

Hydrofoils are used to reduce the overall friction between the hull and the water. This is achieved by lifting the boat above the water surface at high speeds with wing-like structures. The concept was developed in the $1950's$ and used mostly in commercial and military engine powered vessels, like the *Spaviero Class* patrol boat, designed by the Italian Navy (See Figure 1.5) to move at high speeds to defend the Adriatic and Mediterranean sea coasts. The goal of this concept is to achieve high speeds with a greater stability and control. By eliminating the *hull-water* interaction the drag is then reduced and so is the needed energy to displace the vessel, eliminating the influence of waves on the vessel also provides a much stable displacement.

Figure 1.5   Hydrofoiling *Spaviero* military vessel
Image from www.boatdesign.net

Analog to airplane wings, *hydrofoils* only function above certain speeds, as the produced *Lift* force *L* is a direct function of the square of the speed (v), the airfoil lift coefficient C_L, the wing area A_w, and the fluid density ρ as expressed on the *Bernoulli* principle derived *Lift* equation (see eq.1.3).

$$L = \frac{1}{2} C_L \, \rho \, v^2 \, A_w \qquad (1.3)$$

Along with the *Lift*, the *Drag* or resistance to movement is also a factor to consider. Equation 1.4, where *D* is the *Drag* force and C_D the drag coefficient, expresses the resultant resistance that a defined area *A* at a certain speed *v* will create. With this relation, it becomes obvious that the smaller the area in contact with the fluid, the smaller the drag.

$$D = \frac{1}{2} C_D \, \rho \, v^2 \, A_w \qquad (1.4)$$

In the case of a vessel with *hydrofoils*, when moving at low speeds the Archimedes principle is still necessary to create the needed buoyancy and remain afloat. Once the higher speeds are achieved, the hydrodynamic *drag* is reduced and *lift* increased, allowing the vessel to achieve even higher speeds with less energy. A *Drag vs. Speed* correlation for the *Displacement* and *Foiling* cases is shown on Figure 1.6.
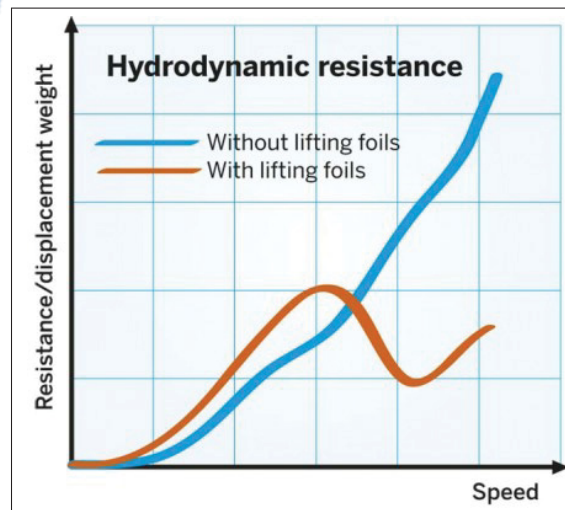
Figure 1.6   Speed vs. drag displacement
and hydrofoiling comparison
Image from http://www.yachtingworld.com

After the 34th *Americas Cup* in 2013, many different concepts of hydrofoils became popular, from *self stable* geometries like the *L, V, J*, to the *assisted* concepts, like the popular *T foil* concept. This geometry is widely used on the *Moth* international class, as seen on Figure 1.7. This system uses a *wand* that senses the height of the boat hull to the water and acts directly on the *T foil* flap, increasing and decreasing the lift as needed.

Figure 1.7   Foiling Moth
Image from Martina Orsini

Some catamarans, like the *Stunt S9* also use this system to control the boat height and achieve stable *foiling*. In this case four supports are used, meaning that the two main foils and the two rudders remain always in the water. This is caused by the fact that catamarans are composed by two hulls, and the system is then doubled. The *wand* of the *Stunt S9* can be seen on Figure 1.8, beneath the number "89" on the hulls.

Figure 1.8   *Stunt S9* Catamaran foiling
Image from Martina Orsini

Continuing with foiling catamarans, some concepts using a three foil support are found, and their nomenclature refers to the structural geometry expressed by a *Letter*, as seen on Figure 1.9. Each of these concepts benefit from totally different *Resultant Forces (RF)* and foiling capabilities.
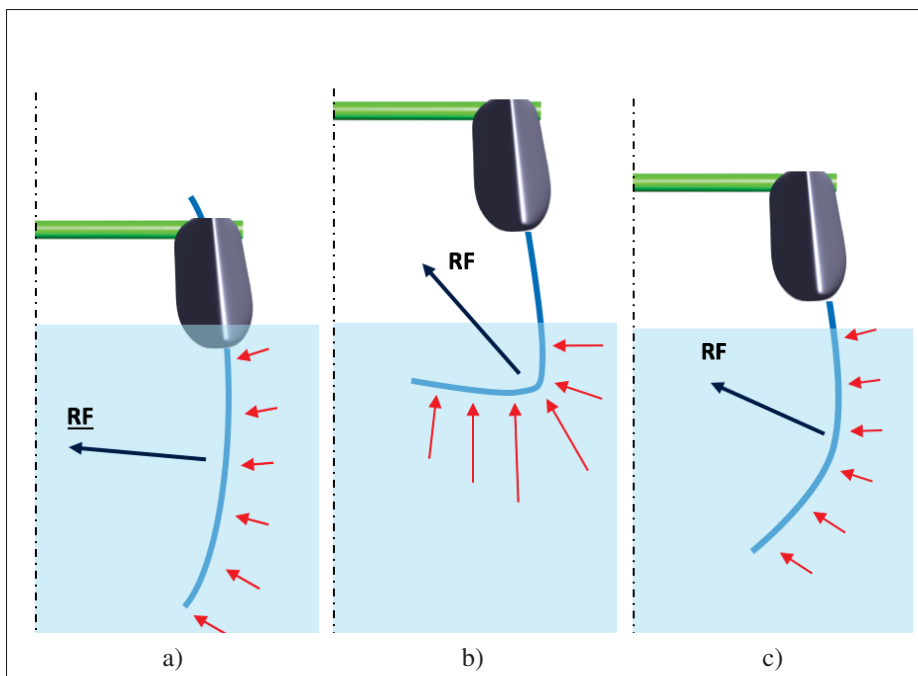
Figure 1.9   Popular hydrofoil geometries on sailing catamarans
(a) C Foil, (b) L/V Foil, (c) J/Z Foil

Beginning with the *C Foils* on Figure 1.9a, this concept generates mostly a sideforce as the *Resultant Force*, provides a small amount of vertical lift. While this kind of appendage is not considered as a *hydrofoil*, it allows to reduce the interaction between the *hull* and the water. Continuing with the *L/V* foils on Figure 1.9b, these geometries are widely used on *CClass*, *Americas Cup Class* and *GC32* catamarans. The geometry provides the necessary lift to allow the boat to *foil* when the needed boat speed is present. Because of its composition, this kind of hydrofoil can be subdivided in three parts, being the *Main Foil (1)*, the *Elbow (2)* and the *Tip (3)*, as seen on Figure 1.10b. The great advantage of this geometry is that it is self-stable, meaning that if too much lift is produced, the hydrofoil tip will pierce the water and by that, the *hydrofoil* surface area in contact with the water will be reduced, ergo the *lift* is reduced.

A clear example of *water-piercing* can be seen on Figure 1.10 where a *GC32* foiling catamaran can be seen at Lake Garda during the *Foiling Week 2016*.
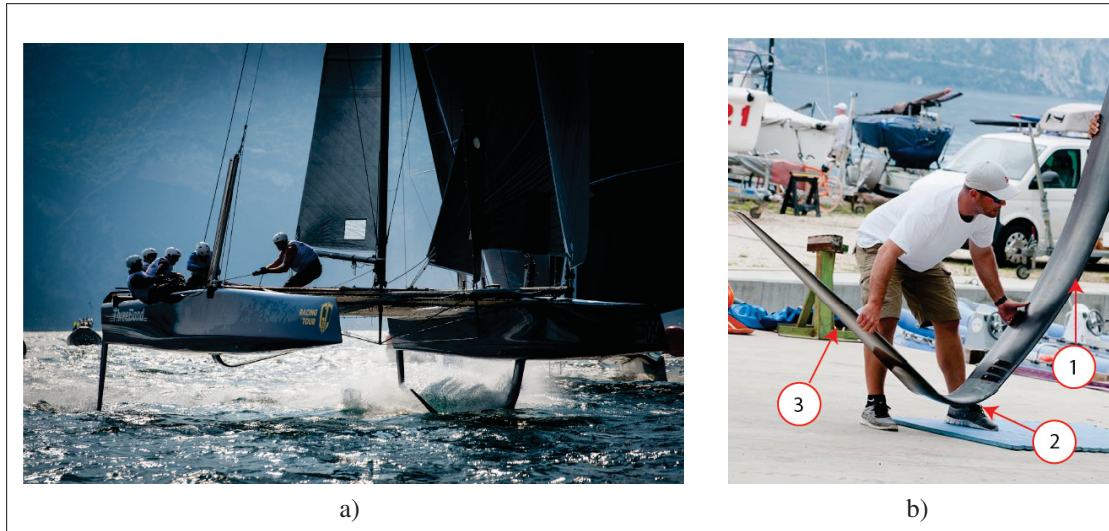
Figure 1.10   GC32 Sailboat
(a) Foiling in Lake Garda, (b) L/V Hydrofoil; Image from Martina Orsini

The last presented geometry on this review is the *J/Z* hydrofoil on Figure 1.9c. This concept is mostly used in *AClass* catamarans (see Figure: 1.11) and comes from a compromise between the *C and L/V* geometries, because the class regulations (ISAF, 2010) only allow a limited design bounding box. The downside of this geometry is that the foiling stability depends greatly on the skipper abilities.

Figure 1.11   Sergio Mehl foiling on DNA AClass
Image from *www.catsailingnews.com*

1.2   Materials

The materials used in this work, are mainly *Carbon Fiber Reinforced Polymers (CFRP)* widely used on lightweight structures and *Shape Memory Alloys (SMA)*, a metal alloy that has interesting elastic properties, used on many actuator concepts and large deformation structures.

1.2.1   Carbon Fiber Reinforced Polymers (CFRP)

Carbon fiber reinforced polymers are broadly used on lightweight structures, as seen on Figure 1.12. This composite material obtained by combining a polymer matrix with a carbon fibers, provide great mechanical properties that would not be possible individually in tension and compression, as well as an accessible manufacturing process by molding and *curing* the polymer at relatively low temperatures $(20 - 180°C)$.
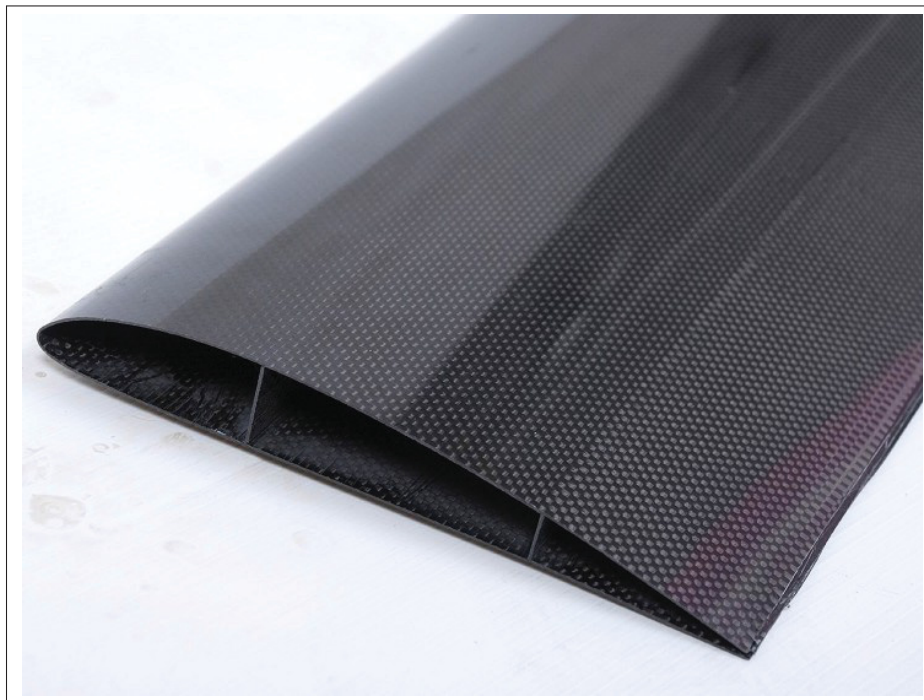
Figure 1.12   Model Airplane lightweight carbon fiber-epoxy wing
Image adapted from www.rcgroups.com

1.2.2 Shape Memory Alloys

Shape Memory Alloy is a highly non-linear thermo-dependent material that has the ability of recovering its original state after experiencing a large deformation. This behavior is possible thanks to a multiple state crystal transformation from Austenite to Martensite (Rao, 2015), as shown on Figure 1.13.
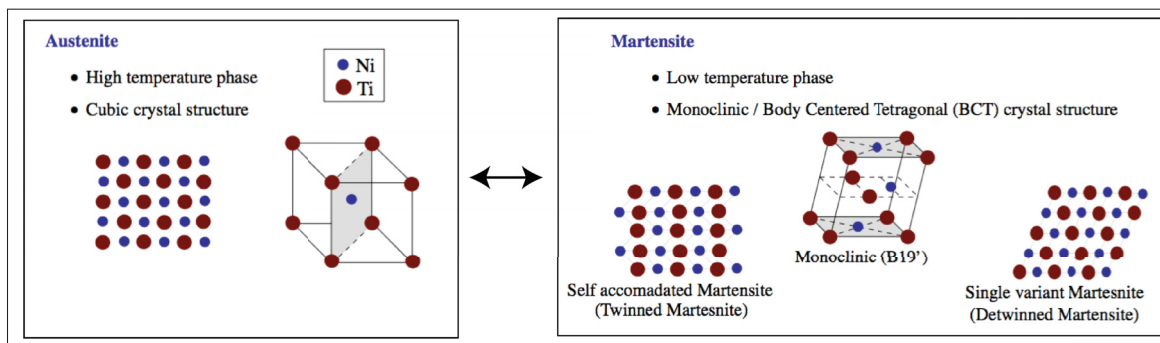
Figure 1.13   SMA phase transformations
Image adapted from (Rao, 2015)

Along with its thermal dependency, *SMA* have a strong rate-dependency as well as loading/un-loading hysteresis (Rao, 2015). Commercially, the most common SMA is *NiTiNOL*, composed in its majority out of a Nickel (Ni) and Titanium (Ti) alloy with almost a *50-50* composition. The name *NiTiNOL* refers to the alloy composition itself and the site of discovery, being **Ni**ckel-**Ti**tanium **N**aval **O**rdonance **L**aboratory.

Depending on the material properties and operation environment, SMA's can be subdivided in two categories:

Shape Memory Effect (SME) - This kind of SMA has the ability to be easily deformed at a low temperature, maintaining the strained deformed state until exposed to a high temperature, at which the material recovers its initial *memory* shape. Most SMA actuators are based on the *Shape Memory Effect*, using an external source of energy and applying the *Joule Effect* to achieve actuation (Rao, 2015) (Barbarino *et al.*, 2014).

Super Elastic Effect (SEE) - When the temperature is kept above *Austenite Final (Af)*, as seen on Figure 1.14, the material will behave as a non-linear spring when loaded, recovering its initial *"memory"* state and geometry when the load is removed. This kind of *SMA* is commonly used in many metal frame reading glasses, allowing high elastic deformations.
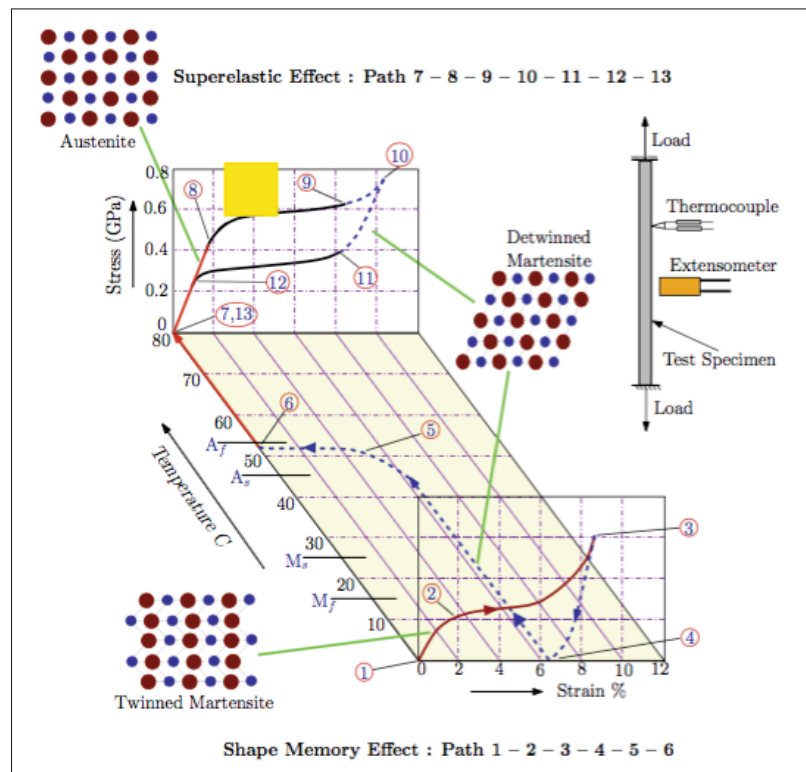
Figure 1.14   SMA behavior and temp. dependency
Image adapted from (Rao, 2015)

The heat operation temperatures of *SMA* can drastically vary depending on their composition and specific treatment. Because of its thermal sensitivity and rate-dependency, most often than not, the material properties are not provided by the manufacturer as the material behavior can dramatically change at different operation and testing conditions. Instead, an approximate range of operation is given as a reference for a general choice, to which follows an exhaustive material characterization process.

1.3 Morphing Structures

Because of its versatility, morphing structures are widely used in the aerospace industry. Airplanes use wing flaps to circumstantially change the aerodynamic properties at different flying stages, as shown on Figure 1.15.

Figure 1.15   Deployed wing flaps on Boeing 757

When taking-off, with low ground speeds, a high lift coefficient is needed on the wings to put the plane in the air. Therefore, by deploying the flaps, pilots increases the wing surface and lift coefficient, to provide the necessary vertical force to take-off. When cruising, at $10,000m$ and high speeds, a large wing surface is no longer needed and the flaps get retracted, keeping a wing geometry that is as efficient as possible for those conditions.

Most of these systems, found on commercial aircraft rely on hinges, guiding tracks and hydraulic actuators to deploy the flaps and modify the wing geometry. These mechanism generates noncontinuous geometries inducing efficiency loss by disturbing the airflow and boundary layer on the airfoil. In the idea of creating a much more compact and *seamless* continuous system, multiple concepts are being developed, where the actuation is embedded into the into the airfoil, like the proposed concept from *FlexFoil* on Figure 1.16, taking advantage of new technologies and materials.

Figure 1.16   FlexFoil technology on wing
Image from www.flxsys.com

1.3.1   Embedded SMA concepts

Most morphing concepts using *Shape Memory Alloys* for actuation purposes, require an electronic active control and an external electric power source to provide the temperature by the *Joule Effect* to function. The concept presented by (Quintanilla, 2016) on his *Ph.D.* thesis proposes a morphing wing flap with embedded *Shape Memory Effect* SMA into an *APA-6* thermoplastic structure channels. This idea uses two wires on the top and bottom side of the flap to generate an induced deflection and change the geometry, as seen on Figure 1.17a. In this case, the deflection is generated by the moment $[M]$ created by the force $[F]$ on the wire and the distance $[d]$ above the neutral axis of the flap. On Figure 1.17b, a sketch shows the *heating/cooling* principle of the concept to achieve the desire flap deflections.

a) Morphing flap with embedded SMA   b) Flap heating/cooling principle
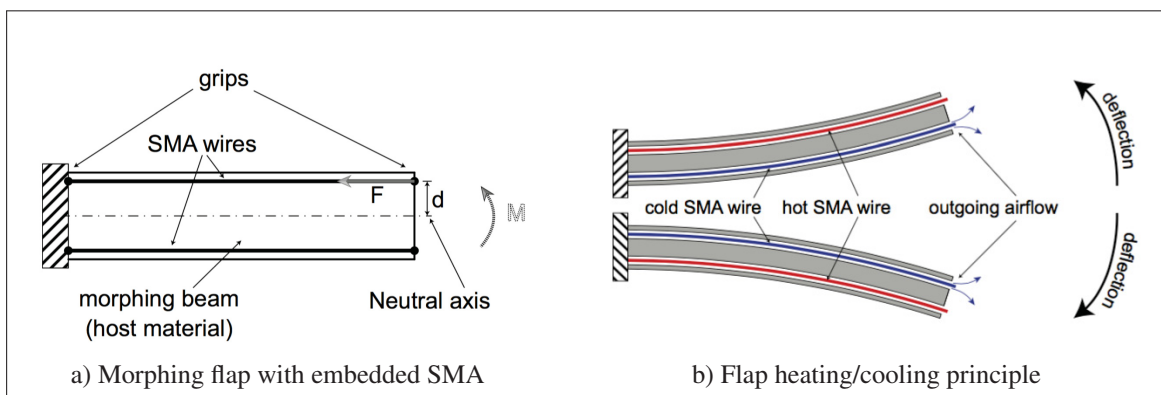
Figure 1.17   Morphing flap with embedded SMA concept
Adapted image from (Quintanilla, 2016)

The validated *Proof of Concept* can be seen on Figure 1.18, where multiple steady positions were achieved to determine the maximum amplitude of the system, as well as the potential dynamic behavior.
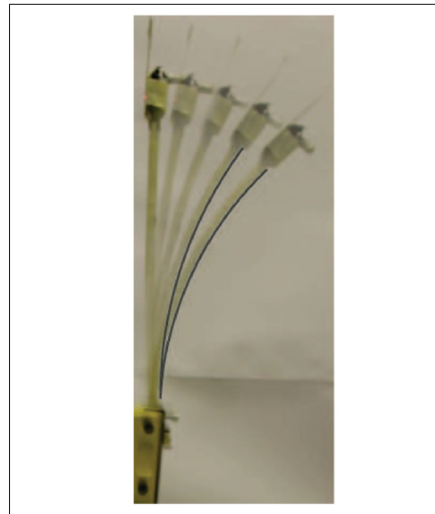
Figure 1.18   Morphing flap
proof of concept deflections
from Quintanilla (2016)

Another reviewed concept using embedded *SMA* was the one from (Brailovski *et al.*, 2010), where the *SMA* is used to move a slider inside the airfoil geometry and with it, change the *extrados* geometry. The conceptual sketch can be seen on Figure 1.19.
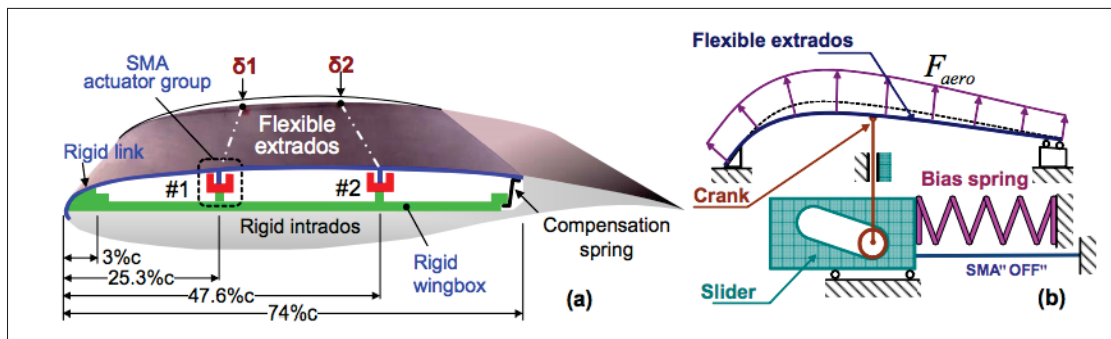
Figure 1.19   Morphing extrados concept
Adapted image form (Brailovski *et al.*, 2010)

Many similar concepts using the previously presented ideas are found in literature, from embedded wires into CFRP composites, to external action actuators. Since the goal of this work is to use the morphing system on an *AClass* catamaran, and the use of electric or electronic systems is not allowed by the rule (ISAF, 2010), these ideas were only used as potential references.

1.3.2   Passive morphing concepts

When revising the existing literature about passive actuation systems for airfoils, where the morphing is achieved by an external functional load, it was found that the examples are much fewer than for the active systems, presented earlier.

The *Laboratory of Composite Materials and Adaptive Structures* at *ETH Zurich* has developed many concepts for *aerospace* and *wind turbines* where the geometries change to modify the aerodynamic behavior of the wing under a defined load case. Three concepts are presented in this review, where the airfoil structural compliance is obtained by a load-dependent variable stiffness.

The first presented concept from Kuder *et al.* (2016) induces a large deformation on the airfoil structure by the means of bi-stable bending elements in between the profile spars. The conceptual model can be seen on Figure 1.20.
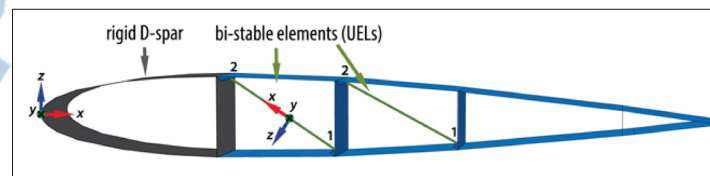
Figure 1.20   Passive morphing using bi-stable elements
Adapted image form (Kuder *et al.*, 2016)

Numerical and experimental results can be seen on Figure 1.21, where for the three load cases studied an induced large deformation on the airfoil is achieved by the deformation of the internal *bi-stable* elements.
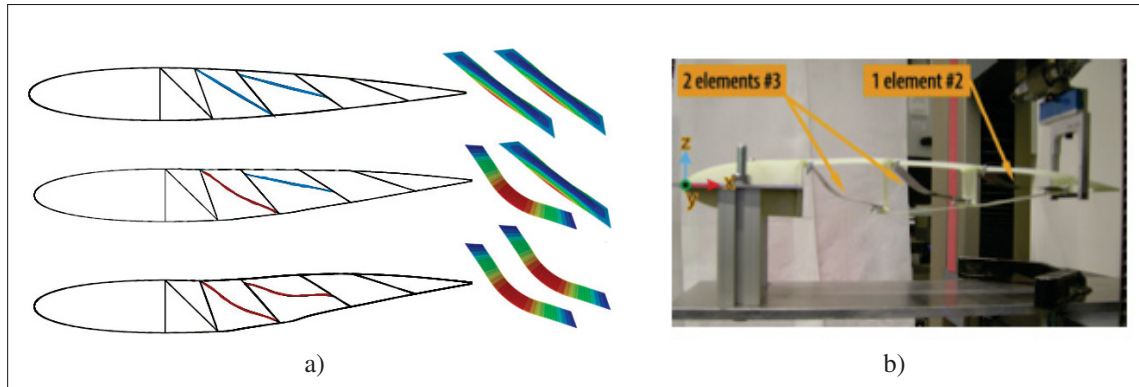
Figure 1.21   Passive morphing concept loading and deformation
(a) Numerical simulation, (b) Experimental testing
Adapted image from (Kuder *et al.*, 2016)

Runkel *et al.* (2016) propose a morphing concept, where the main wing spar *buckles* under load, inducing a twist along the wing span, as seen on Figure 1.22. This concept using the material instabilities is extremely interesting to modify a wing efficiency and avoid the aerodynamic overloading and failure of the structure.
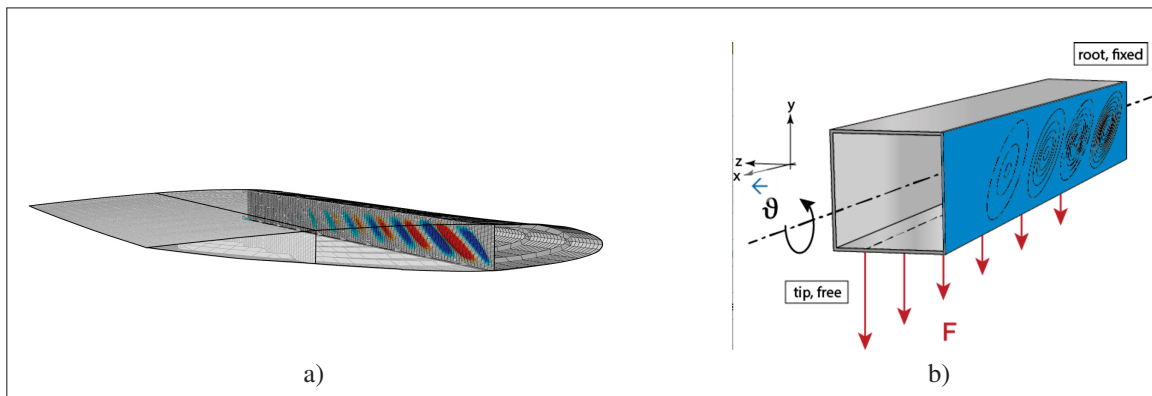
Figure 1.22   Passive twisting of composite beam structures
(a) Wing with buckling front spar, (b) Buckling induced twisting concept
Adapted image from (Runkel *et al.*, 2016)

The last reviewed concept is the one from Arrieta *et al.* (2014), where the aerodynamic load of a wind turbine is alleviated by passive morphing of the *blade*, as seen on Figure 1.23. Similar to the other ideas, the internal structure of the airfoil is designed to deform under load. The *initial* geometry being a highly cambered airfoil, with a *high C_L*, and in the case of a high

loading, the structure changes the geometry into a less cambered airfoil geometry, with a lower C_L generating a smaller *Lifting* force.
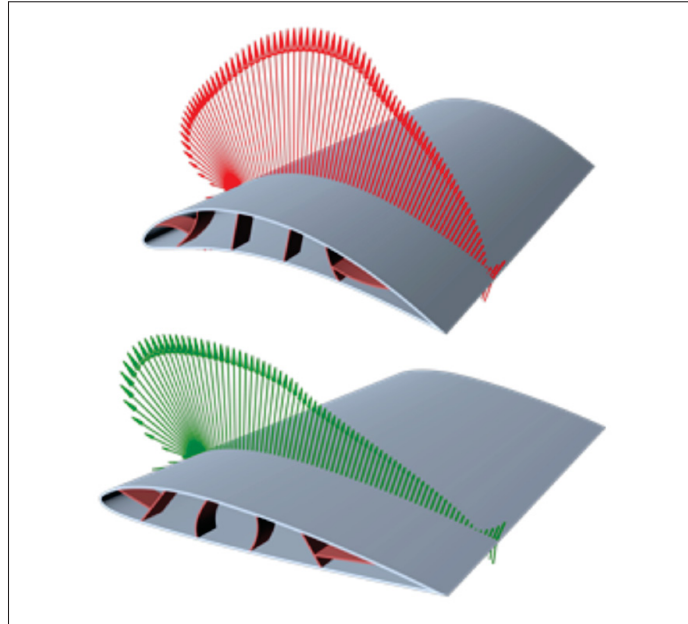
Figure 1.23   Passive load alleviation airfoil concept
Adapted image form (Arrieta *et al.*, 2014)

As seen on this literature review, many structural morphing concepts have been already developed for both active and passive control systems. While the use of embedded SMA for this kind of application is currently applied by an active control, the presented work proposes a methodology to define a morphing airfoil concept using embedded SMA to achieve passive-controlled deformations.

CHAPTER 2

METHODS AND METHODOLOGY

This chapter describes the tools used to design and analyse a *Passive-Selective Non-Linear Compliant Hydrofoil*. They were used to develop a *Proof of Concept Prototype (PCP)* and a complete hydrofoil *Proposed Design (PD)*. The chapter will first define the load case to which the structure was submitted, then will continue with the simplified geometry used for the prototype preliminary design study. Finally, a detailed description of the developed tools to achieve a time efficient design approach will be presented.

2.1 Load Case

The load case of the study is based on a J/Z hydrofoil for an *AClass* catamaran, designed by *Clemens Dransfeld, FHNW* and called *EH1*. The concept uses the maximized geometrical envelope allowed on the class rules, inspired by the most successful commercial *AClass* designs, such as *DNA* (Figure 2.1), *Scheurer G7* and *Exploder A13*.

Figure 2.1   Sergio Mehl foiling on DNA AClass with J/Z foils
Image from *www.catsailingnews.com*, using with authorization

The load evaluation was done by *F. Schadt* (Schadt, 2016) during his masters work at FHNW as part of the *EHYCOMP* project. The load-case presented is based on an *AClass* catamaran with two submerged hydrofoils, as most commercial *AClass* catamarans do, to develop the needed vertical lift and achieve a *Foiling* state.

The concept proposed in this thesis has the intention of using only one submerged hydrofoil to generate the needed vertical lift, as seen on Figure 2.2, a configuration adopted by many *CClass* and *America's Cup* catamarans. This would be possible by a large deformation on the hydrofoils lower section up to the tip, converting a hydrofoil from a *J/Z* to an *L/V* geometry.
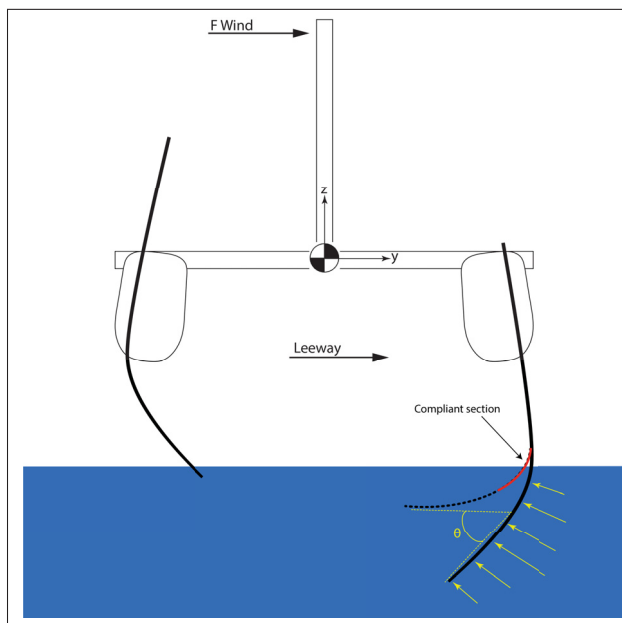
Figure 2.2 Single submerged Compliant hydrofoil on an AClass

Despite the fact that the concepts diverge from the fundamental application of two foils being submerged and sharing the vertical load to allow a *Foiling* state, joint decisions regarding the basic parameters were taken, allowing a maximum use of the calculated values for both studies. The overall geometrical boundaries, the hydrofoils geometrical sub-sectioning, and the boat-speeds, just to name a few, were defined based on average or commonly used values.

To begin with the hydrofoils load calculations, the minimum boat-weight allowed for racing along with *AClass* rules (75 *kg*) was used. The skipper weight, height and center of mass were considered to be the average of the population, being respectively 85 *kg*, 1.80 *m* and 1.10 *m*. The free body diagram of the boat and crew, with a general representation of the case-study loads can be seen on Figure 2.3.
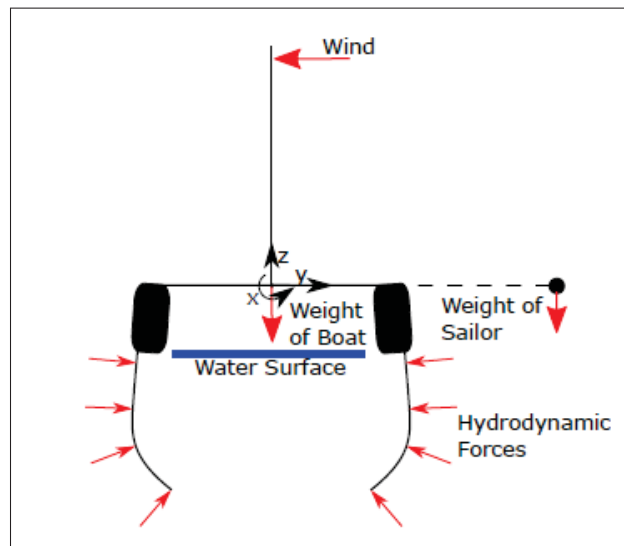
Figure 2.3   AClass with two submerged foils
Image from F. Schadt P8

The *EH1* hydrofoil on Figure 2.4, used for the load case study, was designed with a 1.3*m* span, a root and tip chords of 135*mm*, and 100*mm* respectively and a 10% overall profile thickness. It is composed by two airfoil profile geometries, being *HQ1510* profile from the hydrofoil root to the elbow, transitioning towards an *HQ3510* profile up to the tip. The choice of these profiles is a compromise between the *lift/drag* coefficients (Cl/Cd) of the sections and their purpose. In the case of a four supports foiling catamaran, the main foil section, where the low Cl/Cd *HQ1510* is used, should not create a great hydrodynamic lift because the opposite side foil would generate the same force in the opposite direction, needing for a stronger structure. On the tip side, the cambered *HQ3510* high Cl/Cd profile was chosen as both hydrofoils would collaborate mostly in the same z component direction.

To obtain the hydrodynamic forces acting on the *EH1* hydrofoil when submitted to different configurations, a Vortex-Lattice method model was developed using *Tornado*, a *MatLab* based scrip able to simulate 3*D* airfoils and wings. *MatLab* scripts were adapted and used to evaluate the different sailing scenarios, based on common situations for wind and boat speeds, as well as hydrofoils *foil-rake* and *leeway* angles to simulate the hydrofoils behavior as realistically as possible.
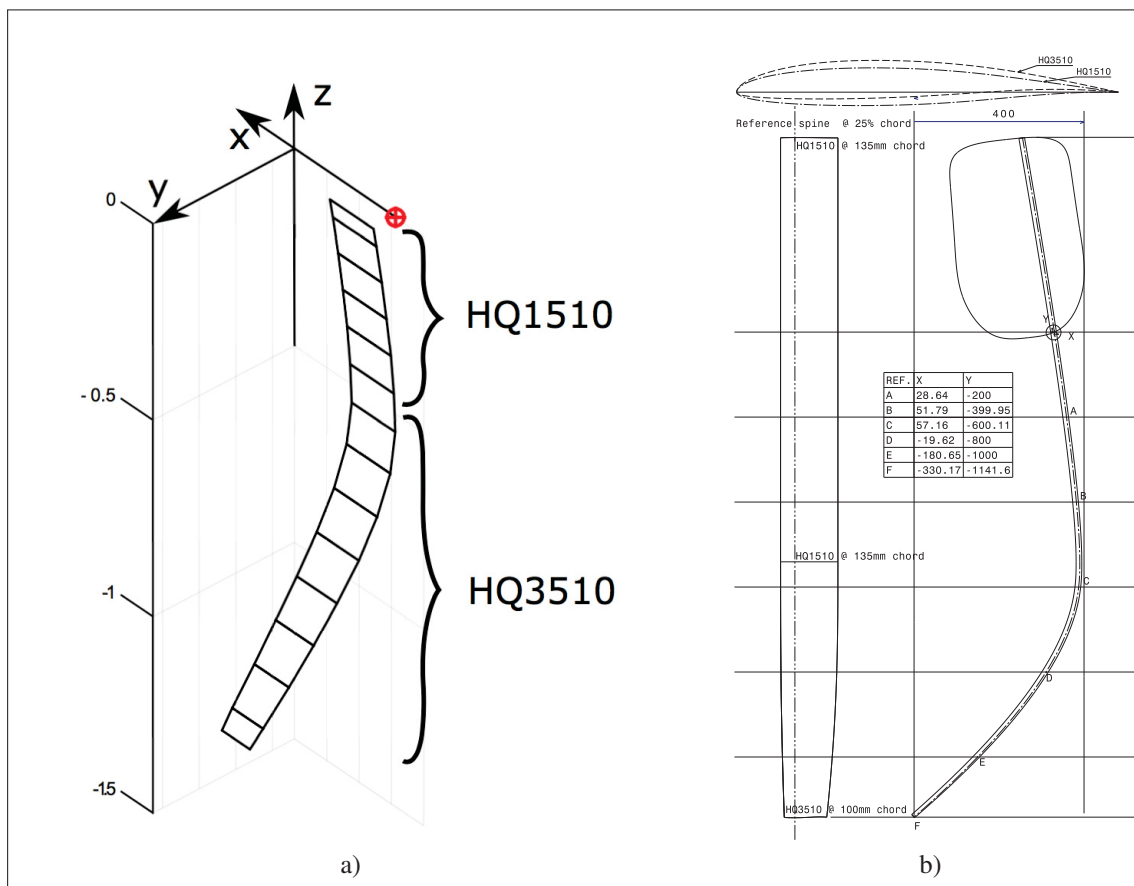
Figure 2.4   EH1 Hydrofoil Drawing
Designed by C. Dransfeld

With the results of the *Bending Moments* and *Shear-Loads* acting on the hydrofoil for the defined boat speeds and hydrofoil conditions along the wing-span (Figure 2.5), it was necessary to define the section where the *Non-Linear Passive Compliance* was going to happen and under what conditions of the boat and hydrofoil.
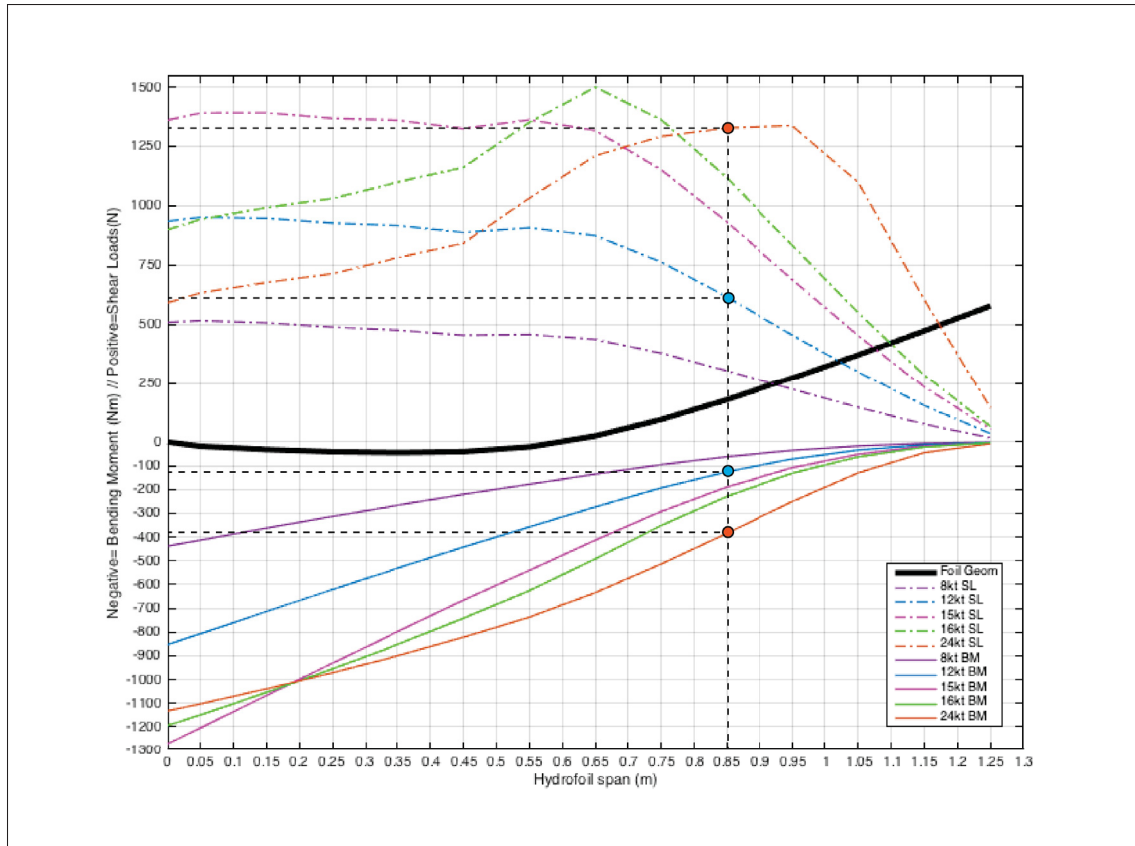
Figure 2.5   Bending Moment and Shear Loads on the EH1 with respect to boat speeds
Shear Loads data from (Schadt, 2016)

To exploit the *EH1* hydrofoil geometry, the section at $0.85m$ from the hydrofoils root was chosen to study the compliance. The choice for the section is based on a continuation of the hydrofoils natural curvature of the elbow and the practicality of the application. At that section, when a boat achieves the objective morphing speed of $12kt$, considered as the beginning of the transition phase between *Archimedean* and *Foiling* modes, an approximate bending moment of $115Nm$ is obtained. Then, at a speed of $24kt$, considered as the foiling mode and maximum speed for the case study, the bending moment obtained is approximately $375Nm$. A simplified diagram of the two geometrical states can be observed on Figure 2.6.
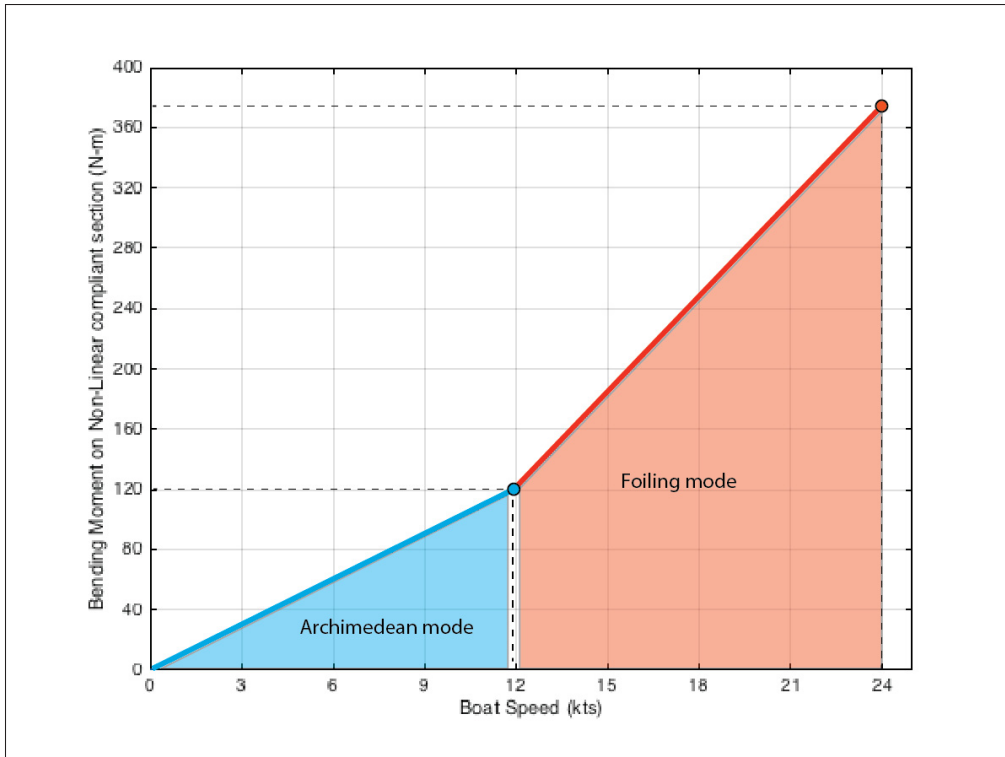
Figure 2.6   EH1 Hydrofoil Boat-speed vs. Bending Moment at $0.85m$

2.2   Hydrofoil Structure Design

Most successful hydrofoils are made out of one or many internal structural beams with an airfoil-shaped shell on the outside, similar to the ones found on wind turbine blades (See Figure 2.7). This configuration allows a lightweight structure design, where the main stresses are absorbed by the internal beam, and the airfoil shaped shell is responsible for the aerodynamic efficiency of the structure.
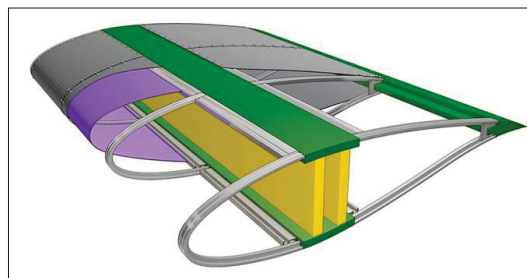
Figure 2.7   GE Wind Turbine Blade CAD
Image from *CleanTechnica.com*

Based on this approach, the *EH1* hydrofoil conceptual design consists of an internal box-beam acting as the main structural element embedded inside a airfoil-shaped shell. For the purpose of the preliminary design analysis, the design of the internal box-beam was chosen to have the maximum external dimensions of 15*mm* thick, by 60*mm* wide, using 4*mm* corner radius, as seen on Figure 2.8. These geometrical boundaries would make it impossible to use this beam structure on the *HQ3510* foil geometry with a 135*mm* chord-length and 10% thickness.
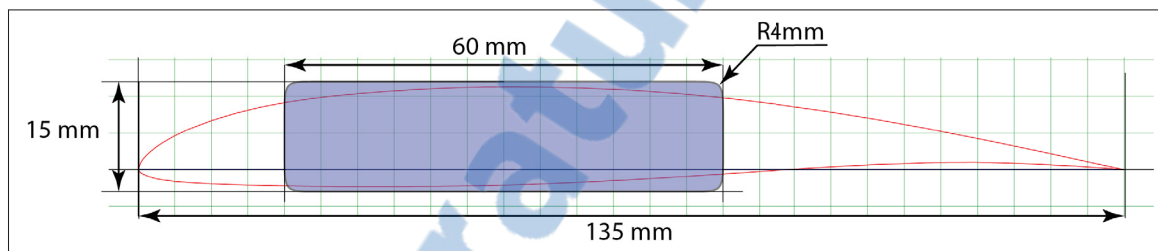
Figure 2.8   HQ3510 foil with structural box-beam
Adapted from *airfoiltools.com*(*www.hq-modellflug.de/*)

At an early stage in the project, the choice of these dimensions was based on a compromise for the proof of concept, where allowing a wider and thicker beam would reduce the complexity for manufacturing while reducing the amount of variables on the structural analysis.

2.3   Prototype Design and Materials

In order to achieve the *Prototype Conceptual Design (PCP)* of the *Passive-selective compliant hydrofoil*, as well as the *Proposed Design (PD)*, multiple analytic *MatLab* based tools as well as an *Abaqus FEM* model were developed to iterate over different design possibilities. This section presents the design approach and process, as well as the materials used to achieve the structural calculations and tests.

2.3.1 Design Methodology

The methodology used for the design of the two concepts can be seen in the flowchart on Figure 2.9. Beginning with the *PCP* design, manufacturing and testing process on Chapter 3 and followed by the *PD* on Chapter 4. The analytic tools used for the design calculations are presented on Section 2.4, while the FEM validation is presented in Chapter 3, along with the *PCP* design calculations.
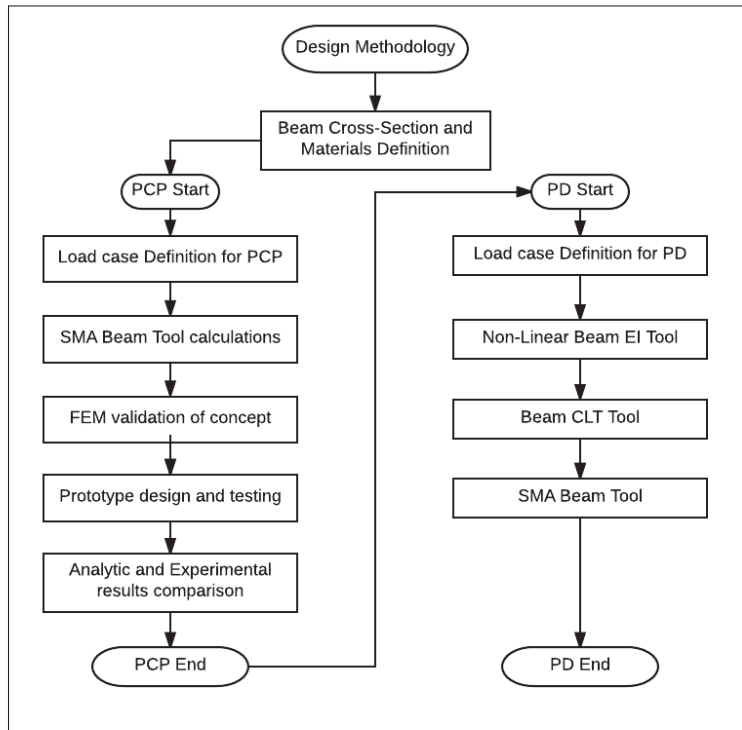
Figure 2.9   Design methodology flowchart

On both cases, the same hydrofoil section is selected to be compliant (see Figure 2.10), submitted to a pure-bending moment loading and neglecting the shear loads acting on the hydrofoil. This approach will also be convenient for the prototypes testing phase, where the goal is to apply a pure-moment by submitting the compliant section to a *Four Point Bending (FPB)*. A simplified diagram can be seen on Figure 2.10, representing the hydrofoils section at which the study will take place, and the proposed testing methodology.
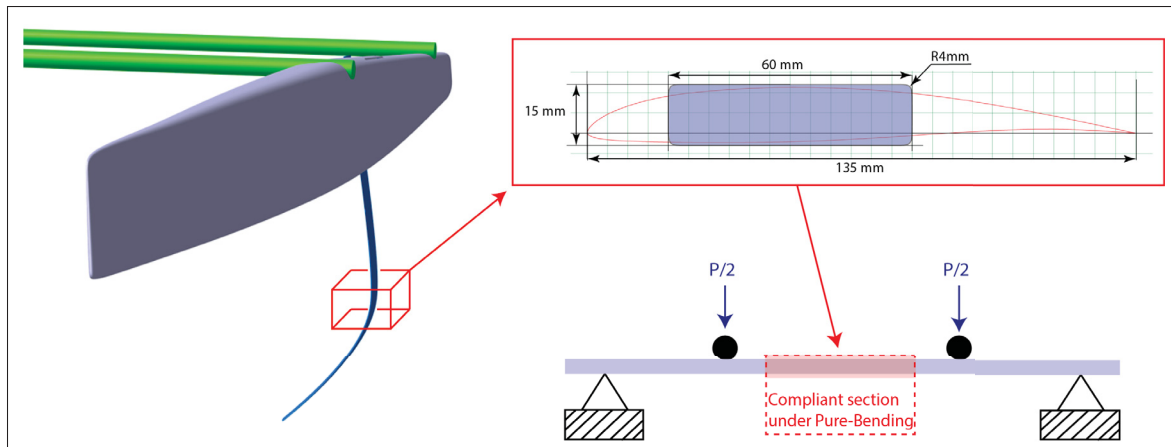
Figure 2.10   Study section on compliant hydrofoil

2.3.2   Conceptual Design

Because of the interesting mechanical properties of SMA when it comes to non-linear behavior, this material was considered for the design. The dependence on multiple user-parameters, such as the temperature to which the material is exposed, the speed of the deformation and whether the alloy is going through a loading or an unloading phase, the mechanical response of the SMA could be drastically modified, as shown on the *Literature Review* on Chapter 1. If all those variables are properly accounted for and controlled, the application could become extremely interesting.

With the intention of achieving large non-linear deformations on the hydrofoil lower section when exposed to a pure bending moment, many concepts using *Shape Memory Alloys* or more commonly used materials were sketched during the brainstorming phase. The considerations taken were emphasized by the practicality of the concept for the final application. One of the concepts consisted of a SMA-made elbow, joining the upper straight part of the hydrofoil and the tip. This would be possible by the machining of an *SMA* block to the desired geometry, but this process is not only expensive, but also extremely difficult to achieve the desired mechanical properties.

The chosen concept, seen on Figure 2.12, was composed by three main materials; *CFRP, Structural Foam and SMA*. The cross section of this beam is seen on Figure 2.11, where the

SMA section would be always submitted to tension when the pure-bending moment is applied. The CFRP would be submitted to compression, and the foam core would act as a spacer keeping the SMA section at the same height during the whole deformation phase.
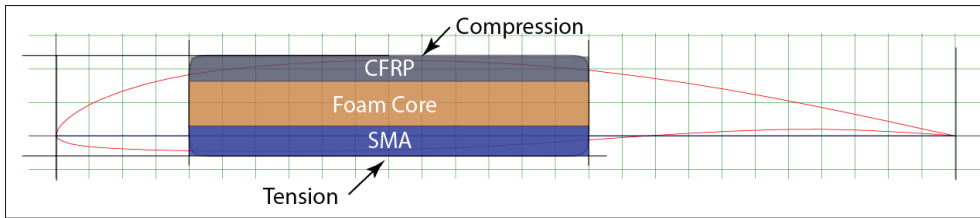
Figure 2.11   Concept design cross-section with foil profile
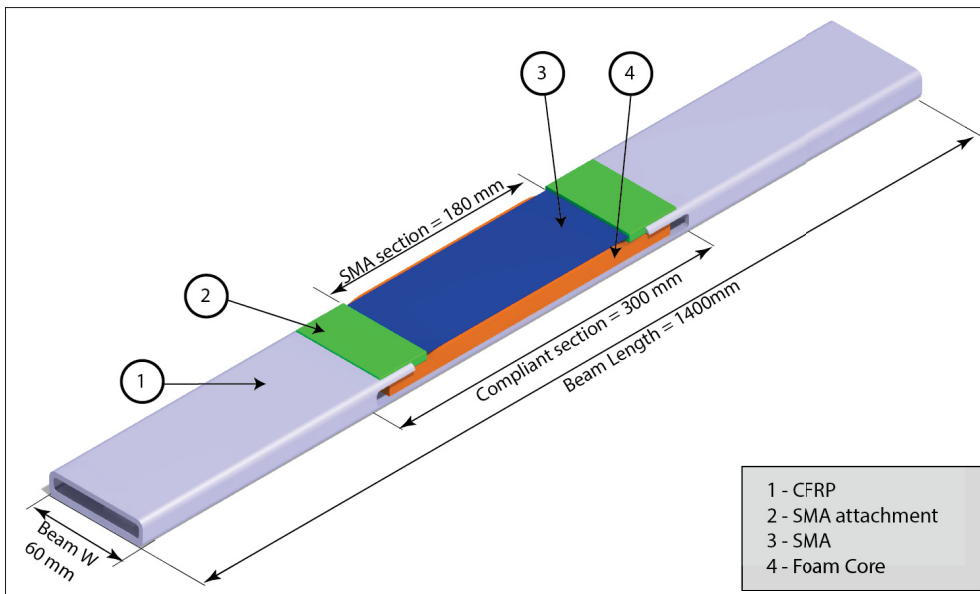
Figure 2.12   Compliant section prototype CAD

2.3.3   Materials & Characterization

To achieve accurate calculations as close as possible with the real application, the materials used for the design needed to be characterized with the projects envelope methodology, where the *SMA* and the *CFRP* were tested following practical and conventional methods.

2.3.3.1 SMA

The SMA used for this project was the Super-Elastic *UDIMET*® N*iTiNOL SMA wire* ⊘ 0.5*mm* from *Special Metals*. This wire has an Austenite Final temperature (A_f) of 4 °C, as specified in the *Certificate of Test* presented on Appendix I, meaning that above this temperature, the material behaves as super-elastic. For the application, the room temperature was defined at 20 °C, making this alloy a good choice for the hydrofoil, supposed to be submerged in water. The wire was tested on a *Zwick Z50kN* tensile testing machine at the operation temperature, with an uncertainty of ± 2 °C, measured during the testing phases. The cycle of loading was defined by the *Standard Test* ASTM F2516. A summary of the test procedure is presented on Figure 2.13.
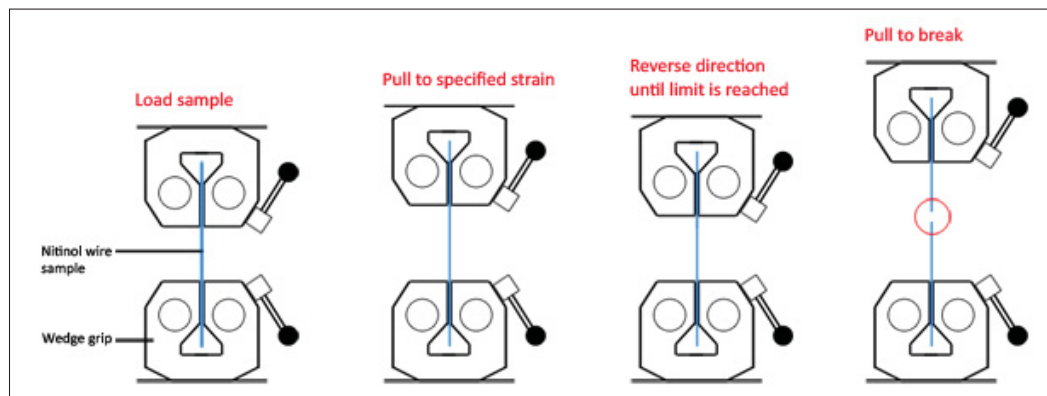
Figure 2.13 NiTiNOL Tension Testing as per ASTM F2516
Image adapted from Admet.com

Before the choice of the *UDIMET wire* was made, many other *NiTiNOL* wires with different compositions and diameters were tested. While being submitted to high strains, either when tested or during the actual application, the thin wire needs to be fully fixed, as any other member for any functional structure. To achieve this, the *wire clamping* technique seen on Figure 2.14a is usually unsuccessful because the induced stresses at the attachment point weakens the wire locally, creating failure before the maximum strength is achieved. The use of *Capstan Grips* (see Fig. 2.14b) solves the previously described issue by using the friction along the circular grips to have a uniform loading and reduced stress concentration on the thin diameter wires.
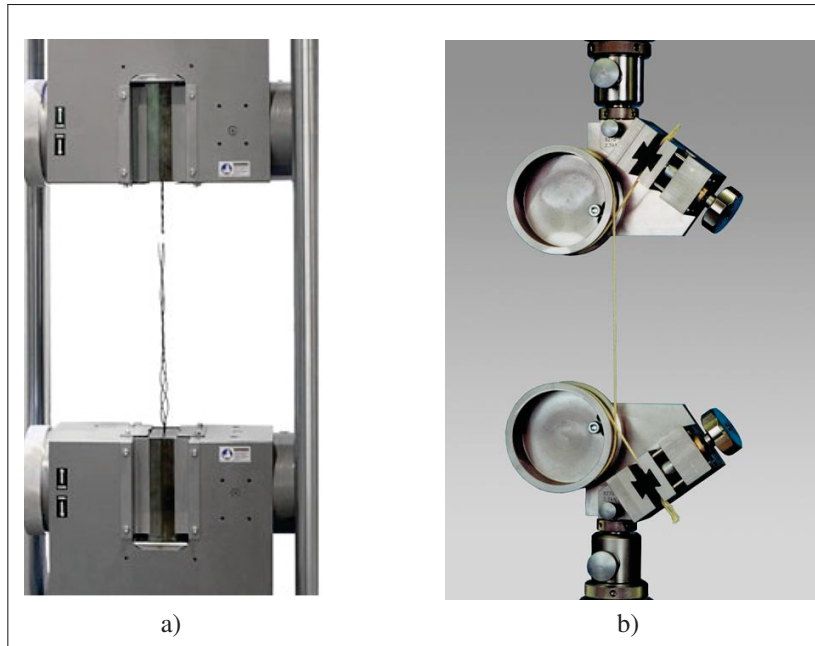
Figure 2.14   Tensile testing grip examples for *NiTiNOL* wires
(a) Flat Grip clamping, (b) Capstan wire grips

With the objective of finding a solution to secure the wire for the material characterization and *training*, as well as for the *PCP* application, a solution inspired from the previously described test methods was developed using the *Pin Loaded Strap* method (see Figure 2.15).
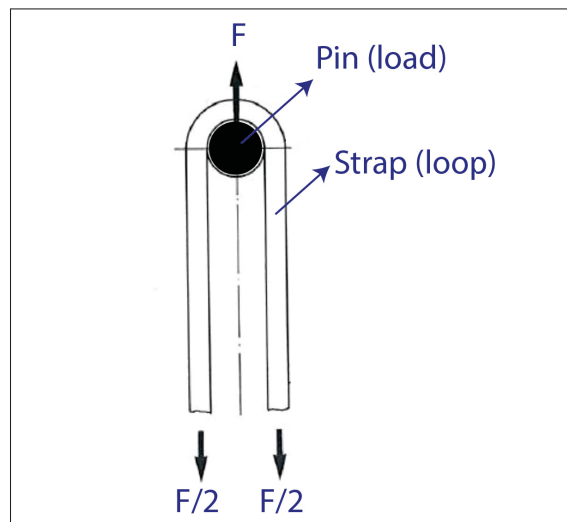
Figure 2.15   Pin-loaded strap loads diag.

This simple, efficient and strong solution is used in high strength tensile applications, like sailboat shrouds attachments, as seen on Figure 2.16, where the high stresses can be efficiently distributed over the hull structure.
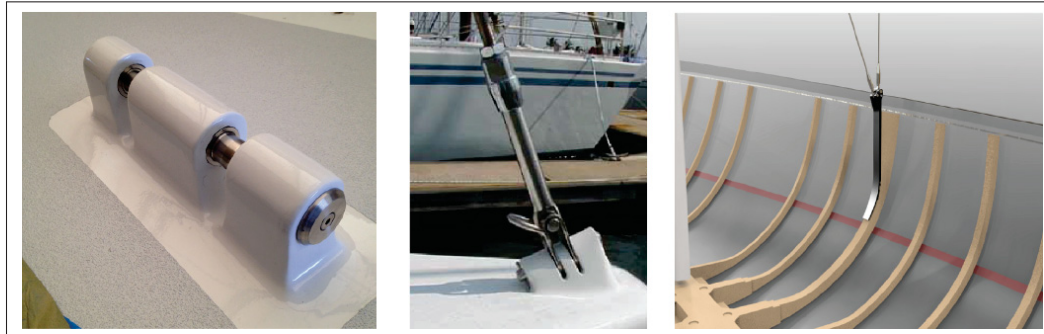
Figure 2.16   Pin-loaded examples on yachts shrouds and stays
Adapted from *www.f-boat.com*

With this system, the wires could be characterized and installed for testing as well as for the *PCP*. The calculations for the high loading of the prototype were done following the equations from *Fiber-Plastic Composite Structures* (Schürmann, 2007). The equations and detailed descriptions, adapted from the literature can be seen on Figure 2.17.
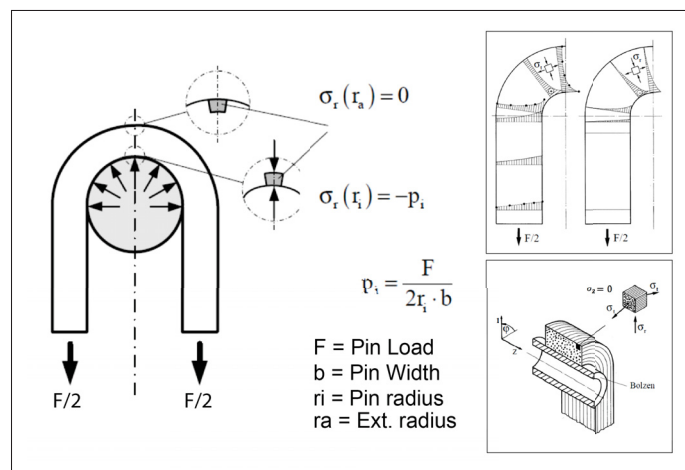
Figure 2.17   Pin-loaded strap stresses diagram
Adapted from Schürmann (2007)

By using this technique, the SMA wire characterisation was completed and the final Stress-Strain results, as well as the complete material properties were determined. These are shown on Figure 2.18 and Table 2.1 respectively.
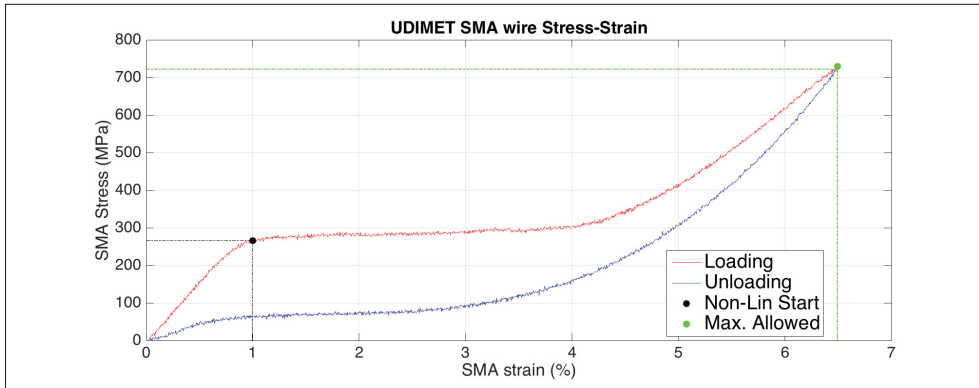
Figure 2.18   Stabilized UDIMET SMA Wire

Table 2.1   SMA testing parameters and obtained properties

SMA Wire Specifications		
Specimen Length	100	*mm.*
Diameter ⌀	0.5	*mm.*
Austenite Final Temp((A_f))	4	°C
Nickel	55.91	*wt.%*
Titanium	44.06	*wt.%*
Oxygen	0.05 (max.)	*wt.%*
Carbon	0.05 (max.)	*wt.%*
Testing Parameters		
Nominal Temperature	20±2	°C
Loading Speed	1	*mm/min*
Unloading Speed	0.5	*mm/min*
Maximum Strain (ε)	10	%
Training Cycles	100	Cycles
Obtained Material Properties		
Linear E Modulus	≈ 30	*GPa*
Maximum Design Strength (σ)	722	*MPa*
Maximum Design Strain (ε)	6.5	%
Ultimate Tensile Strength (σ)	≈ 1100	*MPa*
Ultimate Tensile Strain (ε)	≈ 8.2	%
Stabilization at	≈ 65	Cycles
Initial Residual Strain (ε)	≈ 0.4	%

2.3.3.2 CFRP

For this project, the composite material chosen was the *MTM49-3/34-700WD(12K)-200-35%RW*. This custom made unidirectional material is a *Carbon Fiber Reinforced Polymer (CFRP)*, where the matrix is an epoxy pre-impregnated resin *MTM49-3* produced by *Cytec* and for the reinforcement a *Grafil 34-700WD*, a high strength carbon fiber from Mitsubishi. The material properties of this composite was obtained from IKT, as seen on Table 2.2.

Table 2.2 MTM49/34-700WD Estimated Material Properties

Pre-preg Composite Physical Properties		
Theoretical Ply Thickness	0.2	*mm*
Experimental Ply Thickness	0.182	*mm*
Aerial Weight	200	g/m^2
Resin Weight Fraction	35	*%*
Mechanical Properties		
0° Tensile Modulus E_{11}	124.5	*GPa*
90° Tensile Modulus E_{22}	9.1	*GPa*
In-Plane Shear Modulus G_{12}, G_{13}	3.94	*GPa*
Off-Plane Shear Modulus G_{23}	3.37037	*GPa*
Poissons' Ratio v_{12}	0.3	
0° Tensile Strength X_t	2575	*MPa*
0° Compression Strength X_c	1235	*MPa*
90° Tensile Strength Y_t	40	*MPa*
90° Compression Strength Y_c	182	*MPa*
Inter Laminar Shear Strength (ILSS)	85.7	*MPa*

To complement the previously estimated material properties for the *MTM49-3/34-700WD*, a simple experimental evaluation of a composite specimen was done to validate the *Ply Thickness* and the Tensile Modulus (E_{11}). To proceed, a 400*mm* x 60*mm* flat section was manufactured, composed of 24 plies on a $[\pm15/0_2/\pm15/0_2/\pm15/0_2]_s$ layup. Once cured, the thickness was measured at $\approx 4.368mm$, making the *Ply Thickness* equal to $\approx 0.182mm$.

To validate the laminate stiffness and evaluate the theoretical elastic modulus E_{11}, the specimen was submitted to a three point bending (TPB) test to obtain the *Force(F)-Displacement (W_z)* behavior, as seen on Figure **??**. The experimental data was then compared with the *Elastic*

Beam Theory equations 2.2 and 2.1, where L is the length of the evaluated specimen of $150mm$, being this the distance between the supports for the *TPB*, I_x the second moment of inertia of the plate section, and E_{fx} the flexural elastic modulus of the specimen on the x orientation.

$$I_x = \frac{b\,t^3}{12} \Rightarrow I_x = \frac{60mm\,(4.368mm)^3}{12} \approx 416.7mm^4 \tag{2.1}$$

$$w_z = \frac{F\,L^3}{48\,E_{fx}\,I_x} \Rightarrow E_{fx} = \frac{F\,L^3}{48\,I_x\,w_z} \approx 108GPa \tag{2.2}$$

Finally, to evaluate the results, the laminate with the theoretical material properties was assembled on an *ABD matrix*, following the basic *CLT* calculations to extract the E_{fx} value and compare with the estimated calculations. The results can be seen on equation 2.3.

$$E_{fx} = \frac{12}{t^3\,D'_{11}} = \frac{12}{(4.368mm)^3\,1354\,x\frac{10^{-6}}{GPa-mm^3}} = 109.928 \approx 110GPa \tag{2.3}$$

As seen on Figure 2.19, the results are equivalent, giving an approximate bending stiffness of $110GPa$ for a laminate composed of unidirectional fiber having a longitudinal stiffness of $124.5GPa$.
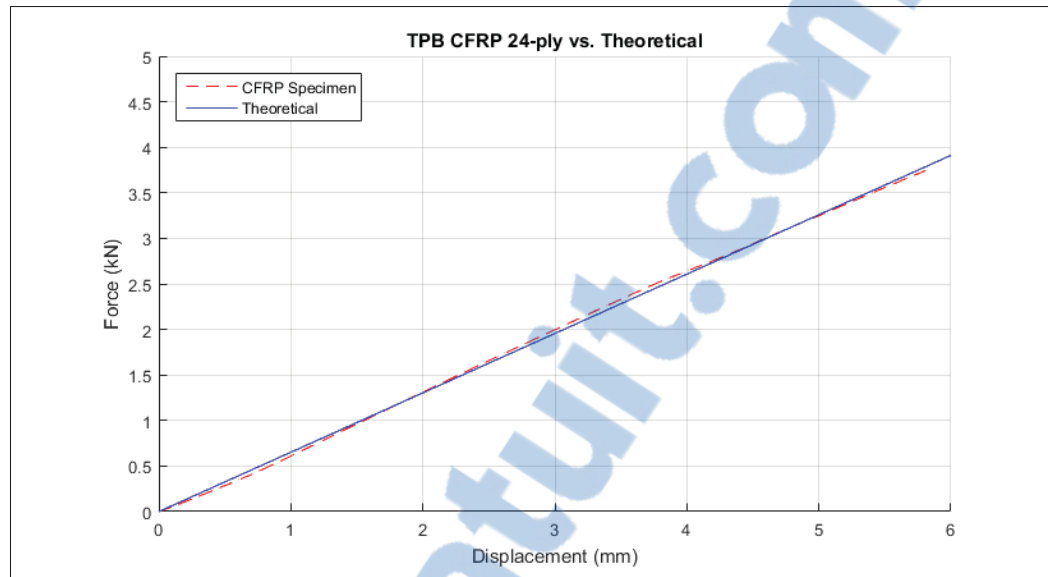
Figure 2.19   Three Point Bending plate test vs. Calculation

2.4   Analytical Design Tools

2.4.1   Non-Linear Beam *EI* Tool

This preliminary design tool was developed to obtain the geometrical and structural design envelope of a *Non-Linear Compliant Hydrofoil* submitted to a load case, represented by a sailing state. Based on a *Simulink™ Sim Mechanics™* model and a series of *MatLab™* scripts, the tool has the capability to determine the spanwise stiffness distribution required *EI (Nm^2)* of the hydrofoil structure to achieve a deformed final loaded geometry while respecting material deformation allowances. The ultimate goal of this model is to evaluate the internal efforts on highly compliant structures under different structural states.

2.4.1.1   Methodology

The calculations to achieve the final results are based on the *Strength of Materials* equations (F & Jr., 2011) and the *Lumped-Parameter method*. This last method proposed by Chudnovsky

42

et al. (2006) allows to discretize a continuous beam into multiple rigid generalized sub-elements, coupled with springs and dampers, as seen on Figure 2.20.
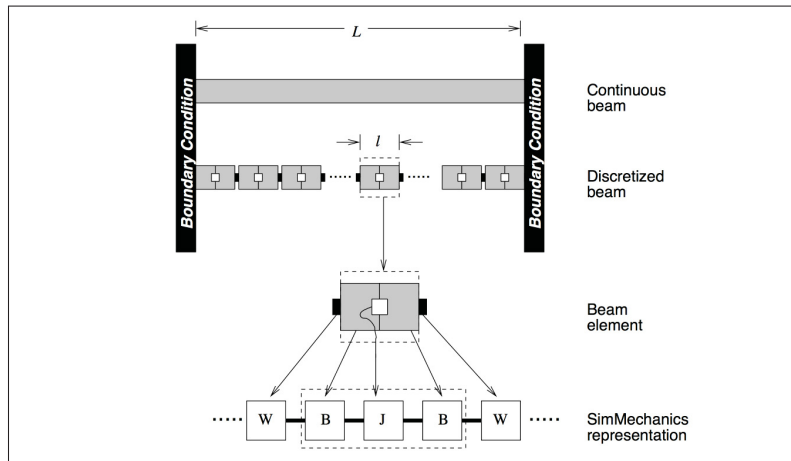
Figure 2.20   Lumped-Parameter beam representation
Adapted image from *Flexible Bodies*-Mathworks.com

The beam of length L from the previous image can be subdivided in n elements, each one of these elements called *Generalized Beam Elements (GBE)*, giving an element length of l. Every *GBE* can be defined as a $B - J - B$ *(Body-Joint-Body)* member, fixed to the subsequent element by a welded joint W. On Figure 2.21 a representation of a *GBE* of length l is shown, submitted to a generalized load F, and deformed position x.
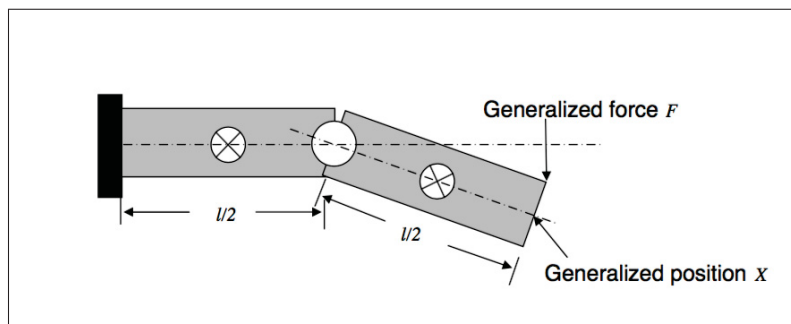
Figure 2.21   Lumped-Parameter element (GBE)

Each one of these elements can have up to 6 *DOF* at the joint *J*, being three rotations and three translations. In the case of the hydrofoil application, the structure is submitted to a 2*D* load case in the $[Y - Z]$ plane, where only the bending stiffness's are considered, reducing the model to 3 *DOF*, from which: *Y*, *Z* are the translations and θ is the rotation at the joint *J*, as presented on Figure 2.22.
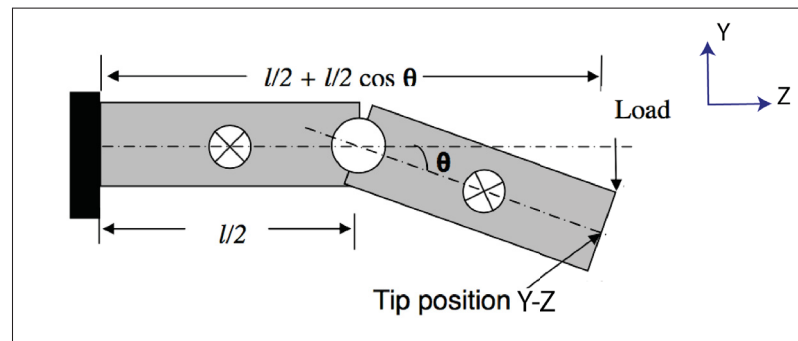
Figure 2.22   Deformed GBE with Parameters

The main element on the *Lumped-Parameter* method is the *joint J*, being represented by the elastic coefficients of a *Spring* (k) & *Damper* (c). While the complete description of the *Jacobian* approximation to apply the lumped-parameter method can be seen on Chudnovsky *et al.* (2006), the equation to obtain the *spring* coefficient is expressed on equation 2.4, where k_x is the rotational stiffness around the *x* axis of the joint, expressed in *Nm* , $\widehat{EI}_{xx}$ is the beam stiffness in Nm^2, and "*l*" the length of the *GBE* in *meters*.

$$k_x = \frac{\widehat{EI}_{xx}}{l} \tag{2.4}$$

For the damping parameter (c), defined as $2\zeta\omega_0$, a quasi-empirical calculation is proposed by the methodology, accounting for the energy-loss effects and equilibrium of moments at the nth *GBE*. Because the built model can be considered quasi-static, *Damping* coefficient is simply determined empirically to allow for a fast convergence.

2.4.1.2 Beam Model Definition

Sim Mechanics is a toolbox of Simulink, a block diagram environment for Model-Based Design in MatLab. SimMechanics allows to simulate complex multi-body systems with an embedded *GUI*, making the graphical representations of the systems easier for the user.

The *Non-Linear Beam EI Tool* is based on a *SimMechanics* model, where the internal structure of the hydrofoil is represented by a rectangular *cantilever box beam*, composed by n elements *(GBE)*, following the *Lumped-Parameter* method. The representation of a $3D$ hydrofoil structure geometry and the catamaran hull is presented on Figure 2.23, where the *EH1* hydrofoil geometry (Figure 2.4) is defined and the approximate overall dimensions of the catamaran hull are presented as a reference.
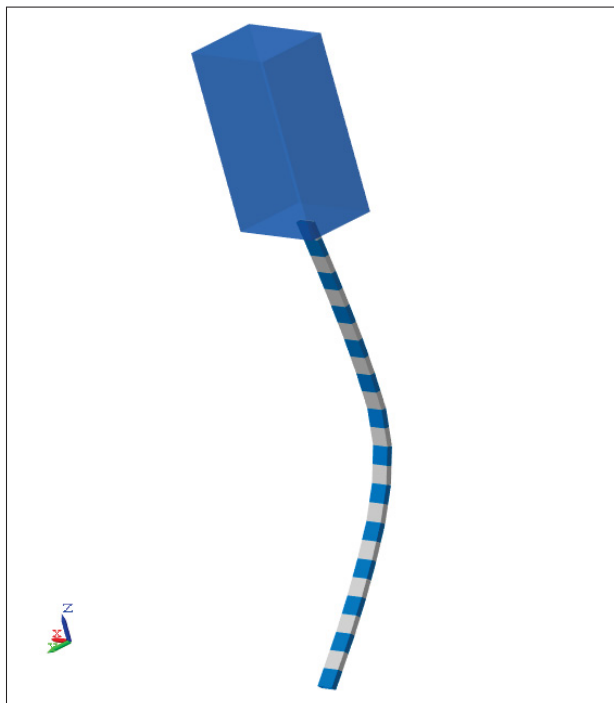
Figure 2.23   SimMechanics representation
of Hull and Hydrofoil structural beam

To create this model, the block diagram representing the Hull-Beam system can be seen on Figure 2.24, where the *Boat Hull Body* represents the *Hull* of the catamaran, and the *LP Beam*

represents the Hydrofoils Internal structure as a Lumped-Parameter Beam.

Other than the basic geometrical parameters and load definition, the model was defined to be adaptive, meaning that if the study needs to have a greater amount of elements to define a beam structure, the *GBE* elements length dimensions adjust to create a more refined geometry and results.
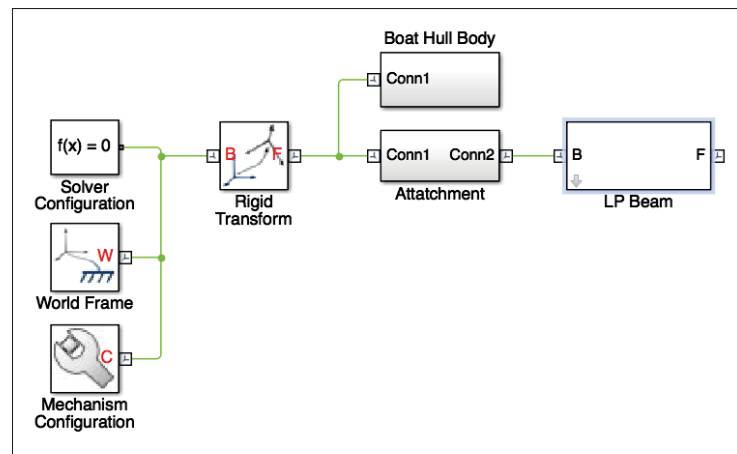
Figure 2.24   SimMechanics Model main diagram

Inside the *LP Beam block*, the multiple *GBE* elements conforming the beam *(Beam Segment n^{th})*, as well as the *Data Aquisition (DMA)* blocks for each element as seen on Figure 2.25, returning the **D**isplacement of the element, reaction **M**oment on the joint, as well as the **A**ngle of the joint.
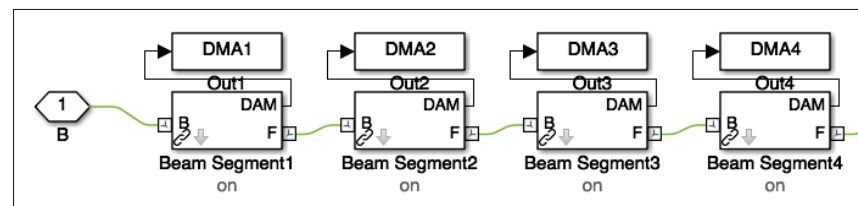
Figure 2.25   LP Beam block diagram with DMA Data Aquisition

Each one of the *GBE* internal structure consists of 5 main *sub-divisions*. These sub-block elements are represented in Figure 2.26 with colors, from which, undeformedthe two *green* are

46

the rigid bodies, the *yellow* represents the joint, the *red* is where the loads are introduced into the system and finally, the *blue* is the *DMA* data acquisition. All these input/output are represented by connection lines on the higher level block diagrams.
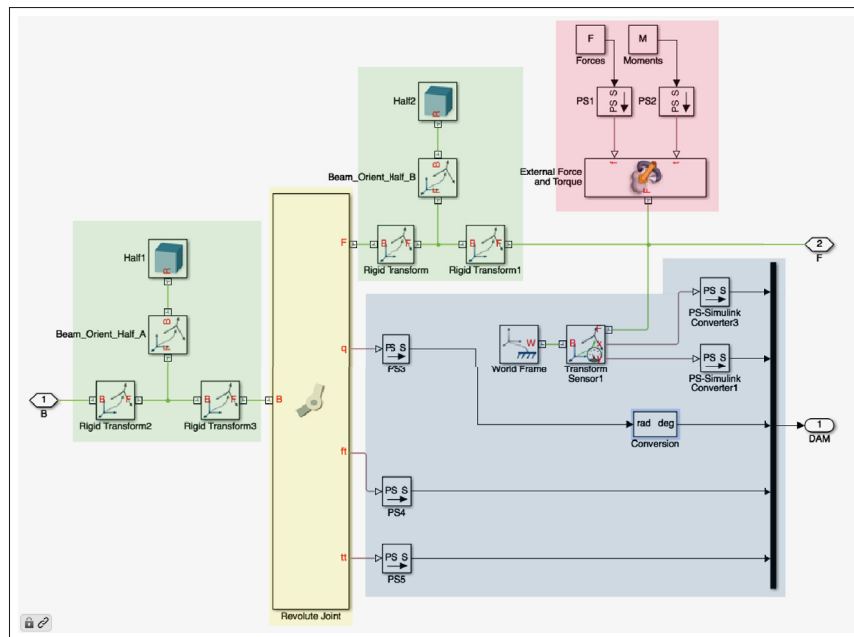
Figure 2.26   Beam GBE block diagram

One example of the potential use of this model is presented on Figure 2.27, where a 13 elements beam, with the *EH1* hydrofoil geometry is submitted to a hydrodynamic load. The particularity of this load introduction is that it remains always perpendicular to the hydrofoils' surface, therefore taking into account geometric non-linearity.

On Figure 2.27a the initial geometry of the hydrofoil is presented, then as the speed increases the load on the hydrofoil increases and the compliance is achieved (2.27b), with a greater resultant net force F_z, subsequently increasing lift and reducing drag by diminishing the water-hull contact area. The model representation of the superposed deformation sequence is shown on Figure 2.27c, with the undeformed state on the right side, an intermediate state on the middle and the final deformed beam on the left.
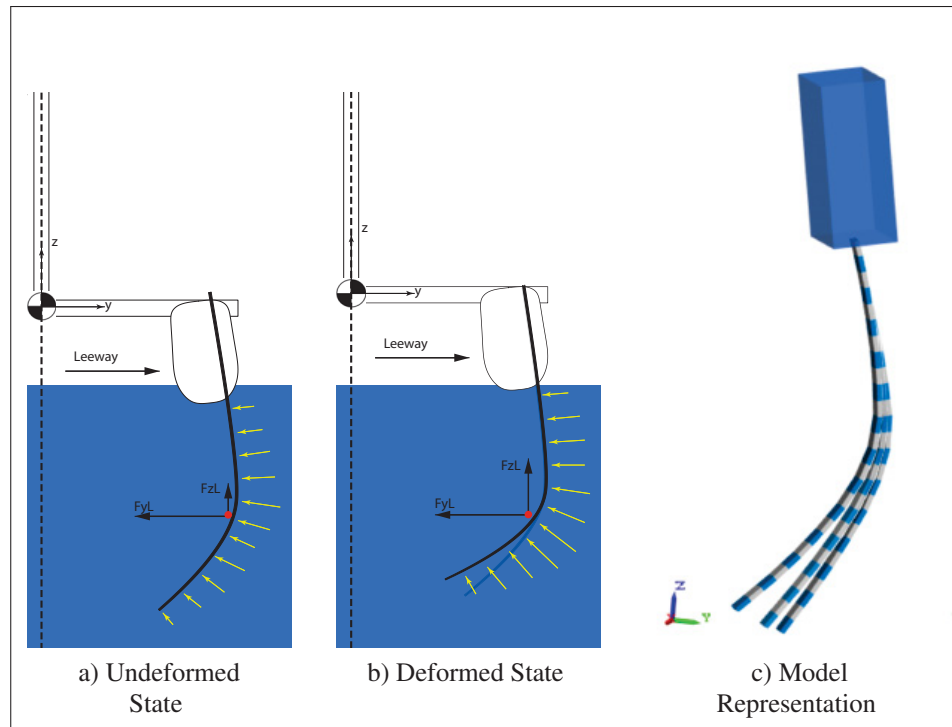
Figure 2.27   Model Capability representation

2.4.1.3   Model validation

In order to validate the methodology proposed by Chudnovsky *et al.* (2006) and confirm the *non-linear* capabilities of the tool, a beam model was defined to compare against the results of Dado & Al-Sadder (2005). With a unit-less generic beam model, where the rigidity (EI) and beam length L is defined as "1" (Figure 2.28), Dado compares large deformations of his proposed technique against the *MSC-NASTRAN* FEM software results.
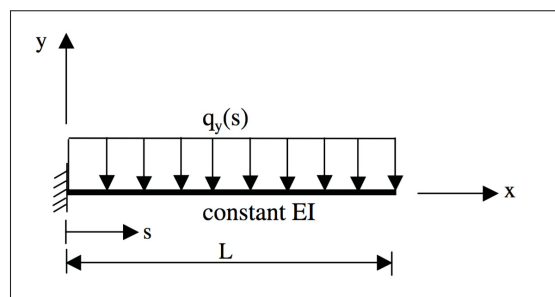
Figure 2.28   Dados' beam load case diag.

On the *Sim Mechanics* model, the *EI* stiffness was converted into a k_z term, as expressed on equation 2.4, becoming $EI = 1/l$. The results were then compared against a 15 element equivalent beam on the *Sim Mechanics* model, where the *green-black* overlapped results match with the results from Dados', as seen on Figure 2.29. On that image, the $\overline{q_y}$ represents the unit *load*, and the horizontal and vertical plotting axes the spatial position $(x - y)$.
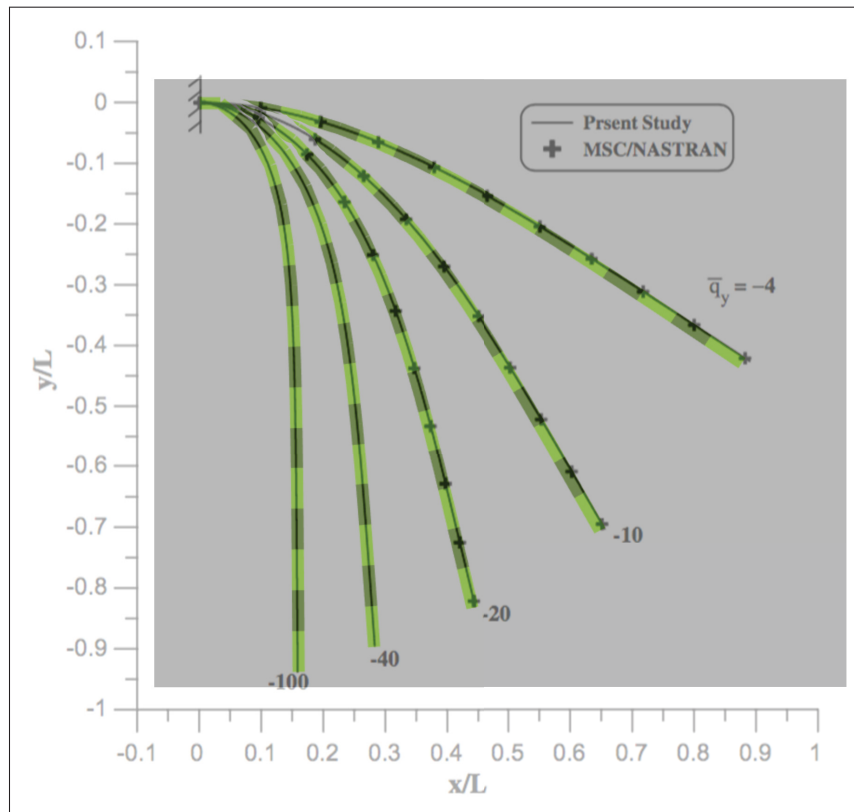
Figure 2.29   Sim Mechanics model validation
Adapted image from (Dado & Al-Sadder, 2005)

It is possible to see the similarity and consistency of the large deflection results between the data from the article (Dado & Al-Sadder, 2005) and the *SimMechanics* model on the superposed image. Unfortunately, only a graphical approximation of the results can be done, as the numerical data is not available on the work from Dado & Al-Sadder (2005).

2.4.1.4   Tool implementation and scripting

The main objective of the tool is to obtain the optimal *EI* distribution for a specific compliant geometry under a static load-case. The final geometry is defined by a local maximum strain allowance, bending moment and cross-section properties (ε, M_{Beam}, $\widehat{EI}_{Beam}$ *and* $\bar{y}$) at each GBE joint, as shown on equation 2.5.

$$\varepsilon = \frac{M_{Beam}\,\bar{y}}{\widehat{EI}_{Beam}} \tag{2.5}$$

To begin the calculations with the *Non-Linear Beam EI Tool*, the user needs to define the *geometrical boundaries*, the *load case* to which the structure will be submitted and the convergence criteria, defined by the maximum allowed strain (ε) at each element.

The geometry of the beam was defined by the overall length L, the number of *GBE* elements n, the cross section dimensions, height (h), width (w), the wall thicknesses and the angle (θ) to which the joints (J) are rotated to define the initial unloaded beam geometry. A *Sim Mechanics* GUI visualization of the beam cross-section element can be seen on Figure 2.30.
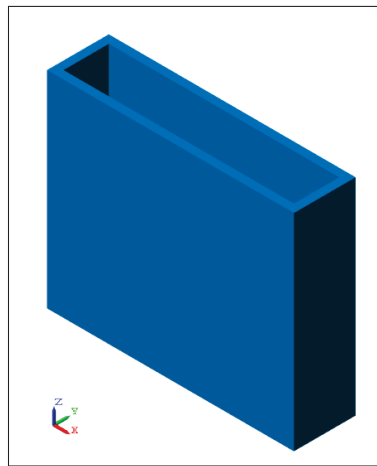
Figure 2.30   Sim Mechanics
beam section geometry

The hydrodynamic loads are usually defined in the three orthogonal axes, x, y, z. In this case, since the analysis is only done on a $2D$ plane, the x component representing the drag is neglected.

As a final step, the maximum strain (ε) is defined by the designer for every element, following a practical criteria. For the case of a hydrofoil that does not allow large non-linear deformations, the strain would be kept to values that assure a material integrity, below failure values. For the case of the *Non-Linear Hydrofoil* design, the section or sections where the large deformations are allowed would at least double the maximum strain allowances from the conventional structure. A feature of the tool to allow a faster convergence is a tolerance definition (or error allowance). This criteria can be defined as a percentage of the target strain values. For initial studies, these values should be kept at a higher tolerance on the first iterations of the preliminary design, and reduced when a refined solution is needed.

An example of the MatLab input structure matrix of a 13 elements beam is shown on Figure 2.31, where the initial K_x *GBE* joint coefficients in $N - m^2$ are on the first column, followed to the right by the applied loads vectors F_{xyz} in N, and the rotation angle θ in degrees to define the geometry *(GeoAngAbs)*. The last two columns *StrMax & StrTol* represent the maximum allowed strain percentage on the element and the error tolerance on the calculation, respectively.

Fields	Kx	Fxyz	GeoAngAbs	StrMax	StrTol
1	3.1991e+10	[0,0,0]	0.8200	0.1500	0.0750
2	3.1991e+10	[0,0,0]	1.8900	0.1500	0.0750
3	3.1991e+10	[0,0,0]	2.5200	0.1500	0.0750
4	3.1991e+10	[0,0,0]	4.7600	0.1500	0.0750
5	3.1991e+10	[0,0,0]	6.8200	0.1500	0.0750
6	3.1991e+10	[0,0,0]	17.0700	0.1500	0.0750
7	3.1991e+10	[0,0,0]	30.0600	0.1500	0.0750
8	3.1991e+10	[0,0,0]	38.9100	0.1500	0.0750
9	3.1991e+10	[0,0,0]	44.9700	0.1500	0.0750
10	3.1991e+10	[0,242.7423,0]	47.5700	0.1500	0.0750
11	3.1991e+10	[0,496.7380,0]	49.9100	0.1500	0.0750
12	3.1991e+10	[0,460.3362,0]	52.1100	0.1500	0.0750
13	3.1991e+10	[0,143.6232,0]	52.1100	0.1500	0.0750

Figure 2.31   Input Matrix Structure from Non-Linear Beam EI Tool.
$K_x(Nm^2)$, $F_{xyz}(N)$, $GeoAngAbs(deg)$, $StrMax(\%)$, $StrTol(\%)$

With all the input variables defined by the user, the calculation can begin. The analysis begins with an unrealistic beam stiffness, where the *EI* is considered 5 to 10 times higher than the realistic values. The load is applied as defined by the study and the deformation calculated with equation 2.5, evaluating the strain criteria for every n^{th} element, and adjusting the stiffness coefficient while iterating over these values one at the time, from the root to the tip, until the elements strain (ε) design criteria is met. The flow chart of the tool calculations is seen on Figure 2.32.
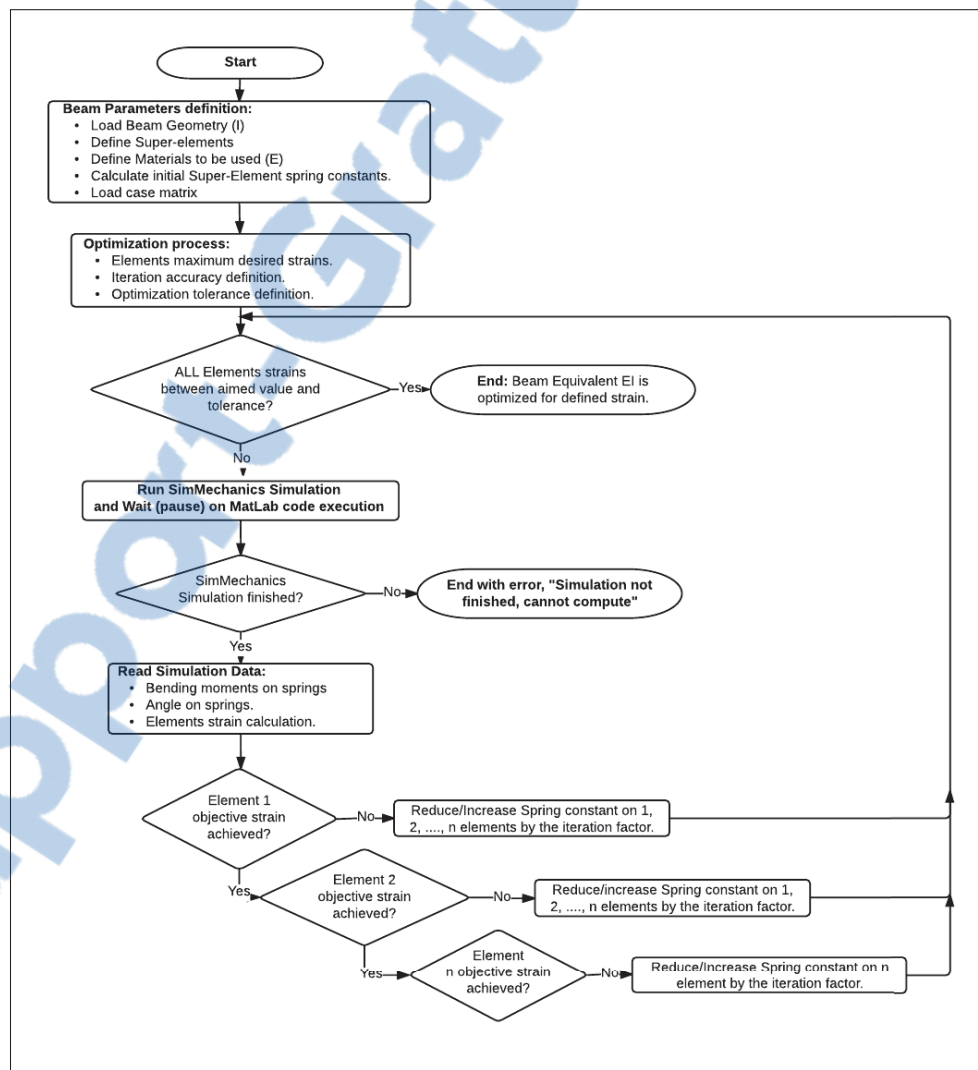
Figure 2.32   Flowchart for Non-Linear Beam EI Tool
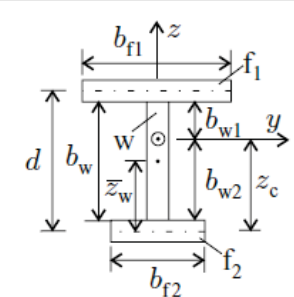
2.4.2 Beam CLT Tool

The *Beam CLT Tool* was developed to determine the preliminary internal beam structure of the hydrofoil made with laminate composite materials. Meant to work with the results and geometrical information defined by the *Non-Linear Beam EI Tool* (Section 2.4.1), the *Beam CLT Tool* is able to determine the *I-beam* laminate wall thickness of every n^{th} *GBE* element for a defined ply-stacking sequence.

2.4.2.1 CLT Concepts Review

The applied methodology of this set of scripts is based on the *Classic Laminate Theory (CLT)* from Gibson (2012), the composite beam equations from Kollar & Springer (2003) and the *I-Beam* calculations from Swanson (1997) to evaluate the needed design parameters.
Even though the *Conceptual Design* on Section 2.3.2 proposes a *Box-Beam* structure, composed of 4 walls, the preliminary calculations of the structure uses the I-Beam equations composed by two horizontal flanges $(f_1 \& f_2)$ and one vertical shear web (w). These two approaches are considered identical for the tool purpose, as the structure is mainly submitted to bending and the beam $\widehat{EI}_{xx}$ from Figure 2.33 would be equal if the *I-Beam* web thickness and ply stack is equivalent to the half *Box-Beam* side walls.

$$\widehat{EA} = \frac{b_{f1}}{(\overline{\alpha}_{11})_{f1}} + \frac{b_{f2}}{(\overline{\alpha}_{11})_{f2}} + \frac{b_w}{(a_{11})_w}$$

$$z_c = \frac{1}{\widehat{EA}} \left(\frac{b_{f1}}{(\overline{\alpha}_{11})_{f1}} d + \frac{b_w}{(a_{11})_w} \overline{z}_w \right)$$

$$\widehat{EI}_{yy} = \frac{b_{f1}}{(\overline{\alpha}_{11})_{f1}} (d - z_c)^2 + \frac{b_{f2}}{(\overline{\alpha}_{11})_{f2}} z_c^2 + \frac{b_{f1}}{(\overline{\delta}_{11})_{f1}} + \frac{b_{f2}}{(\overline{\delta}_{11})_{f2}} + \frac{1}{(a_{11})_w} \left(\frac{b_{w1}^3 + b_{w2}^3}{3} \right)$$

Figure 2.33   *I-Beam* Equations from Kollar & Springer (2003)

The parameters α, β & δ from the Kollar equations on Figure 2.33 are the compliance parameters from the *ABD* matrix, or ABD^{-1}, as seen in Equation 2.6, where the *A, B & D* terms represent the Tensile Stiffness, the In-Plane and Bending Coupling and the Bending Stiffness of the laminate respectively.

$$\begin{bmatrix} [\alpha] & [\beta] \\ [\beta] & [\delta] \end{bmatrix} = \begin{bmatrix} [A] & [B] \\ [B] & [D] \end{bmatrix}^{-1} \tag{2.6}$$

The assembly of the *ABD* matrix (Equation 2.10) is achieved by the equations 2.7, 2.8 and 2.9, where $\bar{Q}_{ij}$ represents the stiffness matrix of the lamina and z_k the ply position, as seen on Figure 2.34.

$$A_{ij} = \sum_{k=1}^{n} \left[\bar{Q}_{ij} \right]_k (z_k - z_{k-1}) \tag{2.7}$$

$$B_{ij} = \sum_{k=1}^{n} \left[\bar{Q}_{ij} \right]_k \frac{\left(z_k^2 - z_{k-1}^2 \right)}{2} \tag{2.8}$$

$$D_{ij} = \sum_{k=1}^{n} \left[\bar{Q}_{ij} \right]_k \frac{\left(z_k^3 - z_{k-1}^3 \right)}{3} \tag{2.9}$$
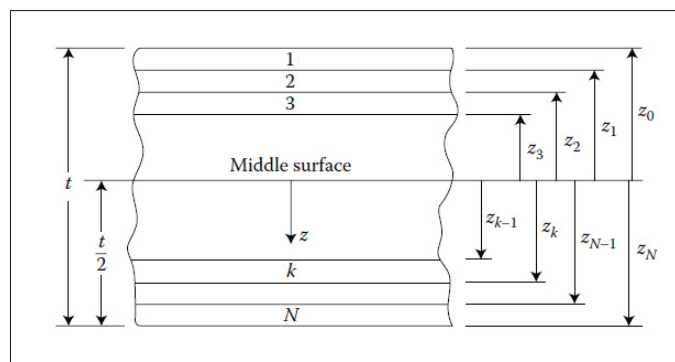
Figure 2.34   Lamina representation (Gibson, 2012)

As described in Gibson (2012), the *ABD* matrix relates the extensional stiffness matrix $[A]$ with the in-plane forces $[N]$ to the mid-plane strains $[\varepsilon^0]$, while matrix $[D]$ relates the moments $[M]$ with the curvatures $[\kappa]$.

The tool was designed to be used with symmetric ply-stacks, making the matrix $[B] = 0$, and assuming no coupling is present in the composite layup.

$$
\begin{bmatrix} N_x \\ N_y \\ N_{xy} \\ M_x \\ M_y \\ M_{xy} \end{bmatrix} = \underbrace{\begin{bmatrix} A_{11} & A_{12} & A_{16} & B_{11} & B_{12} & B_{16} \\ A_{12} & A_{22} & A_{26} & B_{12} & B_{22} & B_{26} \\ A_{16} & A_{26} & A_{66} & B_{16} & B_{26} & B_{66} \\ B_{11} & B_{12} & B_{16} & D_{11} & D_{12} & D_{16} \\ B_{12} & B_{22} & B_{16} & D_{12} & D_{22} & D_{26} \\ B_{16} & B_{26} & B_{66} & D_{16} & D_{26} & D_{66} \end{bmatrix}}_{[ABD]} \begin{bmatrix} \varepsilon_x^0 \\ \varepsilon_y^0 \\ \gamma_{xy}^0 \\ \kappa_x \\ \kappa_y \\ \kappa_{xy} \end{bmatrix} \tag{2.10}
$$

With the I-Beam stiffness $\widehat{EI_{xx}}$ from Kollar & Springer (2003) presented in Figure 2.33, a proposed technique from Swanson (1997) is used to evaluate the strains of an I-Beam while submitted to a pure bending moment M_x, depending on the flange width and length. The method from Swanson defines a difference on the flange *aspect ratio (AR)*, evaluated as the Beam Length (f_L) divided by the *beam flanges width* (f_W) $(AR = f_L/f_W)$. Equations are developed for a beam assembled by three components, where the two flanges $(f_1 \& f_2)$ are horizontal plates and the shear web (w) as a vertical plate (see Figure 2.35).

The beam curvature κ_x at the *Neutral Axis (NA)* is calculated as seen on equation 2.11.

$$
\kappa_x = \frac{\widehat{M}_{beam}}{\widehat{EI}_{xx}} \tag{2.11}
$$

The strains at the ξ position of the beam, on the *web* are calculated as seen on equation 2.12.

$$
\varepsilon_x^0 = \xi \kappa_x = \xi \frac{\widehat{M}_{beam}}{\widehat{EI}_{xx}} \tag{2.12}
$$
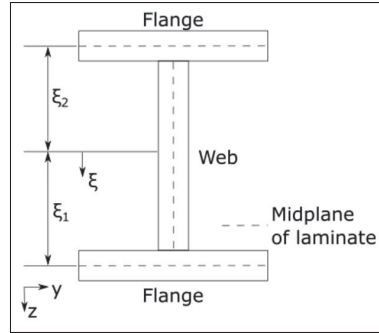
Figure 2.35 *I-Beam* diag.
(Swanson, 1997)

Depending on the *AR*, the strains ε_y on the flanges are evaluated differently. The equation 2.14 is used to calculate the strains for a narrow beam $(AR > 5)$, and 2.15 for the ones considered as wide$(AR < 5)$ assuming $\kappa_y^0 = \kappa_{xy}^0 = 0$. The strain ε_x is evaluated identically for both types of beams, as seen on equation 2.13 .

$$\varepsilon_x \ = \ (\xi + z_k)\kappa_x = \ (\xi + z_k)\frac{\widehat{M}_{beam}}{\widehat{EI_{xx}}} \tag{2.13}$$

$$\varepsilon_y = \varepsilon_y^0 + z_k \ \kappa_y = \left(\frac{\alpha_{12}}{\alpha_{11}}\xi \ + \ z_k\frac{\delta_{12}}{\delta_{11}}\right)\kappa_x = \left(\frac{\alpha_{12}}{\alpha_{11}}\xi \ + \ z\frac{\delta_{12}}{\delta_{11}}\right)\frac{\widehat{M}_{beam}}{\widehat{EI_{xx}}} \tag{2.14}$$

$$\varepsilon_y = \varepsilon_y^0 + z_k \ \kappa_y = \left(\frac{\alpha_{12}}{\alpha_{11}}\xi\right)\kappa_x = \left(\frac{\alpha_{12}}{\alpha_{11}}\xi\right)\frac{\widehat{M}_{beam}}{\widehat{EI_{xx}}} \tag{2.15}$$

The plane shear strains γ_{xy} are also evaluated differently depending on the *AR* of the beam, with equation 2.16 used for the narrow beams and equation 2.17 used for wide beams.

$$\gamma_{xy} = \varepsilon_y^0 + z_k \ \kappa_y = \left(\frac{\alpha_{16}}{\alpha_{11}}\xi \ + \ z_k\frac{\delta_{16}}{\delta_{11}}\right)\kappa_x = \left(\frac{\alpha_{16}}{\alpha_{11}}\xi \ + \ z\frac{\delta_{16}}{\delta_{11}}\right)\frac{\widehat{M}_{beam}}{\widehat{EI_{xx}}} \tag{2.16}$$

$$\gamma_{xy} = \varepsilon_y^0 + z_k \ \kappa_y = \left(\frac{\alpha_{16}}{\alpha_{11}}\xi\right)\kappa_x = \left(\frac{\alpha_{16}}{\alpha_{11}}\xi\right)\frac{\widehat{M}_{beam}}{\widehat{EI_{xx}}} \tag{2.17}$$

To calculate the stresses $\sigma_{x,y}$ and τ_{xy} for a ply, the strains $\varepsilon_x \, \varepsilon_y \, and \gamma_{xy}$ are multiplied by the stiffness matrix $\bar{Q}$ as shown in equation 2.18.

$$\sigma_{x,y} = [\bar{Q}] \{\varepsilon_{x,y}\} \tag{2.18}$$

To evaluate the potential failure of the beam structure, the *Tsai-Hill* failure criteria (see Equation 2.19), extracted from Gibson (2012) is used. If the result is greater than "1", structural failure is assumed.

$$\left(\frac{\sigma_1}{S_L}\right)^2 - \frac{\sigma_1 \sigma_2}{S_L^2} + \left(\frac{\sigma_2}{S_T}\right)^2 + \left(\frac{\tau_{12}}{S_{LT}}\right)^2 = 1 \tag{2.19}$$

2.4.2.2   Tool Methodology

To estimate the internal structure needed for a functional hydrofoil, this tool has the capability of defining the beam wall thickness, while the input parameters for this estimation come from the previous calculations on the *Non-Linear Beam EI Tool*. This means that for every calculated *EI* section *GBE*, a discrete *CFRP I-Beam* layup definition is determined to match the required local bending rigidity (EI).

To do so, the process iterates over a user defined layup ply-stack and orientations where the lamina material properties are defined by the user, such as E_1, E_2, G_{12}, v_{12} and the material tension and compression limits S_L^-, S_L^+, S_T^- and S_T^+.

The optimization is based on the lamina thickness, where it is defined at least as 5 times thinner than the real material for the initial iteration. The process starts with a comparison of the target $\widehat{EI}$ from the *Non-Linear Beam $\widehat{EI}$ Tool* and the composite equivalent $\widehat{EI}_{xx}$ from (Kollar & Springer, 2003) calculations. If the composite beam stiffness value is below the target value from the previous calculations, the lamina thickness is increased of 1% and the composite *I-Beam* is recalculated until the target value is achieved, providing the output of the *flanges* and *web* thickness (f_t, w_t) as seen on Figure 2.36.

When all the *GBE* sections are calculated, the tool evaluates the *Tsai-Hill* criteria on the tension and compression side of the beam with the associated bending moment calculated by the *Non-*

Linear Beam EI Tool, outputting the maximum failure index as reference.

In the case that the failure index is above 1, to which laminate failure is assumed, the local maximum strain would need to be reduced in the *Non-Linear Beam EI Tool* to stiffen the section, and the iteration restarts. The flowchart diagram of the tool can be seen on Figure 2.37
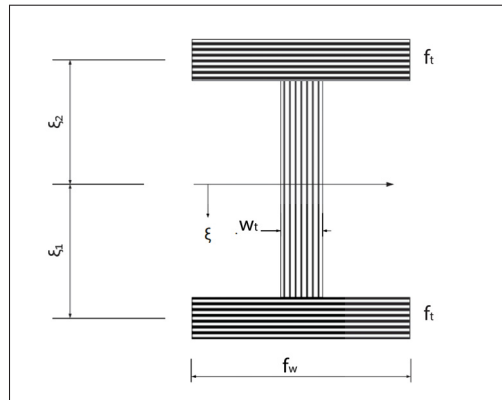
Figure 2.36   Composite I-Beam def.
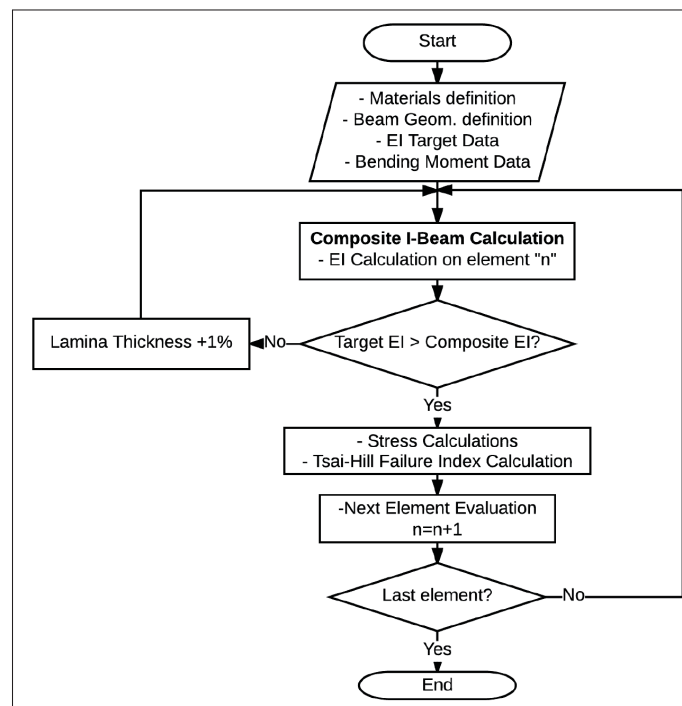
Figure 2.37   Beam CLT Tool Flowchart

2.4.3 SMA Beam Tool

The purpose of this set of scripts composing the *SMA Beam Tool* is to determine the approximate mechanical behaviour of a non-linear compliant beam section, composed by different materials, and submitted to pure-bending. The application was developed for the non-linear compliant hydrofoil concept, but generalized to any materials and geometries to achieve equivalent calculations.

2.4.3.1 Motivation

The need to test different *non-linear compliant beam concepts* with different materials and section properties was the main motivation to develop such tool. The goal was to have a pre-design tool for fast iteration calculations. With it, a great amount of time can be spared when comparing with FEA (*Finite Element Analysis*), since the parameters modifications and calculations are almost immediate when using the custom UI on MatLab.

2.4.3.2 Design boundaries and considerations

The boundary conditions for the analysis are defined by the geometrical constraints for the internal structure of the hydrofoil (Figure 2.11). Since the structure is assumed to be submitted to pure bending, the two target values are the beginning of the *non-linear compliance*, and the *maximum bending moment* considered at the maximum boat-speed, as well as the practical constraint of the possibility of using the hydrofoil throughout an acceptable life-cycle.
During the conceptual design process of the passive non-linear compliant beam, a concern about the application of the *SMA* wire came to the discussion for a design that considered the *CFRP* and *SMA* sections of same length, using a constant beam stiffness along the *x* axis, as seen on Figure 2.38.

For the case that a *Bending Moment* is applied (Figure 2.38), the large-strain capabilities of the alloy in tension ($\varepsilon \approx 7\%$) could put in jeopardy the integrity of the *CFRP* laminate when a large compliance is engaged, depending on the section properties. In this situation, the maximum
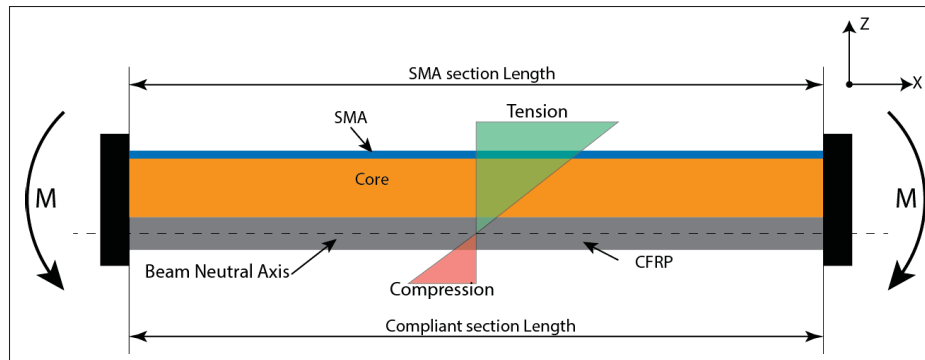
Figure 2.38   Constant stiffness beam section under pure moment

compression stress could be reached on the CFRP side, causing the structure to fail, when the SMA would be far from its maximum tensile strength.

One solution to this problem would be stiffening the CFRP section, and with so, reducing the non-linear effect of the SMA on the structure. This option is not very interesting, as the strain capabilities of the SMA would not be used to their full extent, and the *bending angle* (θ) of the beam would not be exploited to its maximum.

With the goal of exploiting the maximum capabilities of the materials in the design, a concept shown on Figure 2.39 was developed, where for a compliant section of length "L", the length of $SMA(L_{sma})$ would be shortened. With this approach, for the same geometrical strain in the top-side $\varepsilon = \frac{M\,y}{\widehat{EI}_{cfrp}}$ of the compliant beam under pure-bending, a higher local strain would result in the *SMA*. This effect can be described as *Strain acceleration*, and it is made possible because the elastic modulus of the alloy is much smaller than the *CFRP*.
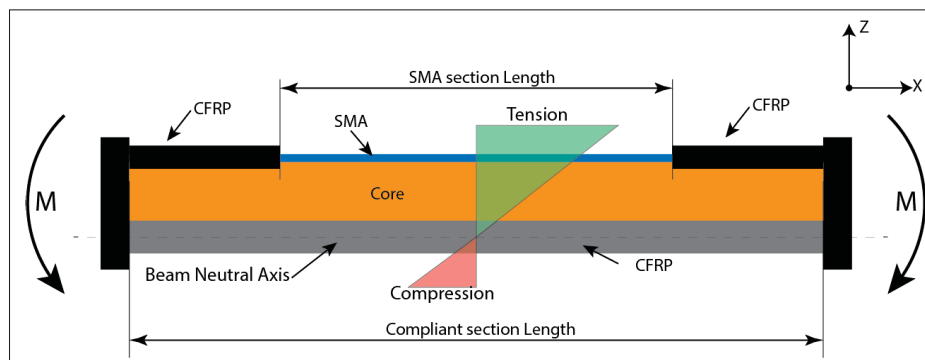
Figure 2.39   Variable stiffness beam section under pure moment

Since the compliant section is defined by the length of the *CFRP*, (L_{cfrp}), and with the idea of making the analysis of the *Compliant Beam* independent of the sections' lengths of *SMA* and *CFRP*, a simplification is applied, where $ratio_{sma} = \frac{L_{sma}}{L_{cfrp}}$.

Independently from the geometrical design, the structural functionality of the compliant section of the hydrofoil is constrained by four main criteria:

SMA Maximum Strain

As any material, *SMA* have the ability to recover their initial state after a deformation. This statement is true only if the maximum elastic strain of the material is respected. Even if the strain capabilities of the alloy are larger than commonly used materials, this parameter is key in the design of the compliant section to avoid permanent plastic deformations on the alloy, and with so, making the hydrofoil not suitable for the intended use and design.

CFRP laminate Failure Index

Following the same idea as with the SMAs, CFRP laminates allow a repeatable elasticity in tension and compression before the first ply failure occurs (Gibson, 2012). This index needs to be chosen accordingly to the design specifications and precautions taken for the application.

Trigger and Maximum Bending Moments

Respecting the maximum failure strains and stresses are key in the process. But for a fully functional *Passive Selective Compliant Hydrofoil*, the geometry changes need to happen at the design specifications load-case.

$Ratio_{sma}$

This relation between the bending section length and the SMA section length modifies the compliance behaviour. This parameter has a direct influence on the three previously described parameters, such as *SMA Maximum Strain, CFRP laminate Failure Index and Trigger and Maximum Bending Moments*

These four parameters are directly influenced by the section and material properties and strictly related to each other.

2.4.3.3 Methodology

Respecting the bending moment at which the hydrofoil starts the non-linear behaviour is key for the concept to be successful. This will determine the precise speed at which the hydrofoil will be able to create the needed lift for the boat to achieve a *Foiling* state. Because of this, the calculations were aimed at determining the *Trigger and Maximum* bending moment for a specific section and the rest of the parameters were considered in a second degree.

To begin, and because of the great non-linearity of SMA, a simplification was done to reduce the complexity of the calculations. With the acquired material properties at 20°C, multiple key points in the *Stress-Strain* relationship were defined, as seen on Figure 2.40.
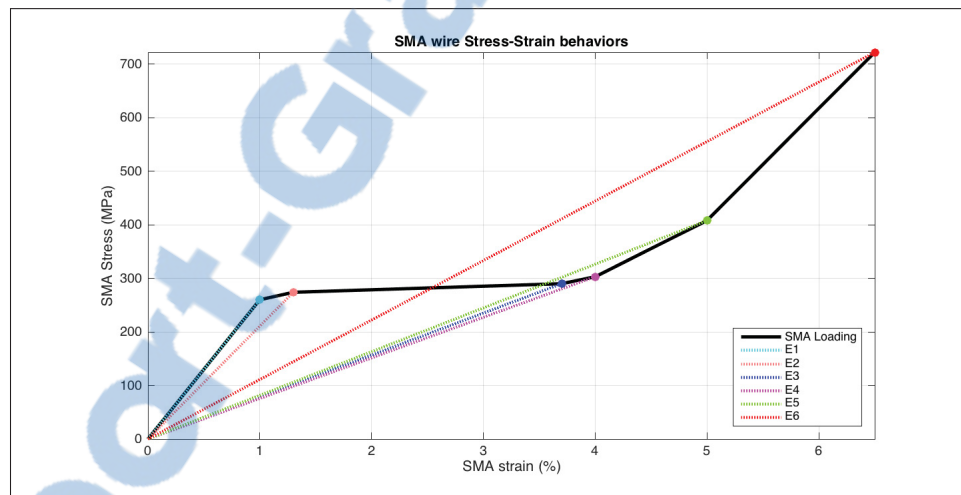
Figure 2.40   Linearized loading beahavior and Elastic Moduli definitions
of Special Metals UDIMET® NiTiNOL SMA wire ⌀ 0.5*mm*

These secant lines, were used to calculate the linear elastic modulus for each defined point on the loading behaviour of the UDIMET® *SMA*. The *key-points* were defined where a considerable change of the material occurs.

Bending moment values for a defined beam section can be easily achieved by applying the *Euler-Bernoulli Beam theory* (equation 2.20), where the composite beam stiffness ($\widehat{EI}_{beam}$) and neutral axis is calculated for a determined SMA stress-strain state and *CFRP* laminate, and with it, the bending moment M_{Beam} value can be directly obtained. This approach can be used when

the cross section of the beam is constant, as seen on Figure 2.38.

$$\varepsilon_{sma} = \frac{M_{Beam}\,\bar{y}_{sma}}{\widehat{EI}_{Beam}} \quad \Rightarrow \quad M_{Beam} = \frac{\widehat{EI}_{Beam}\,\varepsilon_{sma}}{\bar{y}_{sma}} \tag{2.20}$$

Unfortunately, when the length of the SMA section (L_{sma}) is shorter than the CFRP section (L_{cfrp}), the lengthwise cross-section of the beam is no longer constant and *Euler-Bernoulli Beam theory* can not be directly applied, hence a more elaborated method was developed. Based on the *Beam Section Equilibrium*, a set of equations was derived from a FBD (free-body diagram) presented on Figure 2.41 to obtain a relation between the *Bending moment*(M_{Beam}), the ε_{sma} and the *ratio$_{sma}$* as expressed in equation 2.21.

$$M_{Beam} = f_{(\varepsilon_{sma},\ ratio_{sma})} \tag{2.21}$$

For this analysis, the *Foam Core* stiffness was neglected, as its function consists only of keeping the spacing between the *CFRP* and *SMA* constant under load. It was also considered that the *SMA* member can freely slide over the core, and no shear-load is transferred. With that in mind, and assuming the equilibrium, a set of equations solving the problem was developed.
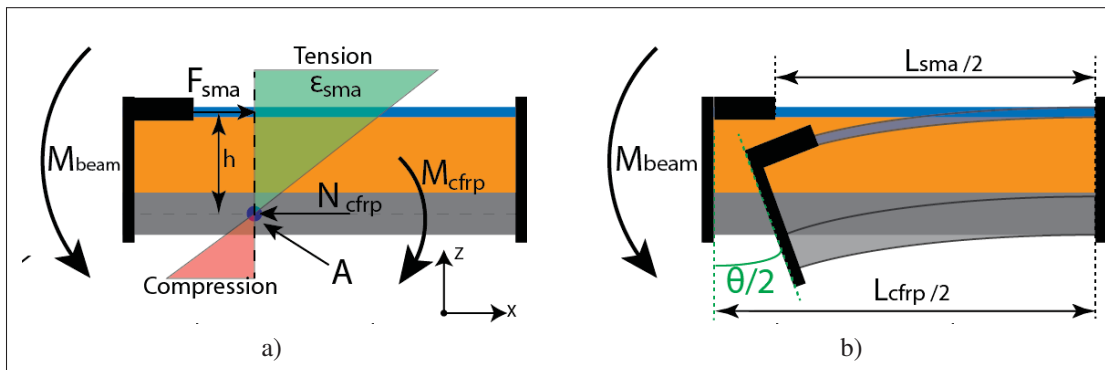
Figure 2.41   FBD of symmetric composite beam under pure-bending
(a) Applied and reaction forces, (b) Deformation angle θ under load

Beginning with the equilibrium of forces on the x axis and a sum of moments at point A in Figure 2.41a, equation 2.22 and 2.23 can be derived.

$$\sum F_x = 0 \Rightarrow F_{sma} = N_{cfrp} = \sigma_{sma} \, S_{sma} = E_{sma} \, \varepsilon_{sma} \, S_{sma} \tag{2.22}$$

$$\sum M_A = 0 \Rightarrow M_{Beam} = M_{cfrp} + M_{sma} = M_{cfrp} + (F_{sma} \, h) \tag{2.23}$$

Then, based on Figure 2.41b, the strain on the *SMA* (ε_{sma}) can be expressed by equation 2.24, where μ is the CFRP axial deformation.

$$\varepsilon_{sma} = \frac{\Delta L_{sma}}{L_{sma}} = \frac{h\theta - \mu}{L_{sma}} \tag{2.24}$$

Based on the strength of materials theory, the beam rotation θ and CFRP axial deformation μ can also be expressed by:

$$\theta = \frac{M_{cfrp} \, L_{cfrp}}{\widehat{EI}_{cfrp}} \tag{2.25}$$

$$\mu = \frac{N_{cfrp} \, L_{cfrp}}{\widehat{EA}_{cfrp}} \tag{2.26}$$

Considering the previous equations, equation 2.24 can be rearranged as:

$$\varepsilon_{sma} = \frac{h\theta - \mu}{L_{sma}} \Rightarrow \varepsilon_{sma} \, L_{sma} = h\theta - \mu \tag{2.27}$$

Replacing equation 2.25 and 2.26 in equation 2.27 yields equation 2.28:

$$\varepsilon_{sma} \, L_{sma} = h \, \frac{M_{cfrp} L_{cfrp}}{\widehat{EI}_{cfrp}} - \frac{N_{cfrp} \, L_{cfrp}}{\widehat{EA}_{cfrp}} \tag{2.28}$$

64

$$\varepsilon_{sma} = h \frac{M_{cfrp} L_{cfrp}}{L_{sma} \widehat{EI}_{cfrp}} - \frac{N_{cfrp} L_{cfrp}}{L_{sma} \widehat{EA}_{cfrp}} \tag{2.29}$$

And by replacing N_{cfrp} in equation 2.29 with equation 2.22 gives:

$$\varepsilon_{sma} = h \frac{M_{cfrp} L_{cfrp}}{L_{sma} \widehat{EI}_{cfrp}} - \frac{E_{sma} \varepsilon_{sma} S_{sma} L_{cfrp}}{L_{sma} \widehat{EA}_{cfrp}} \tag{2.30}$$

$$\varepsilon_{sma} + \frac{E_{sma} \varepsilon_{sma} S_{sma} L_{cfrp}}{L_{sma} \widehat{EA}_{cfrp}} = h \frac{M_{cfrp} L_{cfrp}}{L_{sma} \widehat{EI}_{cfrp}} \tag{2.31}$$

$$\varepsilon_{sma} L_{sma} \widehat{EI}_{cfrp} + \frac{L_{sma} \widehat{EI}_{cfrp} E_{sma} \varepsilon_{sma} S_{sma} L_{cfrp}}{L_{sma} \widehat{EA}_{cfrp}} = h M_{cfrp} L_{cfrp} \tag{2.32}$$

$$\frac{\varepsilon_{sma} L_{sma} \widehat{EI}_{cfrp}}{h L_{cfrp}} + \frac{\widehat{EI}_{cfrp} E_{sma} \varepsilon_{sma} S_{sma} L_{cfrp}}{\widehat{EA}_{cfrp} h L_{cfrp}} = M_{cfrp} \tag{2.33}$$

$$\frac{\varepsilon_{sma} L_{sma} \widehat{EI}_{cfrp}}{h L_{cfrp}} + \frac{\widehat{EI}_{cfrp} E_{sma} \varepsilon_{sma} S_{sma}}{\widehat{EA}_{cfrp} h} = M_{cfrp} \tag{2.34}$$

Finally, by replacing equation 2.34 in equation 2.23 and taking into account that $M_{sma} = h F_{sma} = h E_{sma} \varepsilon_{sma} S_{sma}$, then: $M_{Beam} = M_{cfrp} + M_{sma}$ as shown by equation 2.30:

$$M_{Beam} = \frac{\varepsilon_{sma} L_{sma} \widehat{EI}_{cfrp}}{h L_{cfrp}} + \frac{\widehat{EI}_{cfrp} E_{sma} \varepsilon_{sma} S_{sma}}{\widehat{EA}_{cfrp} h} + h E_{sma} \varepsilon_{sma} S_{sma} \tag{2.35}$$

Using $ratio_{sma} = \frac{L_{sma}}{L_{cfrp}}$, equation 2.35 is rearranged to obtain:

$$M_{Beam} = \varepsilon_{sma} \left(\frac{ratio_{sma} \, \widehat{EI}_{cfrp}}{h} + \frac{\widehat{EI}_{cfrp} E_{sma} \, \varepsilon_{sma} \, S_{sma}}{\widehat{EA}_{cfrp} \, h} + h \, E_{sma} \, S_{sma} \right) \qquad (2.36)$$

With this approach, for any $ratio_{sma}$ calculation, the angle of the beam θ only depends on the length of the compliant section L_{cfrp} and the beam cross-section properties.

2.4.3.4 Tool implementation and scripting

With the developed equation to obtain the bending moment, many other variables, previously described in section 2.4.3.2, also needed to be taken in account.

To begin, the overall geometry of the beam needs to be defined by the user, as well as the material choice and the CFRP stacking sequence. The material database can be used to iterate over different material types efficiently.

With those definitions, a first approximation is done with a simple *Euler-Bernoulli* equation, (2.20), where the desired bending moment M_{Beam} for the *Triggering* of the structure is defined to obtain the Beams' bending stiffness $\widehat{EI}_{Beam}$. At this stage, the first slope of the SMA is used ($E1$ in Figure 2.40).

Based on that target $\widehat{EI}_{Beam}$ value, the script creates a *Look Up Table (LUT)*, as seen on Figure 2.42. The purpose of this is to evaluate the possibilities on the design, where different *SMA* thicknesses and *CFRP* fiber orientations are evaluated to obtain an equivalent $\widehat{EI}_{Beam}$ value. The *SMA* thicknesses are evaluated as a percentage $(\%)$ of the beams height, as seen on the first column of Figure 2.42, with the equivalent number of wires needed and equivalent rectangle cross section thickness on the last column of the *LUT*. Every combination is calculated to evaluate the $\widehat{EI}_{Beam}$ stiffness.

To help the user, the table shows the closest $\widehat{EI}_{Beam}$ value line for every fiber orientation option, as well as the position, under parenthesis. The choices of the user are not limited to the ones shown on the table, this means that any ply angle, as well as any SMA thickness can be freely chosen.

	0 Deg	+/- 5 Deg	+/- 10 Deg	+/- 15 Deg	+/- 20 Deg	+/- 25 Deg	+/- 30 Deg	+/- 45 Deg	Num of Wires	SMA eq. Thickness (mm)
1 % (1)	86.62	86.02	84.19	81.10	76.86	72.04	67.49	59.79	46	0.1500
2 % (2)	120.81	120.19	118.33	115.17	110.83	105.87	101.14	92.98	92	0.3000
2.25 % (3)	128.90	128.29	126.42	123.23	118.86	113.85	109.06	100.76	103	0.3375
2.5 % (4)	137.71	137.09	135.20	132.00	127.58	122.51	117.66	109.18	115	0.3750
2.75 % (5)	145.75	145.12	143.22	139.99	135.54	130.41	125.49	116.83	126	0.4125
3 % (6)	154.48	153.85	151.94	148.68	144.18	138.99	133.98	125.12	138	0.4500
3.25 % (7)	162.46	161.83	159.90	156.61	152.06	146.81	141.72	132.65	149	0.4875
3.5 % (8)	170.42	169.78	167.83	164.51	159.91	154.59	149.42	140.13	160	0.5250
3.75 % (9)	179.06	178.41	176.45	173.09	168.44	163.03	157.76	148.23	172	0.5625
4 % (10)	186.95	186.30	184.32	180.93	176.22	170.73	165.37	155.60	183	0.6000
5 % (11)	219.67	218.99	216.92	213.36	208.39	202.53	196.71	185.81	229	0.7500
Resuls										
Closest EI (N–m2)	154.48	153.85	151.94	156.61	152.06	154.59	149.42	155.60		
Position (line)	6.00	6.00	6.00	7.00	7.00	8.00	8.00	10.00		

Figure 2.42   Compliant Section design *Look Up Table*

Then, continuing on the UI, the user needs to make a choice of fiber orientation as well as SMA thickness percentage, based on the *LUT* values.
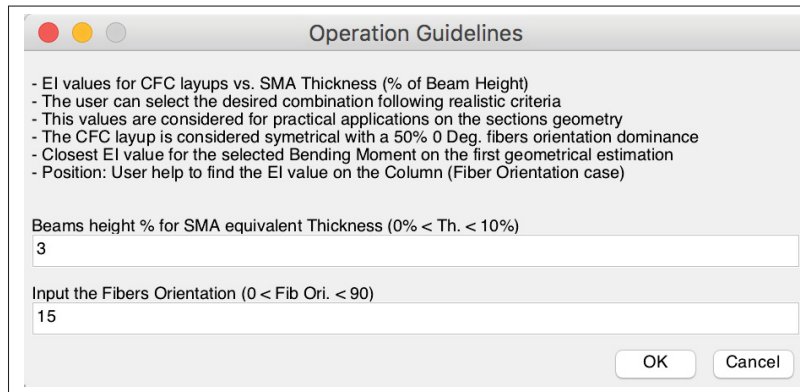
Figure 2.43   Input UI and Operation Guidelines

After selecting the desired SMA thickness and fiber orientations, a validation message appears on the screen (see Figure 2.44).

As a final step, the $ratio_{sma}$ needs to be chosen. This choice is critical to determine the *Trigger* and *Maximum* bending moments for the *Passive Non-Linear Compliant Beam*, as well as the maximum *Tsai-Hill* failure index allowed by design, as seen on Figure 2.45. Once the user has made his choice, the $ratio_{sma}$ is then defined as a percentage, as indicated on the UI, and confirmed by clicking "*OK*".
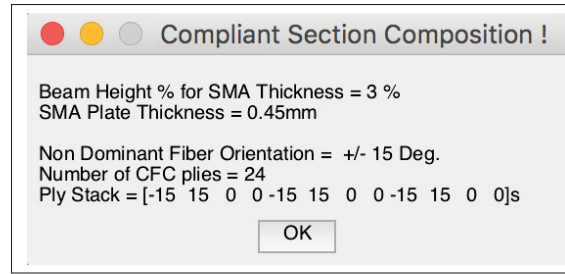
Figure 2.44   Compliant Section Validation
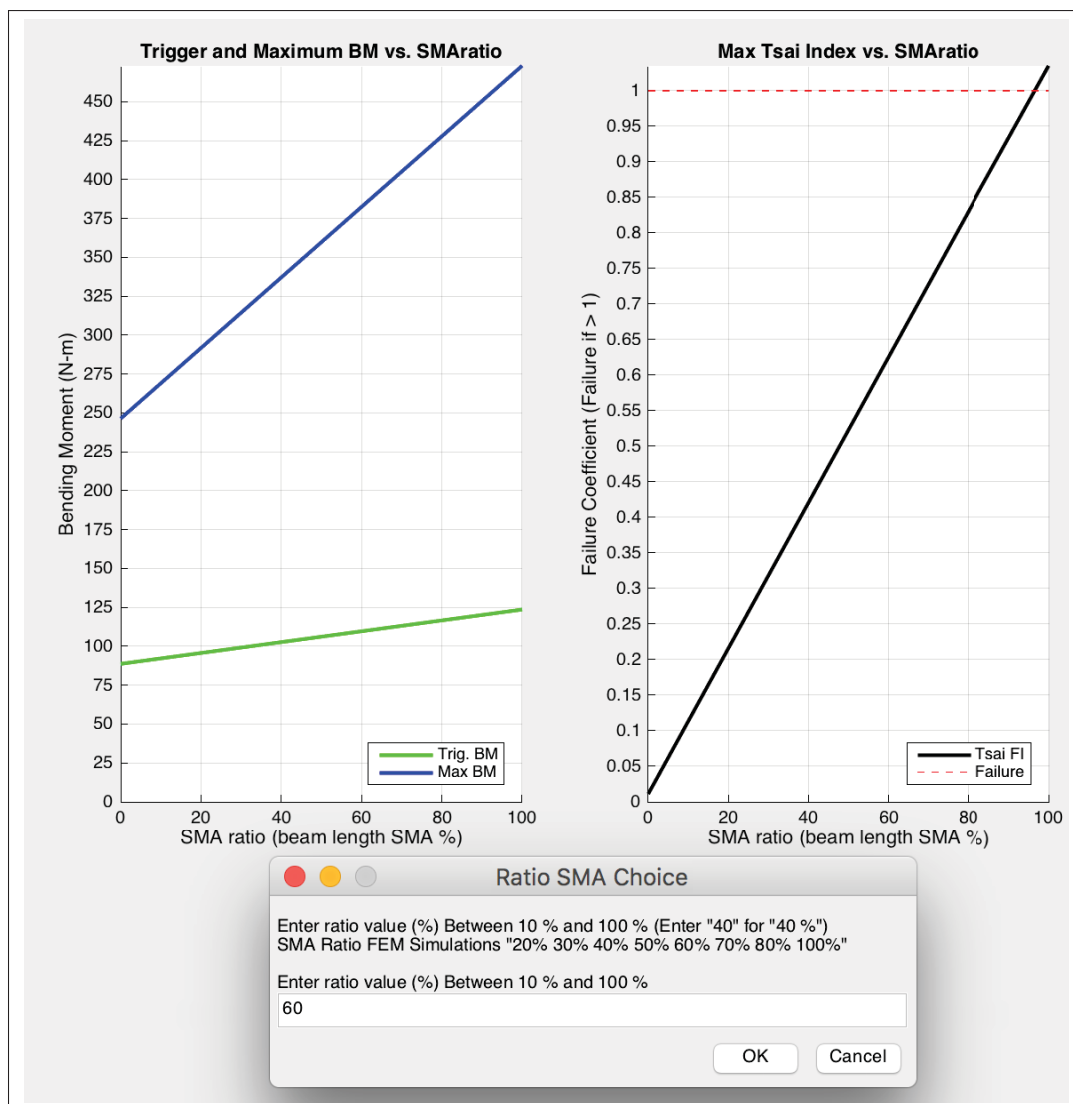
Figure 2.45   *ratio*$_{sma}$ choice and Plotting

Finally, the SMA Beam Tool provides the results as plots (Figure 2.46 as a reference only). The two plots seen on Figure 2.45 were modified with the indication of the chosen *ratio*$_{sma}$ and the equivalent Bending Moments. On the lower section, the *Bending Radius vs. Bending Moment*, *Bending Angle vs. Bending Moment*, ε_{sma} *vs. Bending Moment*, as well as the *CFRP Failure Index vs. laminate thickness*, are shown.

On the bottom images of Figure 2.46, the FEM validation curves can also be seen, for a fair comparison between the preliminary design tool and results of a commercial software. The complete flowchart of the calculations can be seen on Figure 2.47.
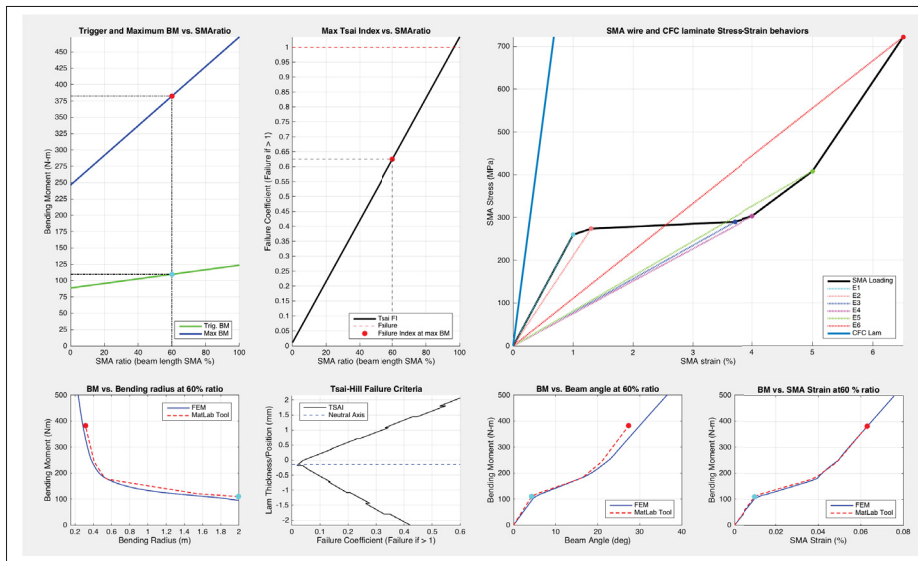
Figure 2.46   SMA Beam Tool final Calculations

The methodology presented in this chapter will be used for the design of the Proof of Concept Prototype (PCP) in Chapter 3, and the design process of the Proposed Design (PD) in Chapter 4. For the PCP design, the SMA Beam Tool is used and the results validated against the finite element model. For the PD, the Non-Linear Beam EI Tool, the Beam CLT Tool, and the SMA Beam Tool are used to demonstrate the complete process for the preliminary design of a Passive-Selective Non-Linear compliant hydrofoil structure.
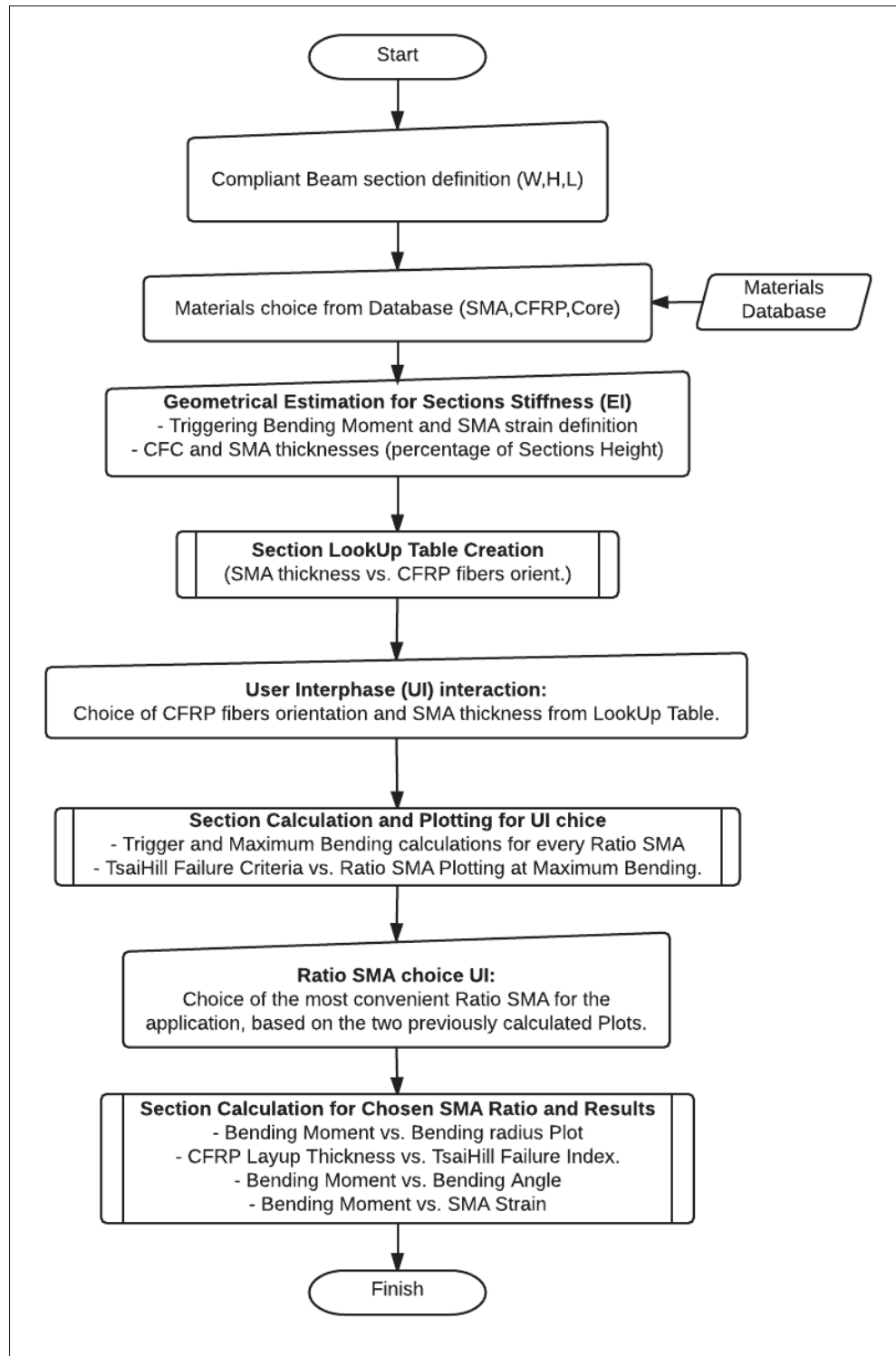
Figure 2.47   SMA Tool Flowchart

CHAPTER 3

PROTOTYPE DESIGN, MANUFACTURING & TESTING

To validate the analytic and numerical design tools used for the *Proof of Concept Prototype (PCP)* design, a structure representing the compliant section of the hydrofoil and the tooling to manufacture were designed, built and tested. The experimental data acquired on a FPB was then compared against the analytic and FEM results.

3.1 Hydrofoil Prototype Design & Manufacturing

3.1.1 Compliant Section Design

The *PCP* was designed to comply with the load-case and geometrical boundaries stated in Chapter 2 of this work. The chosen section of the hydrofoil for the non-linear compliance to happen was at $0.9m$ from the root, where the beginning of the non-linear deformation in the hydrofoil structure happens at a bending moment of $\approx 115 \ Nm$ and the maximum allowed deformation is achieved at $\approx 375 \ Nm$ (see Figure 2.5).

The preliminary design was determined with the *SMA Beam Tool*, described in Section 2.4.3 and validated with the FEM model from Section 3.1.2. One of the goals of this design was to achieve a deflection on the compliant section, so that the *EH1* hydrofoil design becomes a "L/V" hydrofoil geometry once loaded (see Figure 3.2).

The values on Table 3.1 were used for the prototype design calculations, where the beam length was defined to be 1400 mm with a 300 mm compliant section and a $Ratio_{sma}$ of 0.6 (60%), making the length of the SMA section equal to 180 mm, as drawn on Figure 3.1.

Theoretically, the cross section of the hyper-elastic material should be an homogeneous rectangle of 0.45 mm thick by 60 mm (section area of 27 mm^2). In practice, this section was replaced by $\oslash$ 0.5 mm NiTiNOL UDIMET wires, having a *cross-section* area of $\approx$ 0.19635 mm^2. By the division of the theoretical rectangular section area with the one of the UDIMET wire, the number of wires needed for the prototype is equal to 138.
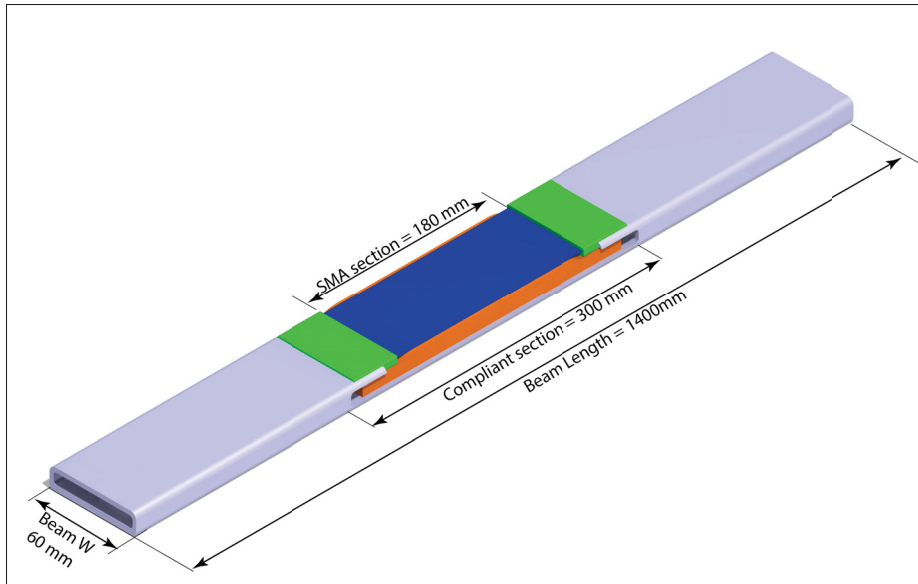
Figure 3.1   PCP CAD with general dimensions

The carbon composite layups were made with a $[\pm15/0_2/\pm15/0_2/\pm15/0_2]_s$ stacking, where the unidirectional tendency of the fibres was mainly chosen to provide in-axis stiffness, with the aim of keeping the compliant section laminate thickness below $1/3$ of the beams height, $(T_{cfrp} < 5\ mm)$.

The criteria for the failure index (FI) of the CFRP section of the PCP being submitted to bending was chosen to be smaller than the aerospace standard. By design, commercial airplane manufacturers use a 1.4 *Safety Coefficient (SC)* for structural carbon-composite parts. The *Failure Index* is calculated as the inverse of the *SC*, in this case becoming $FI = \frac{1}{1.4} \approx 0.71$. In the case of the PCP, the maximum allowed *Tsai-Hill* failure index is calculated to be ≈ 0.625, as seen on the *Max Tsai Index vs SMAratio* plot of Figure 3.16.

The calculations obtained with the previously described design boundaries give a theoretical maximum bending angle of the compliant section of $(\theta/2) \approx 28°$ (Figure3.16), when the maximum bending moment is applied. This value is the half of the total deflection between the two straight CFRP sections; ergo the angle $\theta \approx 56°$ between the hydrofoil straight section and the tip, as seen on Figure 3.2. The summary of the PCP can be seen on Table 3.1.
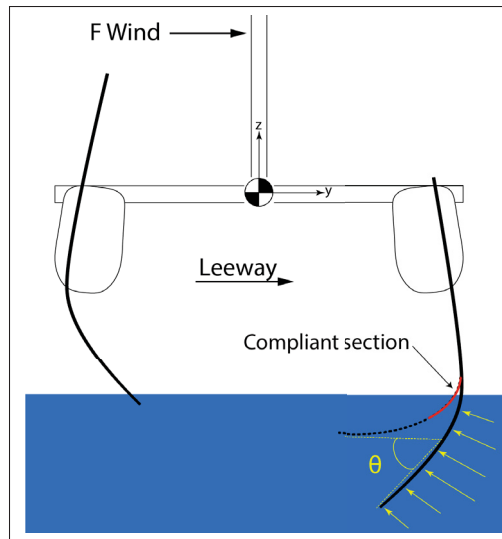
Figure 3.2 Deflected compliant
foil with a 55° angle (θ)

Table 3.1 Prototype geometrical and materials definition

PCP Geom. Parameters	
Beam Length	1400 *mm*
Compliant Length	300 *mm*
Beam Height	15 *mm*
Beam Width	60 *mm*
$Ratio_{sma}$	60% (180 *mm*)
Load-Case	
Trigger BM	115 *Nm*
Maximum BM	375 *Nm*
Material Parameters	
CFRP (Top)	
Ply-Stack	$[\pm 15/0_2/\pm 15/0_2/\pm 15/0_2]_s$(MTM49/34-700)
Thickness	4.32 *mm* (24 *x* 0.18 *mm*)
SMA-CFRP (Bottom)	
SMA Eq. Thickness	0.45 *mm* (*UDIMET* 0.5 *mm* 138 *Wirelengths*)
Ply-Stack	$[\pm 15/0_2/\pm 15/0_2/\pm 15/0_4/\pm 15/0_2/]$(MTM49/34-700)
Thickness CFRP	3.24 *mm* (18 *x* 0.18 *mm*)
Foam-Core	
L x W x T	150 *mm* x 60 *mm* x 7.5 *mm* (min) 8.5 *mm* (max)

3.1.2   Finite Element Model of Compliant Section

3.1.2.1   Motivation

This Finite Element Model (FEM) was developed on *ABAQUS/CAE 6.13-1* with the objective of obtaining high resolution results of the non-linear compliant section structure, where multiple parameters could be extracted from the calculations, as well as to use it as a benchmark validation for the *SMA Beam Tool*, developed on *MatLab* (Section 2.4.3). The model presented on this section is based on the values from Table 3.1, used for the PCP.

3.1.2.2   Materials definition

For the model, three materials needed to be defined, being: CFRP, Foam Core and SMA. For the first two materials, the mechanical properties definition is conventional, as they have a *Hookean* behavior. For the CFRP, lamina properties were used, and for the Foam Core, isotropic properties were defined, while for the SMA, the choice was not as straightforward as for the other two.

Because of the great non-linearity and multi-variable dependence, SMA could not be defined by *Hooks' Law*. For this purpose, Abaqus has a *"(V)UMAT"* material that can be used to simulate NiTiNOL. This script is capable of accounting for the non-linear elasticity and plasticity of the material, the temperature at which it is exposed, the speed of the deformation, as well as the hysteresis on the loading and unloading phases. To use this material model and its properties, an exhaustive material characterization as well as simulation compensations to obtain realistic material behaviors are needed to achieve fairly accurate simulations.

Since the intention of this project is to study the possibility of achieving passive non-linear deformations using embedded SMA, a simpler approach was used, where many variables are considered as constants. With the acquired material properties in section 2.3.3, a *Hyperelastic Marlow* model was chosen to define the material behavior with the *stress-strain* relationship as a Test Data Input.

To validate the consistency between the experimental and FEM behaviour of the Non-Linear material, a plate specimen was put under a tension test. The 10*mm* x 100*mm* x 0.45*mm* specimen was defined (see Table 3.2) with the acquired material properties from the UDIMET® NiTiNOL SMA. The simulation results for this validation specimen can be seen on Figure 3.4.

Table 3.2   SMA Specimen Testing Definition

SMA Specimen Dimensions		
Length	100	*mm.*
Width	10	*mm.*
Thickness	0.45	*mm.*
FEM Boundary Conditions		
Displacement	7	*%*
Element Type	S4R	
Meshing Control	Quad	
Number of Elements	1000	$(100x10)$
Thickness Integration Points	5	
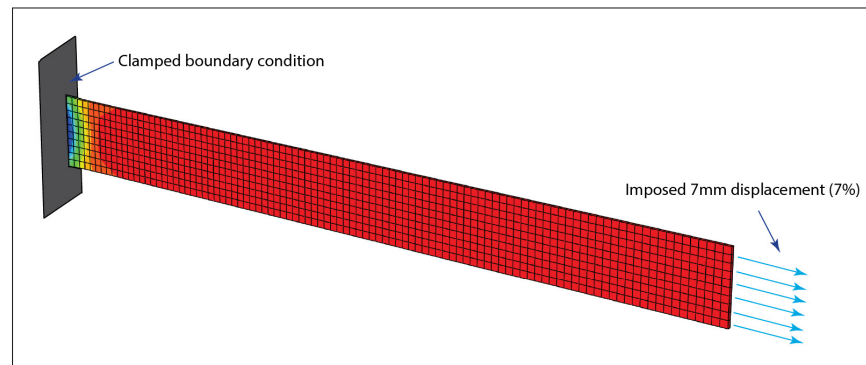
Figure 3.3   SMA material FEM validation

A consideration to be taken in account when working with Non-Linear models on Abaqus, is that the uni-axial Strain values obtained are calculated as $\varepsilon = \ln(1 + (\Delta L/L_0))$, referring to the True Strain. This difference had to be considered when comparing the SMA Beam Tool 2.4.3 with the FEM model engineering strains measurements. This considerations can be found on 3DS-Simulia (2013) section 10.2.2 Stress and strain measures for finite deformation and section 21.1.2 Material data definition.
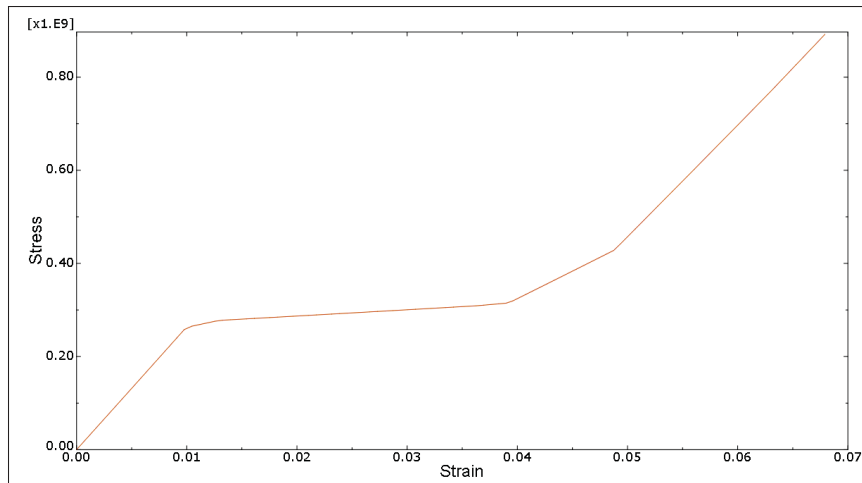
Figure 3.4   SMA material FEM Stress (Pa) - Strain (mm/mm) results

3.1.2.3   Model Design

The model consists of a three part sandwich-like assembly, creating a hybrid *Shell-Solid-Shell* elements composition, modelled in the part design toolbox inside *Abaqus/CAE*. For explanation convenience, the measurements used on this *Generic* model are the overall dimensions for the case study. To begin, the full beam length was defined as 1400 *mm* and 300 *mm* for the compliant section length (L_{cfro}), while the cross section dimensions were taken from the prototype definition, in section 2.3, being 15 *mm* and 60 *mm* for height and width, respectively. To simplify the analysis, the 4 *mm* corner radius (Figure 2.11) on the outer edges of the cross-section were neglected and kept as a sharp edge.

The load case for the FEM study was considered as a Pure-Bending Moment applied by a *FPB* load introduction on the outside of the compliant section, as seen on Figure 2.10.

To reduce the number of elements in the calculation, and to achieve faster results, conventional FEA methodology for a FEM simplification was applied.

The compliant section was *"shortened"* by the application of a symmetry plane cut was made on the $[Y - Z]$ plane (red plane on Figure 3.5), making the analysis on one half of the structure and a second plane cut at the end of the compliant section, 150 *mm* offset from the symmetry plane (green plane on Figure 3.5).
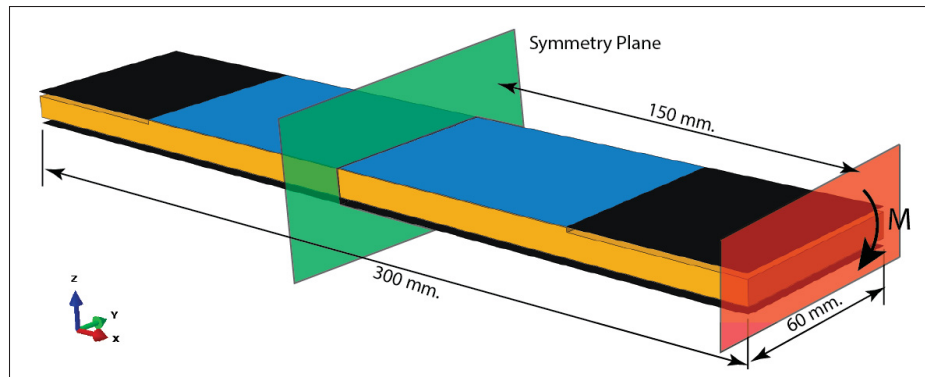
Figure 3.5   FEM compliant section with sym. planes and dimensions

Three parts are needed to compose the compliant section assembly (see Figure 3.6). The CFRP section, under axial compression and composed by a layup, as well as the *SMA-CFRP* section, under tension were defined as 60 *mm* wide by 150 *mm* long *3D Shells*. On the tension side, a shell partition was made to define the two materials on the model, being SMA on the symmetry plane side, and CFRP on the load application side. Because of the different thicknesses on these last two materials, the geometry of the *Foam Core* modelled as a *3D Solid* (yellow) needed to be defined with a specific geometry to avoid elements clashing and increase the model convergence. The shell elements were used on the layer-like members, *CFRP* and *SMA*, where the transverse compression information was not needed to be studied. On the other hand, solid elements needed to be used for the Foam Core to evaluate the compression between the CFRP in compression and the SMA in tension, as this member is responsible to keep the SMA at a constant height, under bending load.
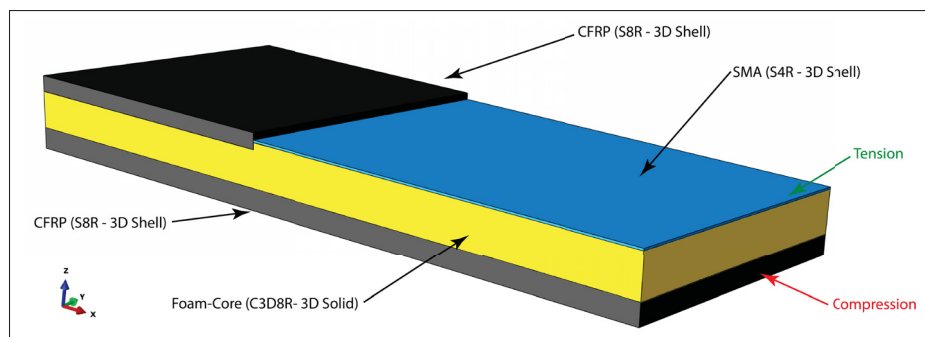
Figure 3.6   FEM model with rendered shell elements

3.1.2.4 Boundary Conditions

The boundary conditions on the model were defined as similar as possible to the real situation. The *contact* condition between the shell elements and the solid were defined as *Friction-less* and *No-penetration* was allowed. With these properties, the foam core could freely slide in-between the elements, being mostly submitted to compression.

As shown on Figure 3.7, the *DOF* on the nodes exposed to the symmetry plane were defined as fixed on the three rotations X, Y, Z as well as the longitudinal direction, normal to the symmetry "X". With this method, the materials have the possibility to contract/expand when loaded at the *symmetry plane*. Three *Reference Points* were defined in the CFRP, Foam Core and SMA elements individually. To fix the model in the space, the one on the composite laminate, was fixed on the "X, Y, Z" displacements. For the two others, only the "X, Y" displacements were fixed, allowing the displacements on the nodes along Z.

The bending moment load introduction is applied on a *Reference Point*, coupled with a *kinematic coupling* to the red plane (see Figure 3.7). The coupling between the reference point and the plane only allows the *x* and *z* displacements, as well as the rotations around the *y* axis, fixing the other DOF.
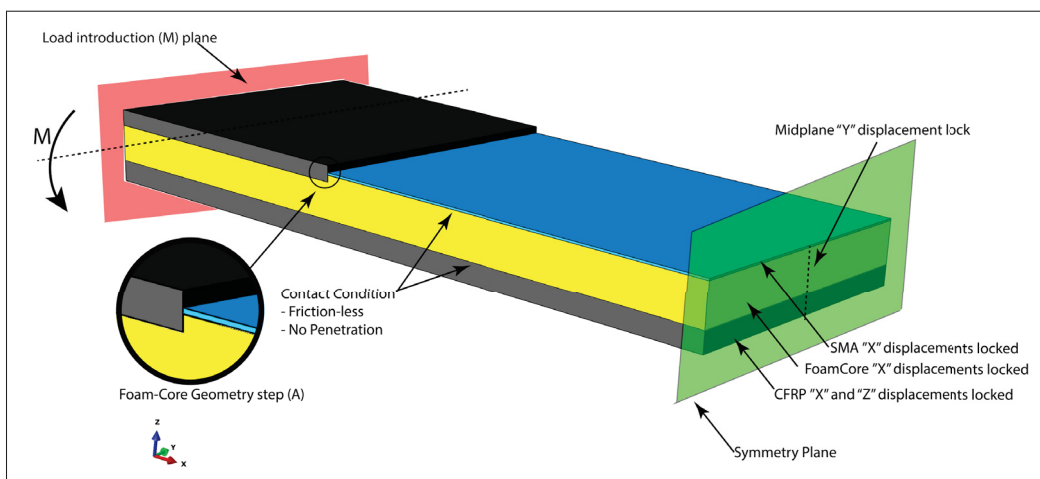
Figure 3.7   FEM Boundary conditions

3.1.2.5   Elements Definition, Meshing and Convergence

The elements on the model were chosen following a conventional methodology. The *CFRP* members were defined as *S8R* shell elements, as this 8-node element is more suitable for layups than the standard *S4R* 4-node shell element. For the *SMA* member, the choice is limited as the *Hyper-elastic* material properties only allow an *S4R* element definition. Finally, the foam core elements were defined as solid C3D8R, allowing the compression evaluation between the two shells. Because of the high deformation of the *Foam-Core*, the *Arbitrary Lagrangian-Eulerian (ALE)* method was used to reduce the distortion in the mesh during the calculations. This method has the ability of re-meshing the parts at every iteration step, having the advantage of much better convergence results, with the obvious trade-of a greater calculation time. The representation of this approach can be seen on Figure 3.8, where the *ALE* and the Lagrangian techniques are compared on a *die-molded* part simulation.
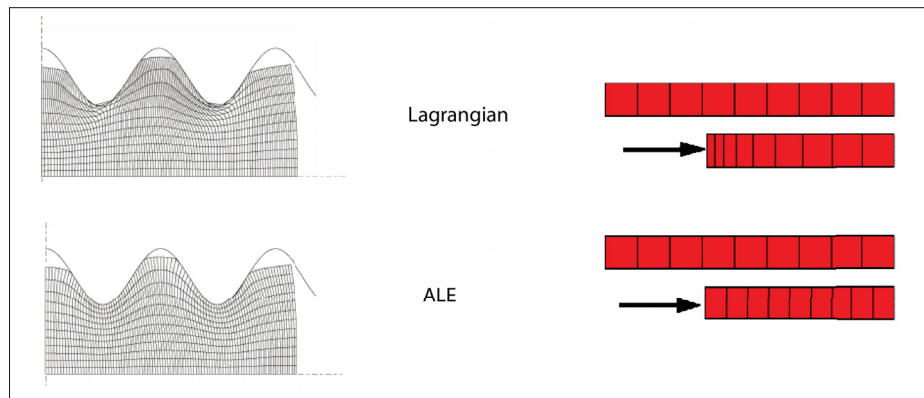
Figure 3.8   ALE and pure Lagrangian meshing representation
Adapted image from www.3ds.com

The meshing of the parts was defined after a convergence study, and since the geometry is relatively simple, an *Hex-Dominated* meshing control was chosen. To begin a 10 *mm* seeding was defined in the shells and a 15 *mm* seeding was defined for the solid parts. By reducing by 1 *mm* at every iteration, the convergence results were stable on with the shell elements at 2 *mm*, while for the solid elements a 5*mm* square seed on the $[X - Y]$ plane and a 2*mm* seeding on the $[X - Z]$ plane were found to be acceptable.

The thickness and positioning of the elements was defined by considering the ply stack at the *Middle Plane* and nominal thickness's for the Shell members, and the Foam-Core dimensions were calculated accordingly to fill the space in between. With these considerations, the model parts were defined as presented on Figure 3.9 where the raw model with the mesh is presented and Figure 3.10 where the thickness representations are shown.Table 3.3:
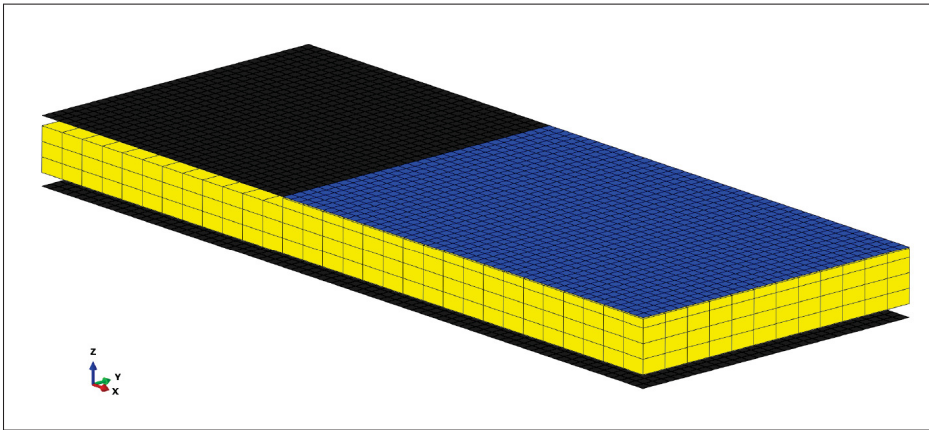
Figure 3.9   FEM model assembly with mesh
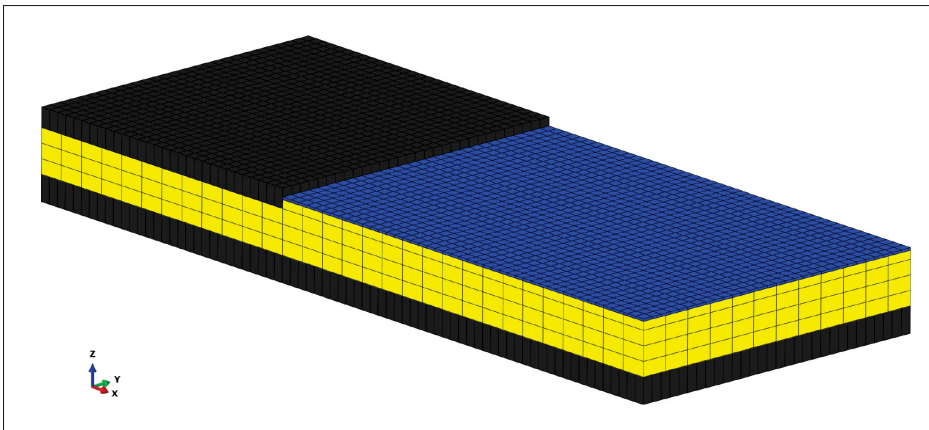
Figure 3.10   Rendered FEM assembly model

Table 3.3   FEM elements definition

CFRP (Top-Side)		
Length	150	*mm.*
Width	60	*mm.*
Element Type	Lamina	Shell S8R
Meshing Control	Quad-Dom.	
Number of Elements	2250	
Thickness Integration Points	5	
SMA-CFRP (Bottom-Side)		
Length	150	*mm.*
Width	60	*mm.*
Element Type SMA	Isotropic	Shell S4R
Element Type CFRP	Lamina	Shell S8R
Meshing Control	Quad-Dom.	
Number of Elements	2250	
Thickness Integration Points	5	
Foam-Core		
Length	150	*mm.*
Width	60	*mm.*
Element Type	Isotropic	Solid C3D8R
Meshing Control	Quad-Dom.	*ALE*
Number of Elements	1656	

3.1.2.6   Results and Data Extraction

The data extraction was done with a *Macro* sequence for convenience. While the load introduction *(M)* was done in a full 1 *second*, the steps needed to achieve the convergence were forced at 0.01 *seconds*. With this, the applied bending moment is calculated by a simple multiplication of the *timestep (t)* and the maximum BM_{max}, expressed in equation 3.1.

$$BM_{(t)} = t \; BM_{max} \tag{3.1}$$

The extracted outputs were the ε_{sma}, the rotation angle θ in radians, the *Tsai-Hill* failure index on the *CFRP* laminate under compression and the maximum compression stress on the Foam Core. Since the shells were defined with 5 integration points, the extracted values were averaged.

On Figure 3.11, the in-plane principal averaged strain is shown. For this study, the focus was put on the ε_{sma}, represented in orange and where the larger deformations happen. The strain gradient is shown at the interphase edge, between the CFRP and the SMA.
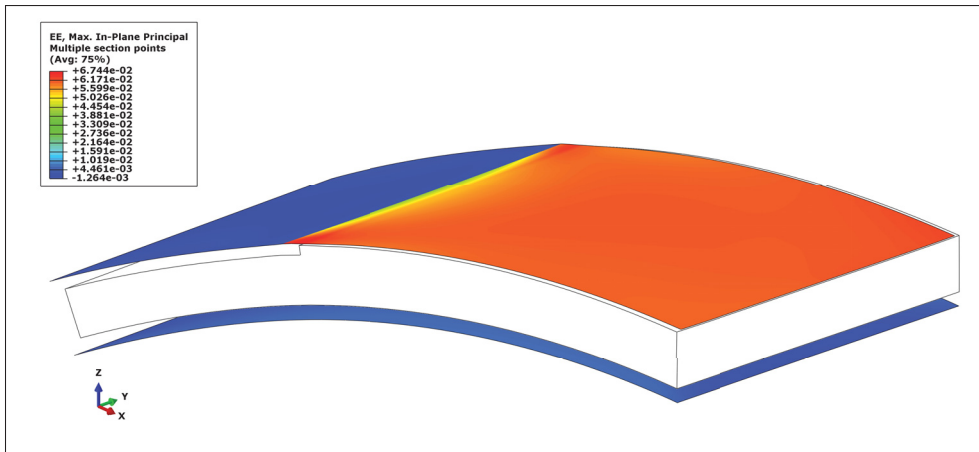
Figure 3.11   In-plane principal strains (mm/mm) on FEM model at 375 Nm

The load introduction plane was used as the beam rotation output. On Figure 3.12, the gradient in red shows the maximum achieved angle (in radians).
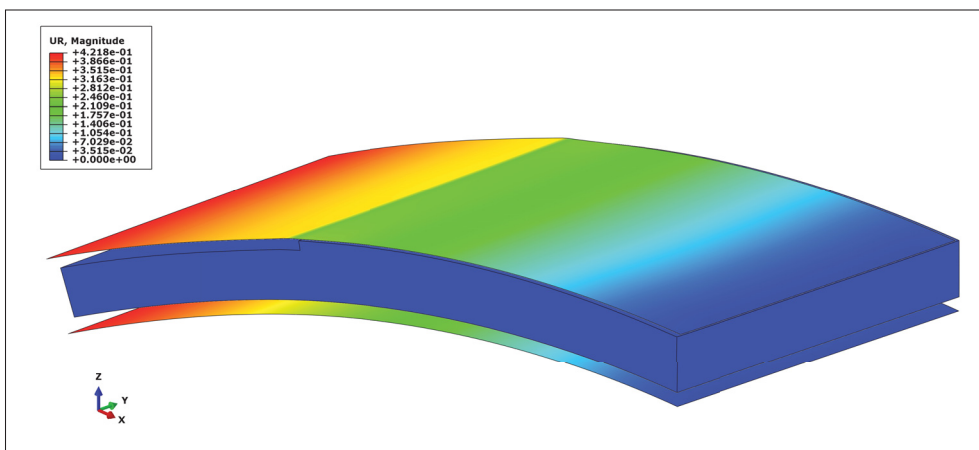
Figure 3.12   Maximum nodal rotation (rad) on FEM model at 375 Nm

The evaluation of the Tsai-Hill criterion is shown on Figure 3.13, where the maximum values are obtained, as expected, on the compression CFRP member.
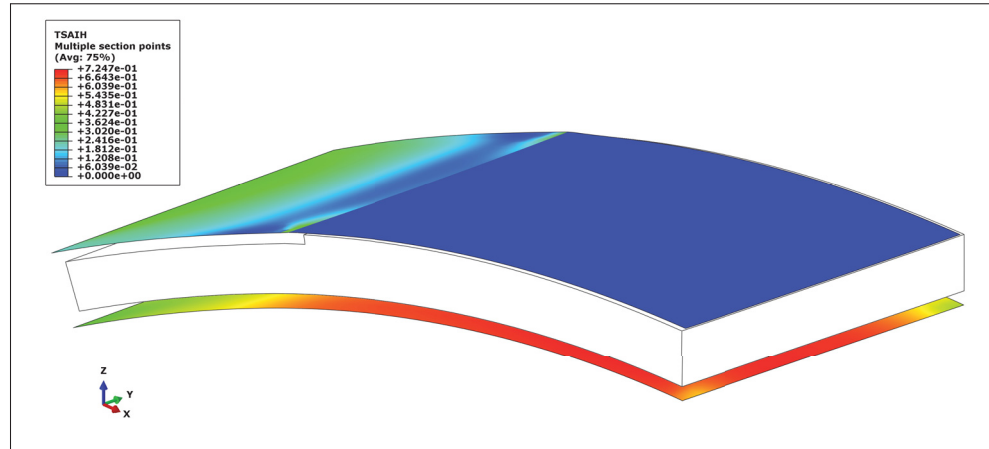
Figure 3.13   Tsa-Hill criterion representation on FEM model at 375 *Nm*

The last evaluation on the model was the pressure between the SMA and the Foam Core to determine the eventual failure of the foam under loading. For an easier representation, the values shown on Figure 3.14 are in the SMA reference (SNEG).
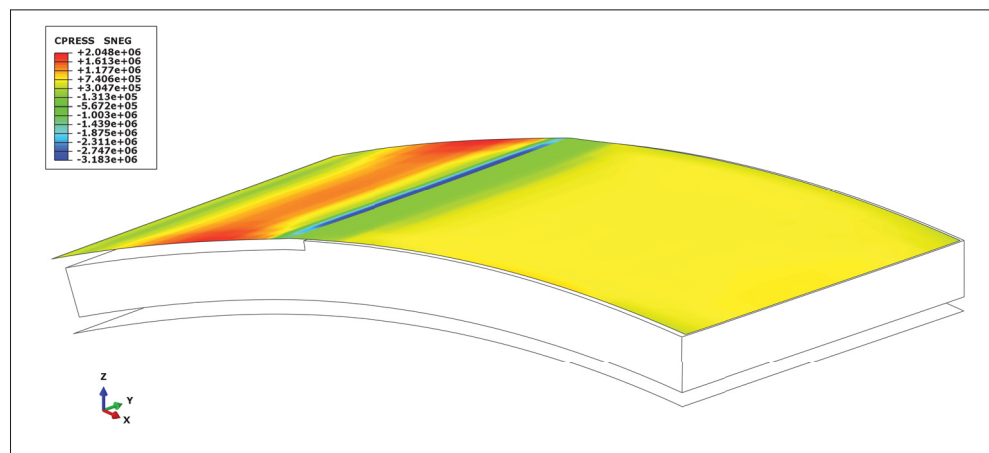
Figure 3.14   Core compression (*MPa*) on FEM model at 375 *Nm*

The final result from the *FEA* can be seen on Figure 3.15 where the *Mises* stresses are represented. These extracted results will be used and compared against the analytic tools on Chapter 3 for the *PCP*.
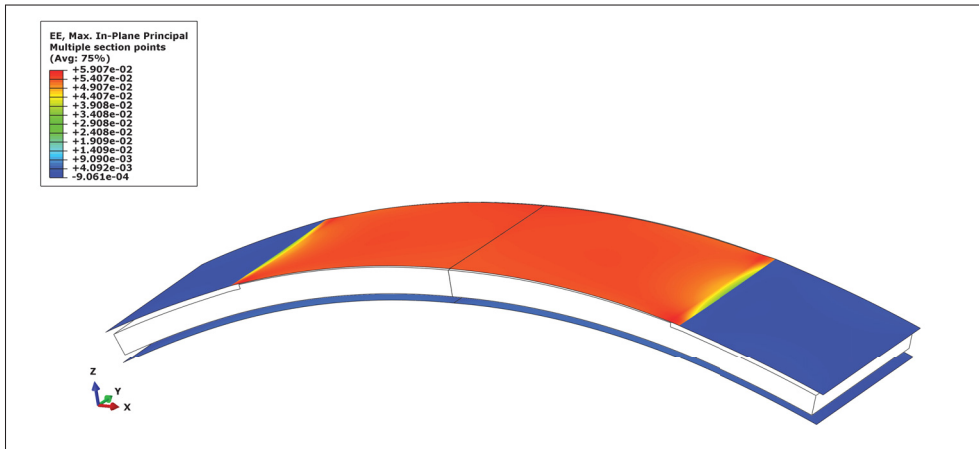
Figure 3.15   FEM beam with symmetric representation

The results seen on Figure 3.16 represent the evaluation of the compliant section defined on Table 3.1. The two first images representing the *SMA Beam Tool* design results for the bending moment and failure index, while the four images in the bottom are the comparison between the analytic tool and the FEM results of the beam deflection *Bending Radius*, the Tsai-Hill failure index on the CFRP, the beams' *Bending Angle ($\theta/2$)* and the SMA strain through the loading. While the Bending Radius and Bending Angle have a slight error between the models, the SMA strain evolution has a high correlation, this being the most important factor along with the failure index to ensure the integrity of the compliant beam section.
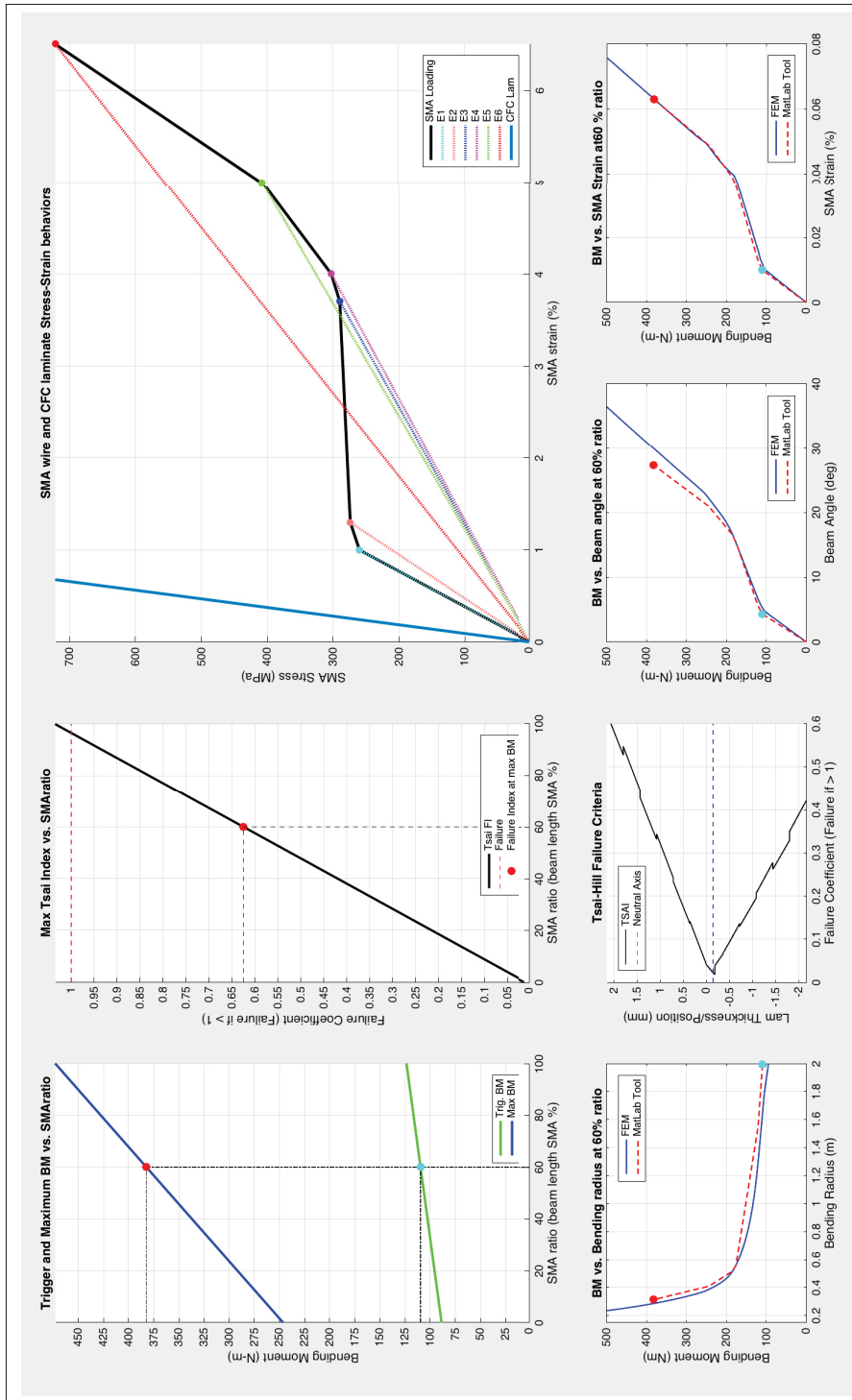
Figure 3.16   SMA Beam Tool Calculation UI results for PCP

3.1.3   Mold design & Manufacturing

To manufacture the *Proof of Concept Prototype (PCP)*, an aluminum two-piece closed mold (Figure 3.17) was designed as part of this work. The main objective was to have the possibility of an *Out Of Autoclave (OOA)* processing of the carbon composite and have no joint on the manufactured beam. Also, for ergonomic reason, the design was made for a *one-person* handling, to allow for flexibility during the ply layup, and de-bulk steps.
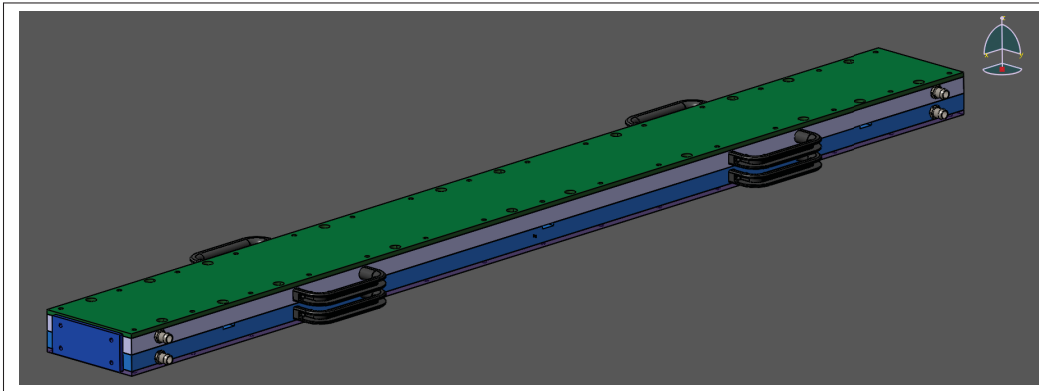
Figure 3.17   Mould CAD model

For an OOA composite process, two main parameters need to be precisely controlled, being the *temperature rates* to polymerize the composite matrix, and the *pressure*, to ensure a proper compaction of the part during the *curing* process. The maximum temperature needed for the mould to cover a large spectrum of pre-preg materials was defined at 160 °C, and the maximum internal pressure was set to 6 *bar*, a commonly used pressure for processing composite parts in an autoclave.

Many options are available to control the processing temperature range, from electrical heating mats, to ovens, to heated oil-based systems, just to name a few. In this case, and because of the expertise of the *FHNW-IKT* laboratory, a *HB-THERM temperature control unit* was used. These water-based systems are able to provide great temperature lapse-rate and stability through embedded serpentine-like heating channels.

To achieve the maximum process temperature with a water-based heating system, the fluid needs

to be pressurized to remain in a liquid phase (see Appendix III). For this case, to have liquid water at 160 °C, a pressure greater than 5.5 *bar* is needed in the serpentine-like heating channel. This enclosure, composed by three channels on each side of the mould, was created by 6 *mm* thick aluminium plates and a 5 *mm* silicon gasket to ensure the sealing.

With a similar idea, and to prevent a resin migration to the outside of the mould during the process, a silicon gasket was installed on the bottom half mould. A general cross-section description can be seen on Figure 3.18. For the design details, please refer to Appendix II.

To ensure a safe and peaceful environment at the*FHNW-IKT* facilities by assuring the proper enclosing of the high temperature pressurized fluid, the *Safety Factor* was kept above 4 (*SF* > 4) for all calculations.
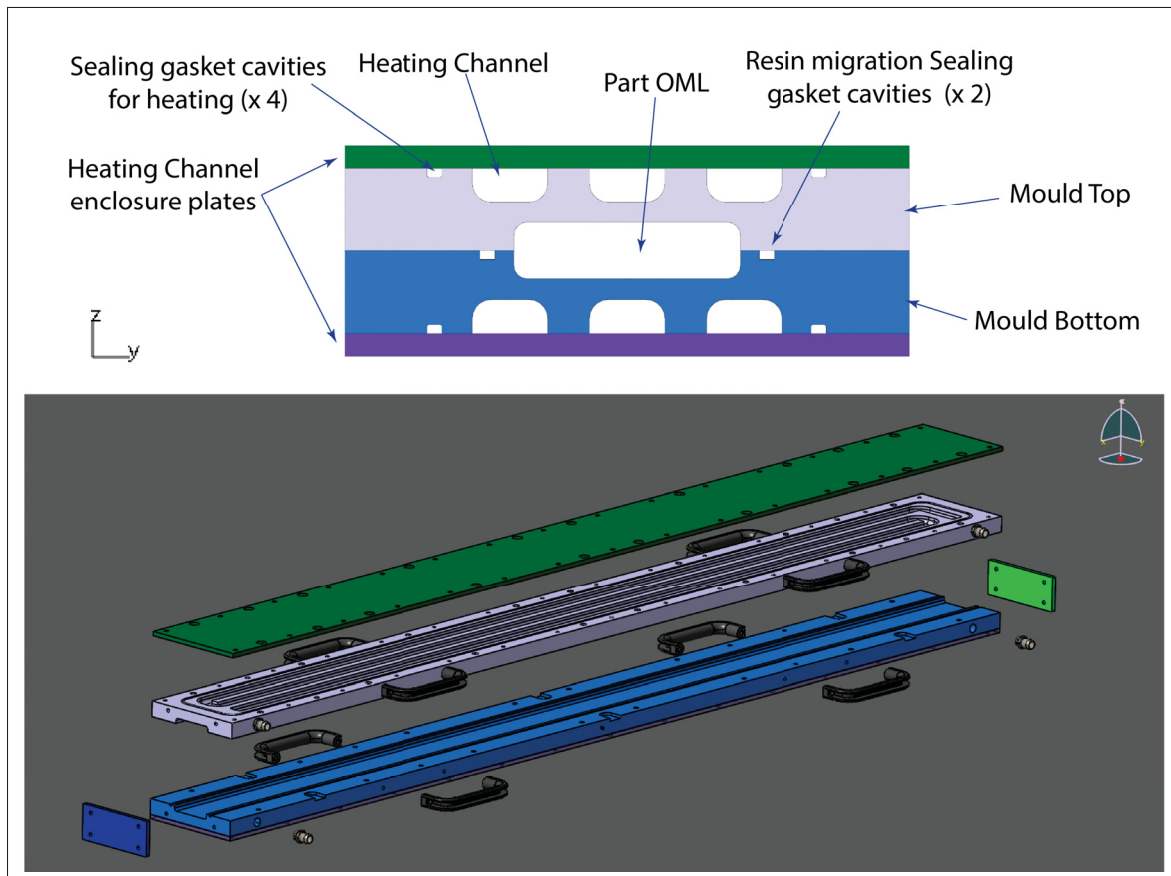
Figure 3.18   Mould cross-section & Exploded view

With the objective of a reduction of the processing steps to obtain the finished part, the use of an overlapped *Scarf Joint* technique was used to join both halves at the beams *shear-web*, and with so, obtain a one-piece *Co-Cured* CFRP part (see Figure 3.19). With the part's OML (Outter Mould Line) geometry being symmetrically through the $X - Y$ mid-plane, a longer flange on the bottom side creating the joint with the top-side section is assembled to the bottom side layup. Then, when the mold is closed and the internal bladder put under pressure, the scarf joint overlaps with the top section laminate and creates the *Co-Cured* joint.
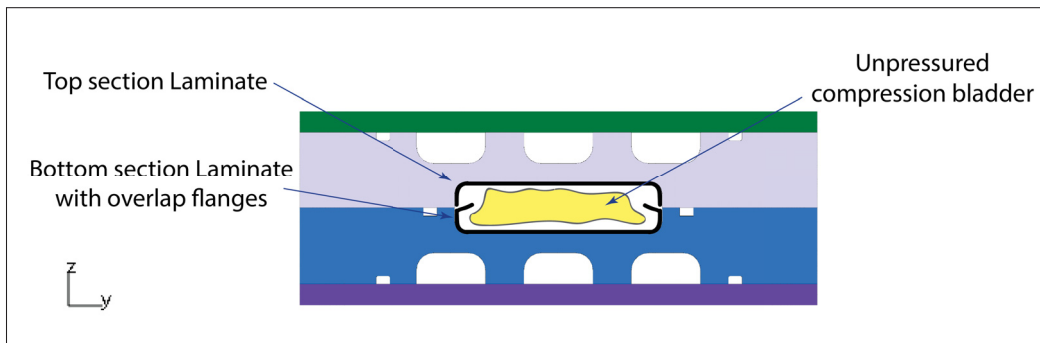
Figure 3.19   Co-Curing and Scarf joint technique representation
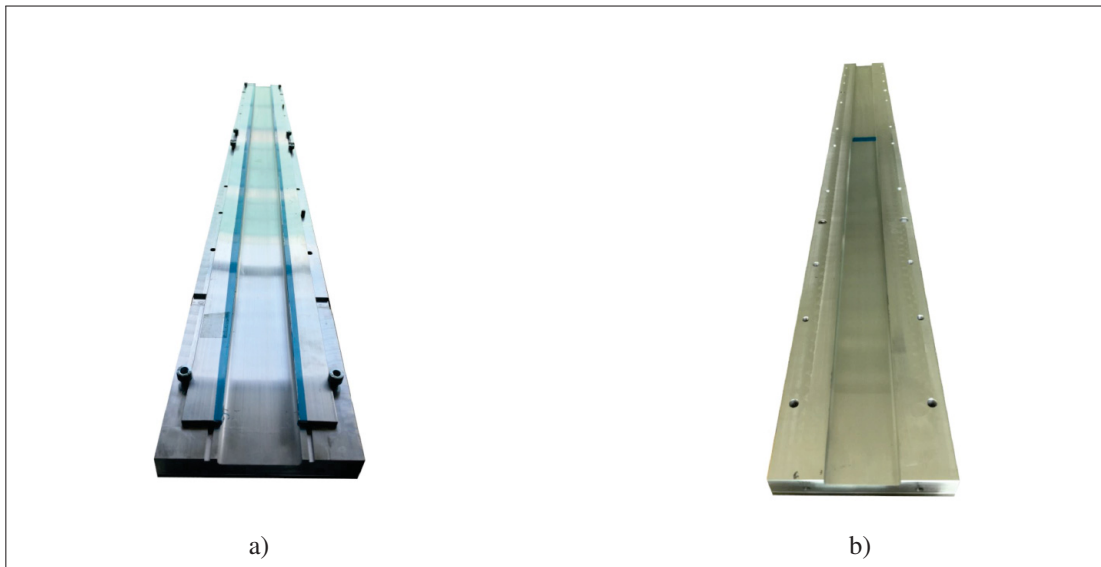
Figure 3.20   OOA Mould parts
(a) Bottom-side mould, (b) Top-side mould

3.1.4 Compliant Beam Manufacturing

To obtain the prototype beam, a two stages process was engaged. First, the CFRP beam was manufactured following the previously calculated parameters and proposed techniques. Then, the SMA wires were installed on the side of the beam submitted to tension.

3.1.4.1 CFRP Beam Manufacturing

To produce a beam structure as close as possible to the calculated parameters and geometry, a CAD fibre-composite layup model was created on the *Composites Design* toolbox on *CATIA V5R20*. With this tool, and the mold *OML* geometry, it is possible to create a composite layup with defined stacking sequences, ply-drops and laminate transitions for non-homogenised layups. Once the *composite CAD design* was finished, a *DXF* file was exported with the precise dimension of every ply for CNC processing. In this case, the *MTM49/34-700* pre-preg fibre was tailored on a *ZUND G3 Digital Cutter* at the *FHNW-IKT* facilities. This efficient process ensures a better ply-cut orientation and most of all, increases speed and precision while reducing scrap waste.

With the *pre-preg* plies cut and sorted-out, the molds already treated with a composite release agent, the layup process began. Because of the small radius on the beams *OML* edges, a 10 minute first ply de-bulk was done on each of the mold sides, followed by one 10 minute de-bulk every three plies.

To have a better support on the *Scarf Joint* flanges, two 5 *mm* aluminum flat bars were installed on the side of the mold, as seen on Figure 3.21a. These bars became the laminate top edge reference for the stacking, as well as the support during the de-bulk process. Once the stacking and final de-bulk process was finished, the aluminum supports were removed from the mold. Even though a 24-ply stack is defined on the beams bottom side, only the first eight (8) compose the *Scarf Joint*.
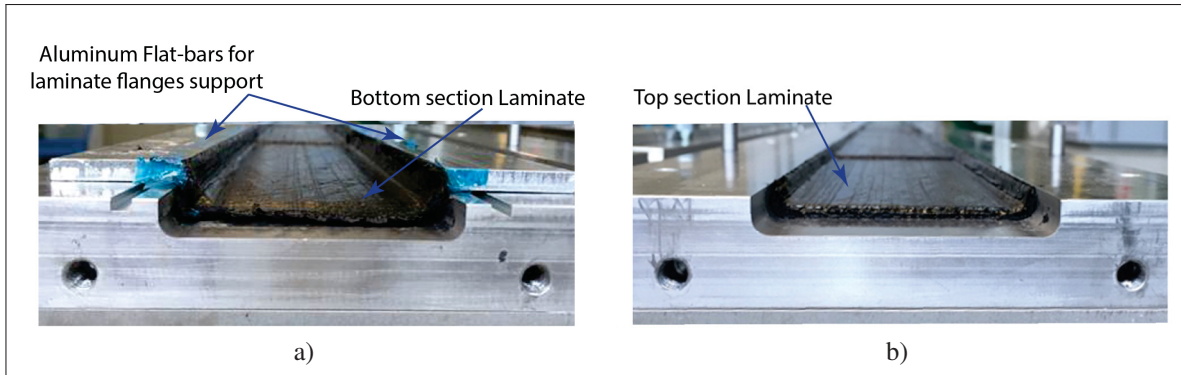
Figure 3.21   Mold halves with stacked plies
(a) Bottom-side mold, (b) Top-side mold

The following step in the process was the installation of a release film over the last ply, to ensure an easy deployment of the internal bladder when pressurized. The release film installed on the top side mold, seen on the right side of Figure 3.22, was kept shorter on the edges to prevent an interference with the flange overlapping from the bottom laminate. To ensure a good positioning of the films until the installation of the bladder, a final de-bulk was done.

Figure 3.22   Release film installed above the last ply

The final step on the process was the bladder installation on the bottom section (Figure 3.23), making sure the overlap flanges stay above of it, until the two mold sections were positioned for a final validation, and closed to proceed with the curing.
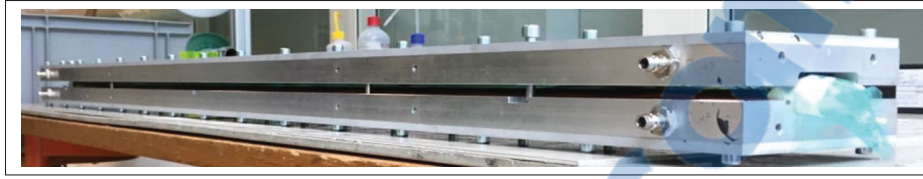
Figure 3.23   Bladder installed in the mould

After a 90 *min.* curing cycle at 135 °C, as specified on the *MTM49* resin Data-Sheets (see Appendix I-3), the composite part was demolded. The bladder and release films were removed, a visual inspection, as well as a *tap-test* were done to inspect potential failure zones, specifically on the *shear-webs*. With these tests passed, the last step was the trimming of the SMA section, as well as the *shear-web* to comply with the designed prototype dimensions.

3.1.4.2   SMA Wires Installation

With the trimmed beam, the process of installing the *SMA* wires could start. Knowing that 138 wire lengths of 180 *mm* (as defined on Table 3.1) were installed with a *Pin-Loaded Strap* technique as described in Section 2.3.3. The full wire length was *Trained* for 60 *cycles*, ensuring a homogeneous pre-strain treatment. The images on Figure 3.24 show the installation on the tensile machine, as well as the close view of the ⌀25.4*mm* (1*in.*) respectively.

With 62 wire lengths installed on the tensile machine, and assuming that $\varepsilon = 7\%$, based on the material characterization on Section 2.3.3, the maximum stress is expected at 750*MPa*. Equation 3.2 was used to obtain the force limit on the system to prevent potential plastic deformation on the wires when under a load of 9.13*kN* during training.

$$F_{max} = Wire_{num} \; Wire_A \; \sigma_{max} \; \Rightarrow F_{max} = 62 \; \pi \; (0.5mm)^2 \; 750MPa \; = \; F_{max} = 9.13kN \quad (3.2)$$

Prior to the wires installation in the prototype, the *Pin Loaded Strap* system was dimensioned to carry the loads to which it would be submitted. With the same calculations from equation 3.2 but with a $Wire_{num} = 138$, a potential force F_{max} of 20.5*kN* was calculated at maximum stress.
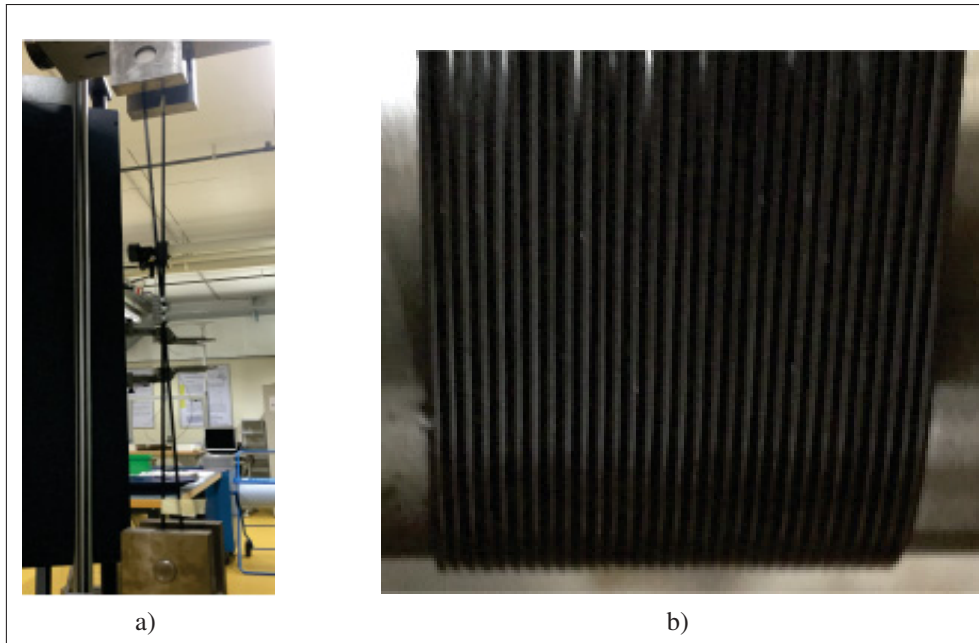
Figure 3.24   SMA Wire for PCP training
(a) Complete setup of wire training, (b) Close up view of wires (31 per side)

Following the equations from (Schürmann, 2007), and considering the small space available to install the strap, a 4*mm Pin* with a 1*mm* CFRP laminated *strap* was used. For these calculations, the F_{max} load was multiplied by the 1.4 safety factor to assure the attachment integrity. The results before trimming can be seen on Figure 3.25.

Figure 3.25   Pin Loaded Strap installed on CFRP beam

With the wire attachment system in place, four symmetrical *strips* were trimmed into the system. This allows the wires to pass around the *Pin*. While 138 wire lengths were needed, the wire was passed 17 times on each *strip*, as seen on Figure 3.26.

Figure 3.26   SMA wires installed on the PCP

This method is far from ideal and it was only used for the validation of the *PCP*, as the wires are not kept at a horizontal position, and the loop of the wire around the pin creates a pre-stress, pre-bending the beam on the opposite side. This effect can be seen on Figure 3.27, where the beam is laying on a flat surface and the wires induce bending.
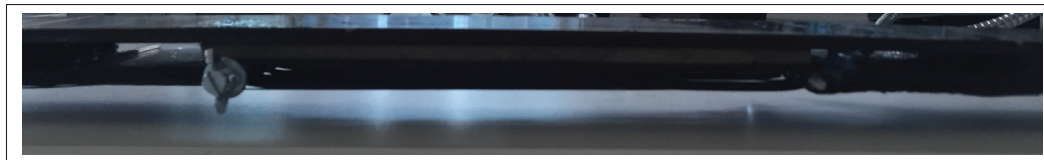
Figure 3.27   Pre-bent beam by SMA wires stress

3.2   Testing

The testing of the *Proof of Concept Prototype (PCP)* was done to validate the analytic and numerical design tools, studied in Chapter 2. Because of the large deformations to which the compliant section was submitted during testing, some nuances need to be taken into consideration.

3.2.1 Setup

The testing of the *PCP* was done on a *Four Point Bending (FPB)* set-up, as seen on Figure 3.28, with a displacement controlled loading. With this method, a Pure Bending-Moment loading can be introduced on the study section, while artificially isolating the shear-loads in the system.
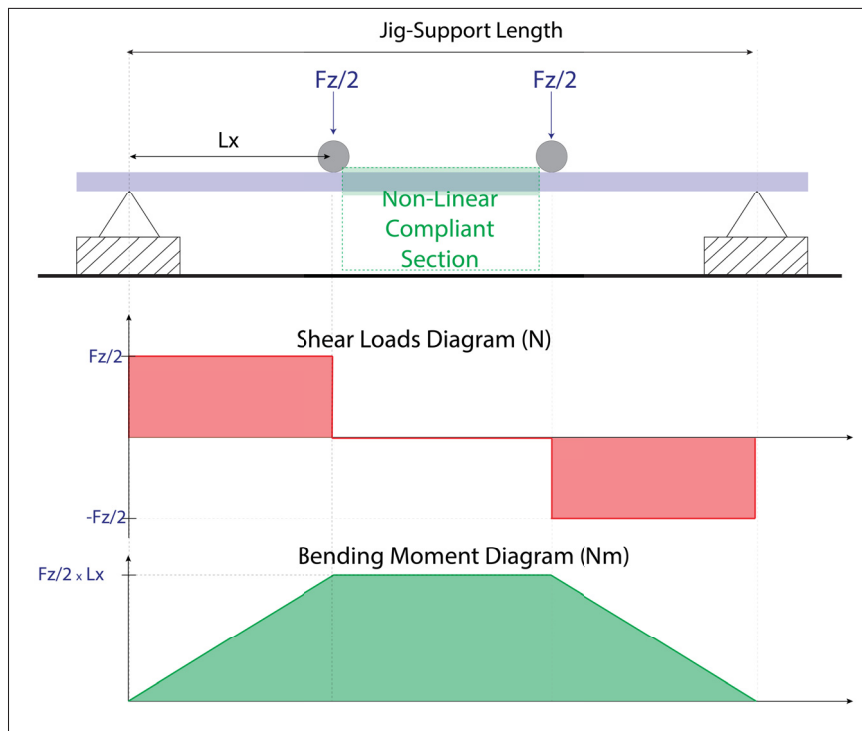
Figure 3.28   Four-Point Bending Setup and loads diagram

The test was performed with a custom *FPB* jig manufactured at the FHNW and able to be used on the IKT tensile test machine.

3.2.2 Testing Procedure

Because only one prototype was available for testing, a progressive schedule was performed to acquire the maximum possible amount of data before the failure of the structure, starting with a 100 *mm* displacement *load-controlled* introduction, and increasing of 50 *mm* at every step. The testing setup on the first 100*mm* step can be seen on Figure 3.29.

To evaluate the non-linear compliant beam capabilities against a small cyclic performances, 5 *loading-unloading* cycles were done at every displacement step.

The ultimate goal of these series of test was to achieve the beginning of the *Detweened Martensitic* transformation slope, where the SMA wire increases its stiffness, after the pseudo constant stress plateau.

The displacement rate of the load introduction was set to 0.25 mm/s for the tests (see Table 3.4). These slow speeds were chosen to give enough time to the *martensitic* transformation to propagate the energy and reduce the material heating effect of the SMA and keep the $stress - strain$ behaviour as constant as possible during the *loading-unloading* phases, as described by Rao (2015). Consequently, this was also a safety measurement, considering the possible failure of a large loaded spring on an open space.

Table 3.4 Testing Schedule

Test Number	Displacement	Speed
T01	100 mm	0.25 mm/s
T02	150 mm	0.25 mm/s
T03	200 mm	0.25 mm/s
T04	250 mm	0.25 mm/s
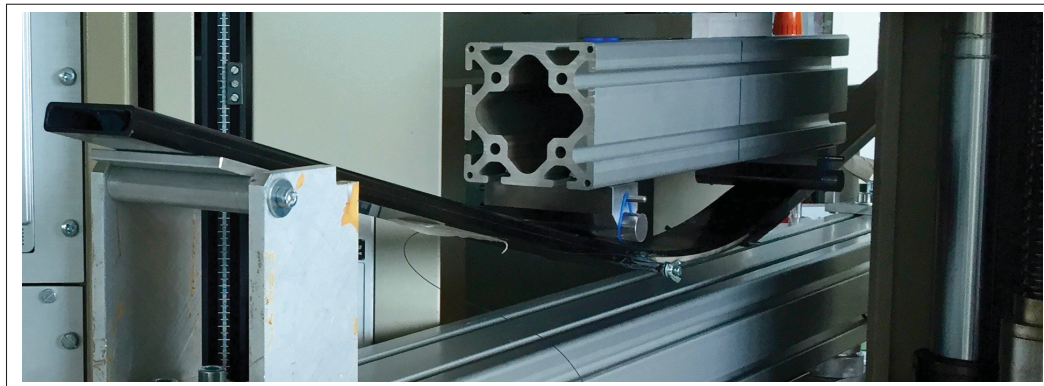
Figure 3.29 Four-Point Bending Test

3.2.3 Data Analysis

3.2.3.1 Experimental Data

The data extracted from the experimental tests are the *Displacement* of the load introduction pins (L_z), as well as the total *Acting Force* (F_z), sum of the two load introduction pins.

To obtain the bending moment applied at the compliant section (M_{Beam}), Equation 3.3 is used, where L_x is the *Lever Length* between the jig support and the closest load introduction pin, and F_z is the acting force.

$$M_{Beam} = L_x \cdot \frac{F_z}{2} \tag{3.3}$$

Equation 3.3 is only true if small beam deflections are analyzed. As seen on Figure 3.30, in the case of the prototype, more parameters need to be taken into count to evaluate the total bending moment calculations.

Because of the beams' large deflection, the force component on the "*x*" axis is not negligible as the displacement evolves, like it is assumed for small deflections. Because of this, the F_z readings on the tensile machine cannot be used as the only introduced load in the system.
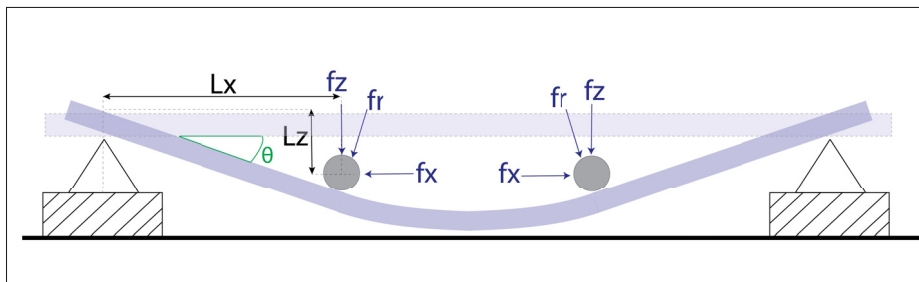
Figure 3.30   Forces and levers diagram on *FPB* Test

To obtain the bending moment, the z and x components of f_r, being f_z and f_x need to be multiplied by the distances on each orthogonal axis, becoming:

$$M_{Beam} = \sum M_x + \sum M_z = f_z\, L_x + f_x\, L_z \tag{3.4}$$

To proceed with the calculations, the value of f_z is simple obtained by dividing the measured *force* (F_z) by two, becoming $\frac{F_z}{2} = f_z$, and for the L_z distance, this is directly obtained from the data-log reading. The L_x dimension is kept constant during the whole procedure, this distance being defined by the installation setup. Finally, to derive the f_x value, the following functions are applied to obtain the angle θ, as well as the force in the x direction.

$$\tan \theta \; = \frac{L_z}{L_x} \Rightarrow \theta \; = \tan^{-1}\left(\frac{L_z}{L_x}\right) \tag{3.5}$$

$$\tan \theta \; = \frac{f_x}{f_z} \Rightarrow f_x = \; f_z \, \tan \theta \tag{3.6}$$

$$M_{Beam} = \; f_z \, L_x \; + \; L_z \, f_z \, \tan \theta \tag{3.7}$$

3.3   Results & Observations

The testing schedule was performed as expected, except for $T04$ from Table 3.4, and the last measured state can be seen on Figure 3.31. While on the 250mm displacement tests, 1mm above the 240mm threshold, a typical composite failure noise was heard and the tests was stopped and brought back to the initial state rapidly.

Figure 3.31   PCP at maximum achieved deflection

To evaluate the accuracy of the models, the *Bending Angle* and the *Bending Moment* were compared graphically. The derived experimental results, the FEM results as well as the SMA Beam Tool results were compared. The raw data comparison can be seen on Figure 3.32.
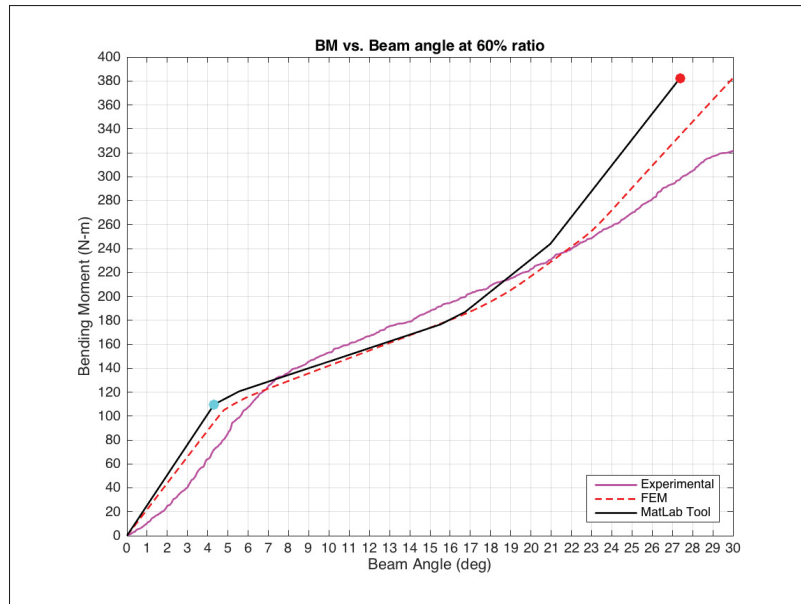
Figure 3.32   Analytic and experimental results comparison

When the results of the SMA Beam Tool, the FEM and the experimental data superposed, some conclusions could be made. Beginning on the first slope, assumed to be straight in the analytic models, the experimental data shows a curved first slope between 0° and 8° of beam angle θ. This behavior was somehow expected, since the *SMA* wires were installed with some slack. The reason of the slack on the wires is a compromise on the geometrical dimensions and position of the pin-loaded strap. This causes a *delay* on the beam response, until the wires were all put under tension.

This slope creating an offset reaction, was visible on all tests (see Table 3.4) and caused a considerable shift on the expected beam behavior, where the *stress-strain* behaviors properties are not as the models predicted. When comparing the slopes of the non-linear behavior between the analytic and experimental data, some equivalences can be found. If a tangent segment is traced on the first slope of the experimental results (see Figure 3.33), the obtained slope angle is

similar on both cases. The same approach can be done with the second slope, when the SMA stiffness is reduced. When looking at the third slope, when the SMA *Detwinned Martensitic* transformation phase is achieved, the results diverge completely. This divergence on the third slope could be caused by the foam core crushing, reducing the inertia of the section, and with it, reducing the *EI* of the beam.
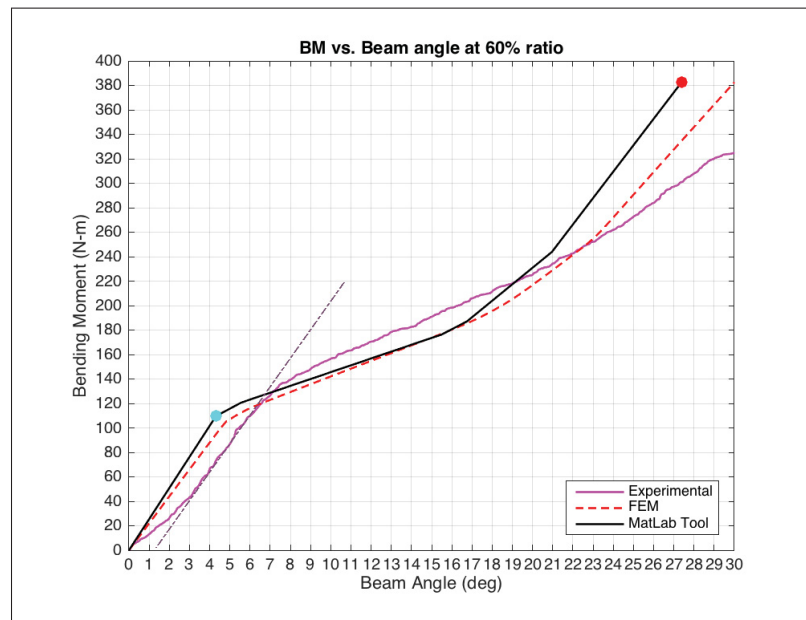
Figure 3.33   Tangent curve on first slope exp. data

If the design targets are observed, the target *triggering* bending moment defined by design is achieved at $115Nm$. The experimental results show a stiffness change at $\approx 125Nm$, with an error of $\approx 8.6\%$. Continuing with reduced stiffness induced by the pseudo-constant stress *plateau* from the *SMA*, also visible in the results.

By design, the beams section stiffness was made to increase at $\approx 17°$ of θ, induced by the *Detwinned Martensitic* phase transformation of the *SMA*. Because of the results shifting, this slope change can be seen at $\approx 20°$ of beam angle. This tendency is visible but evidently weaker on the *experimental* data than the produced by the *FEM* and the *SMA Beam Tool*.

At $\theta = 31°$, (see level indicator on Figure 3.31) the beam structure failed on the *Pin Loaded Strap* laminate bonding and as described previously, the test had to be stopped for safety reasons.

After the visual evaluation of the *PCP* structure, it was found that the pin-loaded strap attachment, hand-laminated over the CFRP beam, started to peel off. This was caused by the local bending at the attachment. Testing could have continued with this initial failure, but no other tests were performed after it, as the acquired results were considered as sufficient, achieving the second SMA slope behavior at the failing point. The debonded *CFRP* laminated was found, as seen on Figure 3.34, showing the last image of the tests with a *close-up* view, as well as the severity of the case, judged as minor after wise.
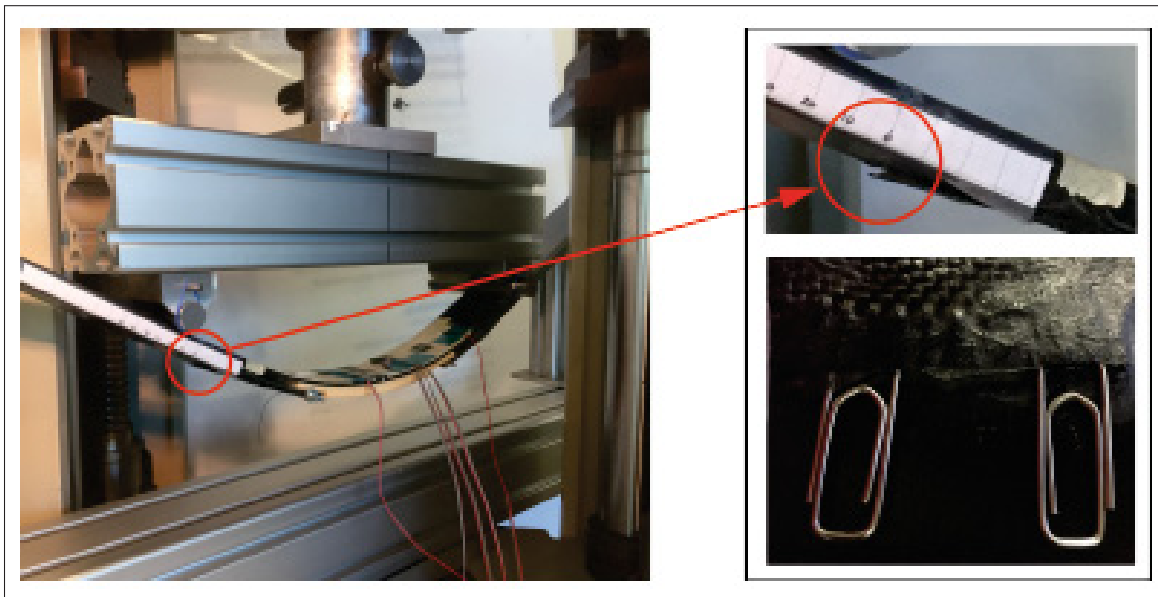
Figure 3.34   Pin-loaded strap fail on *PCP*

3.3.1   Conclusions

The goal of this series of tests was to ultimately validate the envelope of the *PCP* design, as described, this could not be accomplished. On the other hand, the results tendencies and similarities to the simulations give a great prospect for the application.

While the Pin-loaded strap is a simple system for the integration of the wires in a beam with such characteristics, using a smaller SMA wires diameter or even smaller *flat-wires* like the *Euroflex* 0.2*mm*x0.5*mm flat-wire* (see Figure 3.35) mounted on test-piece pin loaded straps.

The use of this kind of SMA would help on reducing the induced bending and the wire slack in the installation. The downside of this method is that for a smaller cross-section wire, a higher number of loops is needed.
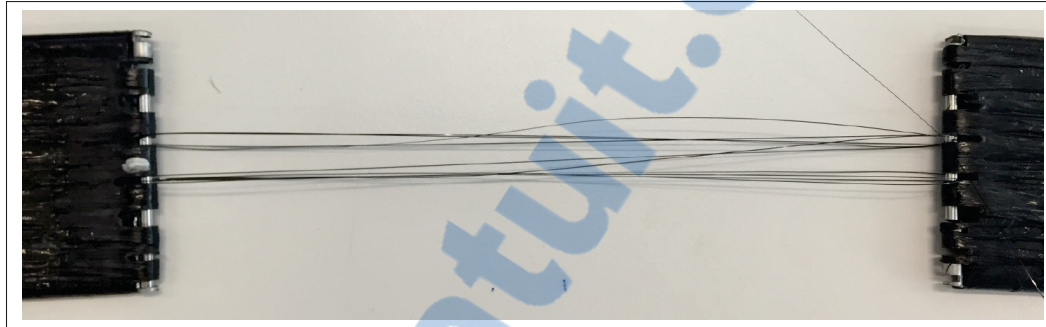
Figure 3.35   Pin-loaded with *Euroflex* 0.2*mmx*0.5*mm flat-wire*

The FEM model and the analytic calculations were not assuming a Foam Core crushing, as the maximum compression material strength was respected (see Figure 3.36). The simulation assumed a flat section to represent the strip of SMA wires.
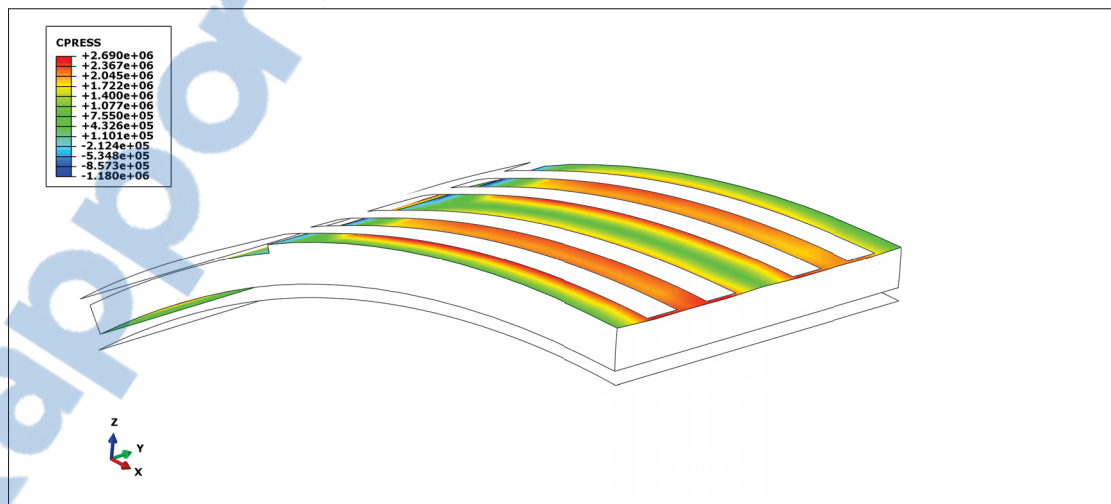
Figure 3.36   FEM model of realistic SMA wire configuration

This evaluation was under estimated, as it is evident on the experimental results (see Figure 3.37) where a permanently deformed groove on every wire strip is visible.

Figure 3.37   Foam Core damage from SMA wires

CHAPTER 4

HYDROFOIL PRELIMINARY DESIGN PROCESS (PD)

This chapter describes the complete process that led to the preliminary design of a passive-morphing hydrofoil for an *AClass* catamaran. The proposed design is a compliant structure able to *morph* from a *J/Z* to an *L/V* hydrofoil geometry.

4.1 Hydrofoil Definition and Load Case

The baseline design used for the study is the *EH1* hydrofoil, as seen on Figure 2.4. This *J/Z* design is the best compromise for a class-legal *AClass* catamaran, allowing a *hull skimming* when sailing upwind and unstable foiling while on a reach or downwind tack. Two load cases were used for the analysis, at boat speeds of 12*kt* and 24*kt*. These two speeds define the load cases for the *Triggering* and *Maximum* foil efforts, represented as bending moments, to which the hydrofoil will be submitted. The loads derivation was done by *F. Schadt* (Schadt, 2016) with a three foil support configuration as this non-linear compliant hydrofoil concept proposes, to evolve the hydrofoil geometry from a *J/Z* to an *L/V* hydrofoil, as shown on Figure 4.1.
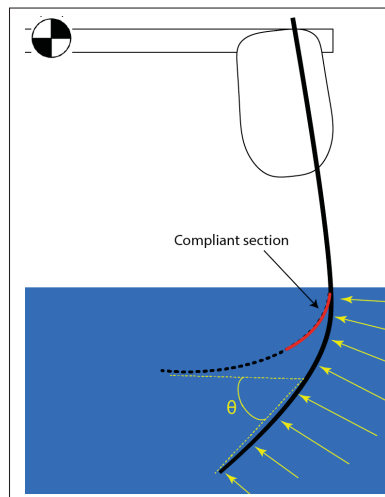
Figure 4.1   Compliance of
a *J/Z* to an *L/V* hydrofoil

4.2   Calculation Process

The calculation process starts with the *Non-Linear Beam EI Tool* described on Chapter 2, defining the overall geometry of the structural beam and the number of discrete elements that will be used for the analysis. The values used for this case can be seen on Table 4.1.

Table 4.1   Beam Definition

Beam Definition		
Beam Length	1300	*mm.*
Elements	13	$(100mm./elem)$
Height	15	*mm.*
Width	60	*mm.*

To approximate the *EH1* hydrofoil geometry, the angle between the elements in the relative and absolute reference system was defined. The specific values can be seen on the *GeoAng* and *GeoAngAbs* columns from the beam matrix (see Appendix IV) .

To determine the element stiffness (EI) (see section 2.4.1), the maximum strain (ε) targets for the beam elements were defined as 0.3% on the first 6 elements, then 0.2% from elements 7 to 11 and 0.1% on the last two elements, with the intention of keeping the foil tip as a stiff member and allowing a small compliance from the root to the elbow of the foil. These values come from the experience on previous iterations of the full hydrofoil preliminary design.

The allowed tolerance was defined at $\pm 0.075\%$ for an initial evaluation of the model. In further steps, this value should be reduced for a higher accuracy (see Appendix IV) . With the initial data defined in the scripts, the 12*kt* load case matrix was imported into the *MatLab* script. This matrix is defined on the orthogonal reference system. A data treatment was done to obtain the equivalent vector loads, normal to the beam elements. The model was then validated in the *Sim Mechanics GUI*, as seen on Figure 4.2. This evaluation will determine the *Triggering* bending moment and total lift obtained with a deformed hydrofoil.

The convergence of the model calculations was achieved in under 7*min* on an *Intel i7 with 8Gb of Ram* computer, with results assuring a vertical lift on the *z* axis of $\approx 850N$, meaning that in
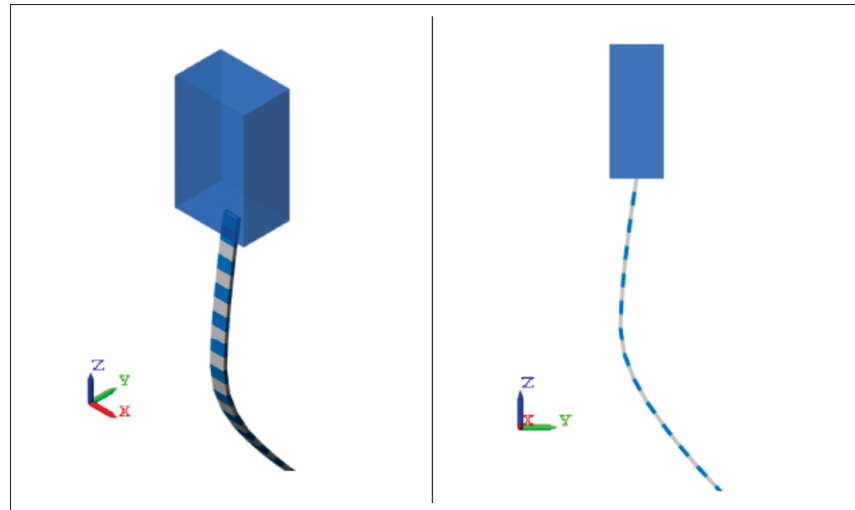
Figure 4.2   ISO and Front view of Hydrofoil *Sim Mechanics GUI*

that situation the boat would not be able to *foil*, as the total weight assumed on the load case is 1600*N*, where 850*N* are assigned to the skipper and 750*N* to the boat weight. From this study, the triggering *Bending Moment* at the 9th element, chosen to be the compliant section was found to be 124*Nm*.

The Isometric and front views of the *foil* under load can be seen on Figure 4.3.
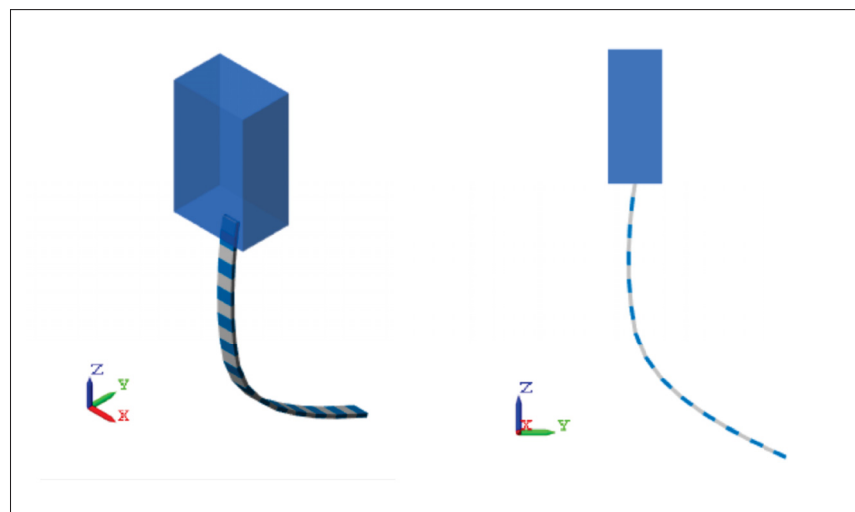
Figure 4.3   Hydrofoil at *Triggering* load case and geom.

As a second step, the load case evaluating the $24kt$ boat speed was introduced in the model. Because this load case assumes a compliant hydrofoil, as well as a fully *foiling* boat, the target strains at the elements 9th and 10th were increased to $\varepsilon = 2\%$ to represent what it can be achieved with SMA on that region. The final results, compared with the initial and *Triggering* case can be seen on Figure 4.4.
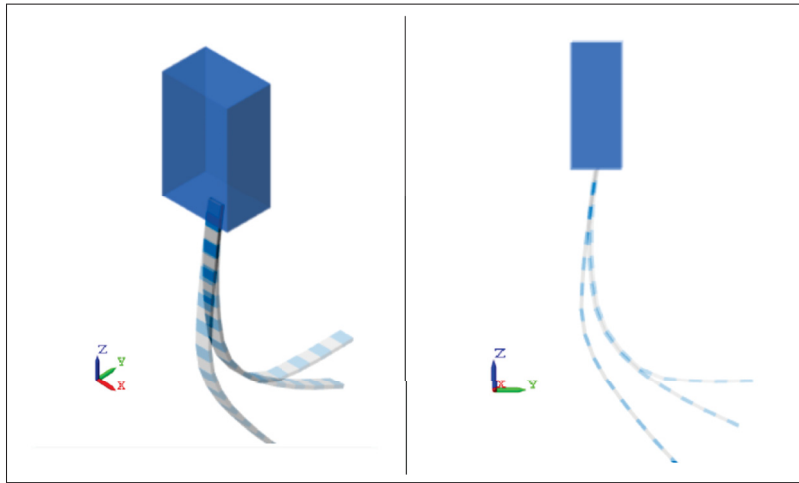
Figure 4.4   Hydrofoil superposed compliance comparison
Unloaded, Triggering & Maximum Compliance

The calculations concluded in under $15min$, where the lift force on the z axis was calculated as $1680N$. The *Bending Moment* at the 9th element was found to be $384Nm$, and a total bending angle of $\theta = 37.5°$ was reached with the 9th and 10th elements rotation. The summary of the results can be seen on Table 4.2.

Table 4.2   Non-Linear Beam EI Tool main results

Triggering BM	124	*Nm*
Maximum BM	384	*Nm*
Compliant Length	200	*mm*
θ	37.5°	

Along with both load case calculations, each study helped to determine the necessary structural stiffness distribution *EI* to respect the imposed strains. The study at maximum load was used for the evaluation of the composite structure with the *Beam CLT Tool*. As described in Chapter 2, this script provides a layup thickness for the *I-Beam web* and *flanges* for every element analyzed on the *Non-Linear Beam EI Tool* calculations.

For this case, the carbon fiber composite used in Chapter 3 for the prototype manufacturing was used, with a $[\pm 30\ 0\ \pm 30\ 0]_s$ laminate, obtaining the layup thickness as seen on Table 4.3. This laminate respects the $FI\ = < 0.7$ criteria.

Table 4.3   Flanges and web thickness on CFRP I-Beam

CFRP I-Beam													
Elem Number	1	2	3	4	5	6	7	8	9	10	11	12	13
Web(*mm*)	6.2	6.1	5.9	5.7	5.4	4.4	4.0	3.2	–	–	1.4	0.6	0.5
Flanges(*mm*)	3.2	3.1	3.0	2.9	2.7	2.4	2.1	1.6	–	–	0.7	0.3	0.2

As seen on Table 4.3, the laminate thickness on elements 9 and 10 are not defined. Even though the tool is able to calculate this compliant section, the results cannot be taken in account, as the definition is based on the maximum compliance of the beam, practically impossible to achieve with this kind of structure and material. Because of this, the next and final step consists in calculating the compliant section with the *SMA Beam Tool*, following the procedure described in Chapter 2.

Considering the previously calculated cases and the main parameters for the compliant section on Table 4.2, iterative calculations were done using the *SMA Beam Tool*, aiming to obtain the required results, with a *CFRP* safety coefficient below the 0.71 arbitrary limit mentionned in Chapter 3.

By using the same *CFRP* material and *SMA* as for the *PCP*, the compliant section could be defined in less than 10*min* and 20 iterations, yielding a structure with 4% of beam height for the *SMA*, equivalent to a 0.6*mm* thickness plate and having a $[\pm 30/0_2/\pm 30/0_2/\pm 30/0_2]_s$ laminate, as seen on Figure 4.5 from the *tool GUI*.
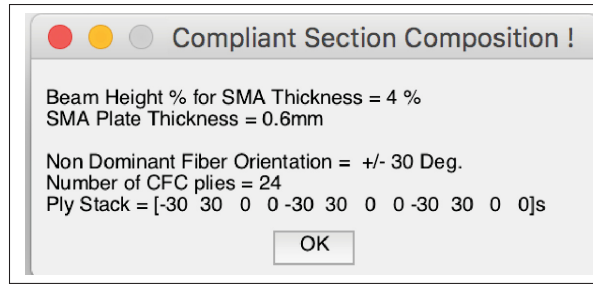
Figure 4.5   Compliant Section definition

With these section properties, the *Bending Moment* and *Tsai-Hill* failure index evolution against the $Ratio_{sma}$ were obtained, as seen on Figure 4.6.
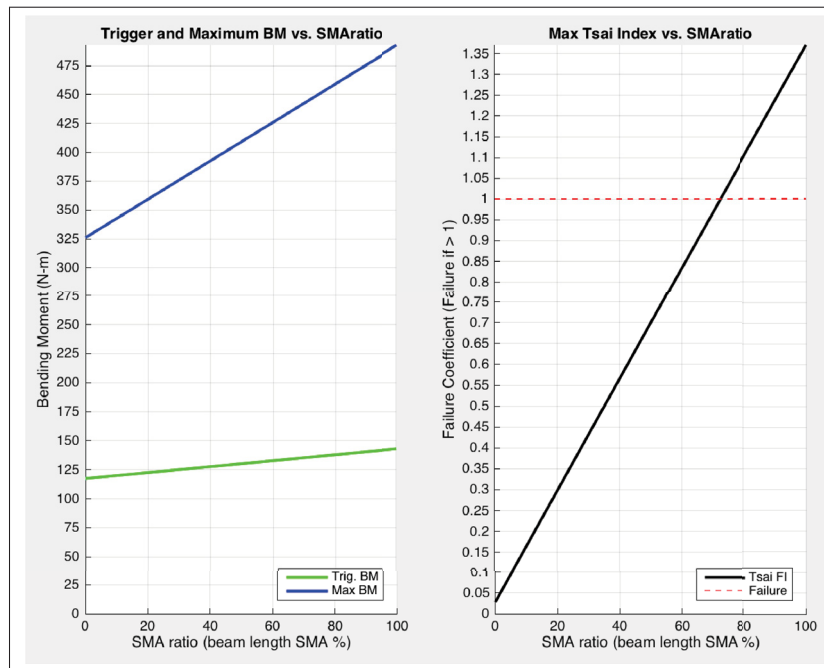
Figure 4.6   Trigger/Max. BM and Failure Criteria vs. $Ratio_{sma}$

The final design choice to be made to comply with the design parameters is the $Ratio_{sma}$, that for this case it was defined at 40%, obtaining the *Triggering* and *Maximum Bending moments*, as well as the failure criteria. The results from the *Tool GUI* can be seen on Figure 4.7.
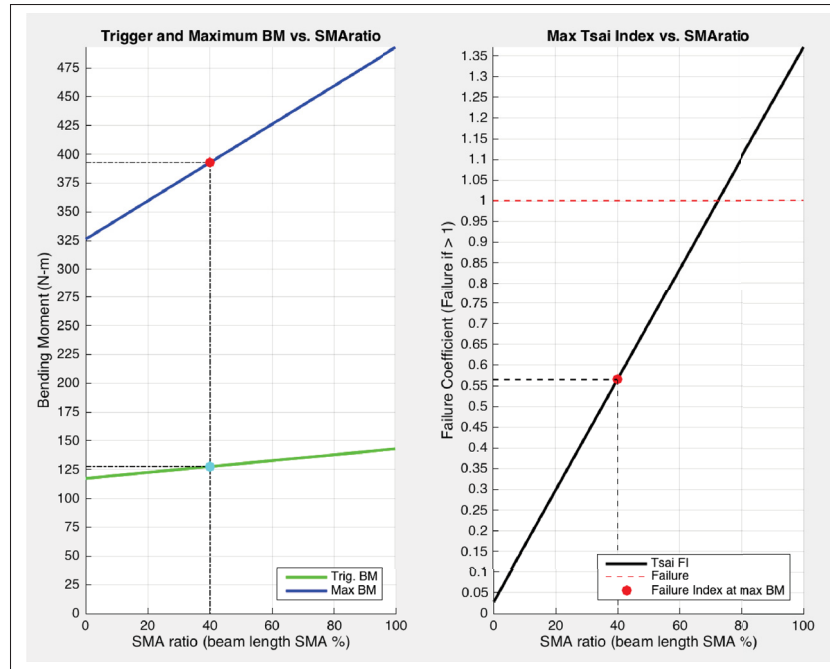
Figure 4.7   *Ratio$_{sma}$* choice and Plotting

With all design parameters chosen, the last validation is the bending angle θ at which the foil with bend at maximum loading. The 37.5° target deflection angle obtained with the *Non-Linear Beam EI tool*, was approximated with the iteration on the *SMA Beam Tool*. As seen on Figure 4.8, the angle at the maximum *Bending Moment* is $\approx 17.5°$, resulting in a $\theta = 35°$ (2 *x* 17.5°), being this value 2.5° below the *target*.
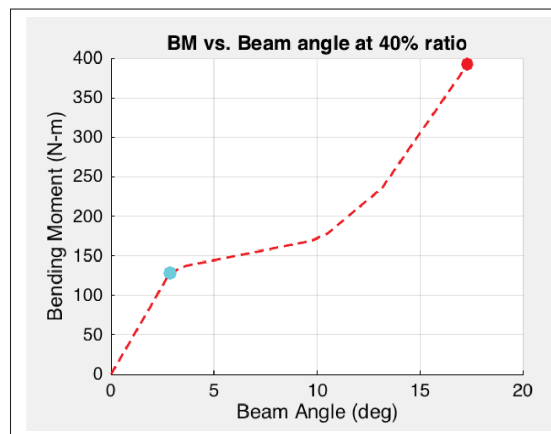
Figure 4.8   Beam Angle $\theta/2$ at Trigger
and Maximum Bending Moments

The design process shown on this chapter represents a simplified approach for the design of a complete Passive-Selective Non-Linear compliant hydrofoil for an AClass catamaran. It proves that the methodology is efficient for the preliminary design of the three main parts of the hydrofoil, without the need of FEM until a more refined design stage is needed.

CONCLUSION AND RECOMMENDATIONS

The purpose of this project, was to evaluate the design feasibility of a passive non-linear compliant hydrofoil structure and its potential application for an AClass catamaran.

Both goals were achieved by developing different customized tools that made the design process more efficient than using regular FEA iterations for preliminary design calculations.

As proven in Chapter 3, the proposed passive compliant structure is able to provide large non-linear deformations with a relatively simple SMA embedded system.

This non-linear compliant structure concept could be used in other fields, such as aerospace or wind energy, where passive actuation to change the airfoil profile with respect to loading could be improve efficiency. Nonetheless, for a practical application on a real catamaran, many issues related to the structure behavior and variables need to be addressed.

For a real case implementation, at least five main considerations should be taken into count. First, the evaluation of the torsional stiffness and 3D load cases would be needed for the compliant section. The conducted analysis of the PCP only considers 1-axis pure bending and no shear loads, being an unrealistic situation. The CFRP laminate used for the prototype has a high axial stiffness which might not prove to be adequate to respect torsional design requirements.

The second considerations is the influence of the temperature on the behavior of the SMA and its impact on the system.The SMA being a highly thermo dependent material, and the main responsible for the non-linear behaviour of the structure, the calculations and the application environment should be defined to have a precise range of actuation.

Another aspect that should be considered for a real application is the structural fatigue. While CFRP composites could achieve high-cycle fatigue, SMA are not as long lasting. Because of this, a deeper evaluation of the material to be used should be considered and defined to provide

a long lasting hydrofoil or a way to replace the shorter lifespan material.

The fourth consideration concerns the integration of the SMA into the system, which is a great challenge in the project. For simplicity, SMA wires were used for this work but this method induced some errors in the application and testing because the wire was manually installed. The inconsistent tension of the 138 wire lengths created a variation in the structural behaviour of the compliant beam. A potential solution to this problem would be the use of an SMA plate directly installed into the CFRP. This solution would create a more practical and stable system.

Finally, developing a solution to maintain an acceptable airfoil shape around the compliant section needs to be considered for a real application case. This part should allow great deformations to follow the internal non-linear structure without modifying the hydrodynamic performance of the hydrofoil.

APPENDIX I

MATERIALS DATA SHEETS

SPECIAL METALS

CERTIFICATE OF TEST

NEW HARTFORD, NY 13413-9576
PHONE: (315) 798-2029
FAX: (315) 798-6860

```
                                CERTIFICATION DATE      :  12/05/01

Ecole de Technologie Superieure   CUSTOMER ORDER NUMBER   : 40823
1125, rue Williams Quest          SMC ORDER NUMBER        : ETS-13008
Montreal, Canada                  ALLOY                   : NITINOL
H3C 1K3                           SIZE                    : 0.020"
                                  HEAT NUMBER             :C7-7455-4-16A
                                  WEIGHT/LENGTH           : 1#/1129 FT

CERTIFICATION:                                              344m

UDIMET® NITINOL WIRE,  .5 MM (0.020" DIA.) AS DRAWN,
BLACK OXIDE SURFACE, 40% COLD WORK.

Af (FULLY ANNEALED) = +4 DEG. C

     CHEMICAL ANALYSES:

          Element                      Wt %
          Nickel                       55.91
          Titanium                     44.06
          Oxygen                        0.05 Maximum
          Carbon                        0.05 Maximum
          Mn, Si, Cr, Co, Mo, W, V     <0.01
          Nb, Al, Zr, P, Cu, Ta, Hf    <0.01
          Ag, Pb, Bi, Ca, Mg, Sn, Cd   <0.01
          Zn, Sb, Sr, Na, As, Be, Ba   <0.01
          Fe                           <0.05
          B                            <0.001


     THIS IS TO CERTIFY THAT THE ABOVE VALUES ARE TRUE AND ACCURATE
              TO THE BEST OF MY KNOWLEDGE AND BELIEF.



                                    _____   12 5 01
                                    SUBHASH C. GUPTA
                                    AUTHORIZED SIGNATURE      DATE

     PAGE  1  OF  1  -  END OF CERTIFICATE
```

Figure-A I-1   UDIMET® NiTiNOL SMA wire

MITSUBISHI RAYON
CARBON FIBER & COMPOSITES

GRAFIL 34-700

Grafil 34-700 carbon fiber is a continuous, high strength, PAN based fiber. It is available in 12K and 24K filament count tows. They can be supplied in either round tow or flat tow formats. The flat tow (designated by 'WD') is the ideal fiber to use in applications where spreading is required, e.g., tape production. The round tow is used in applications where spreading is not necessarily required, e.g., braiding and weaving.

Typical Fiber Properties

Tow Tensile	Strength	700 4830	ksi MPa	SRM 16
	Modulus	34 234	msi GPa	
Typical Density		0.065 1.80	lb.in^3 g/cm^3	SRM 15
Typical Yield	12K	620 800	yds/lb mg/m	SRM 13
	24K	310 1600	yds/lb mg/m	SRM 13

Typical Mechanical Properties

Tensile Properties	0º	Strength	373 2572	ksi MPa	ASTM D3039 / 0º8ply
		Modulus	19.9 137	msi GPa	ASTM D3039 / 0º8ply
	90º	Strength	11.17 81	ksi MPa	ASTM D3039 / 0º16ply
		Modulus	1.34 9.2	msi GPa	ASTM D3039 / 0º16ply
Compressive Properties	0º	Strength	198 1365	ksi MPa	ASTM D3410 / 0º16ply
		Modulus	18.5 127	msi GPa	ASTM D3410 / 0º16ply
	90º	Strength	28.5 196	ksi MPa	ASTM D3410 / 0º20ply
		Modulus	1.49 10.2	msi GPa	ASTM D3410 / 0º20ply
Flexural Properties	0º	Strength	253 1745	ksi MPa	ASTM D790 / 0º16ply, L/D=32, Vf=61%
		Modulus	19.1 132	msi GPa	ASTM D790 / 0º16ply, L/D=32, Vf=61%
	90º	Strength	14.9 102	ksi MPa	ASTM D790 / 0º16ply, L/D=16, Vf=61%
		Modulus	1.28 8.8	msi GPa	ASTM D790 / 0º16ply, L/D=16, Vf=61%
ILSS	Strength		14.1 97	ksi GPa	ASTM D2344 / 0º16ply, L/D=4, Vf=59%

- 250F Epoxy Prepregs
- Resin: Mitsubishi Rayon #340 resin system
- Tensile and compressive properties are normalized to 60% fiber volume

Important: The technical information contained herein is not to be construed as warranties and no patent liability can be assumed. This information can be used for material selection purposes only.

Figure-A I-2   Grafil 34-700 carbon fiber

MTM® 49-3

MTM49-3 is an 80 to 160°C (176 to 320°F) curing, toughened epoxy prepreg resin system developed specifically for the manufacture of components.

MTM49-3 prepregs exhibit excellent ambient and hot mechanical performance combined with good impact resistance after only moderate cure cycles making them ideal for use in the motorsport industry.

Features

- Autoclave and press curable
- 60 days out life at 21°C (70°F)
- 12 months storage at -18°C (0°F)
- Versatile cure temperatures

- 190°C Tg
- Bonds directly to Nomex core in bodywork type applications

Product variants

- MTM49-3:   High Tg and moderate toughness
- MTM49-3B: Black pigmented variant of MTM49-3
- MTM49-3BB: Black pigmented variant of MTM49-3 (higher pigment loading)
- MTM49-3BD: Black dyed variant of MTM49-3

Related documents

- De-bulking guidelines (TDS1036)
- Autoclave processing – lay-up and bagging guidelines (TDS1037)

Related products

- MTA240 adhesive film (PDS1166)
- MTF246 surface improvement film (PDS1240)

Cure cycle

Autoclave cure

Vacuum bag pressure	Minimum of 980mbar (29"Hg)*
Autoclave pressure	6.2 bar (90 psi)†
Ramp rate	1 to 3°C (1.8 to 5.4°F)/minute
Recommended cure cycle	90 minutes at 135°C +5°C/-0°C (275°F, +9°F/-0°F)**
Cool down	Maximum of 3°C (5.4°F)/minute to 60°C (140°F)

*This is the ideal vacuum level, however, it is recognised that it is not always possible to attain. If in doubt, please contact our technical support staff for advice.

†If producing sandwich panels, apply the maximum pressure allowable for the honeycomb type.

**This is an industry standard cure cycle, however it is possible to cure at 135°C in a shorter time. Consult our technical support staff for further information.

Figure-A I-3   MTM49 Pre-Preg Resin

MECHANICAL PERFORMANCE

Type	Test Method	Units	M60		M80		M100		M130		M200	
Short Edge Marking	-	-	Yellow	Green	Yellow	Blue	Yellow	Black	Yellow	Pale Brown	Yellow	Brown
Nominal Sheet Size	-	mm	1285 x 2605		1220 x 2440		1130 x 2275		1015 x 2045		915 x 1830	
		inches	50.5 x 102.5		48 x 96		44.5 x 89.5		40 x 80.5		36 x 72	
Nominal Density		kg/m³	65		85		107.5		140		200	
		lb/ft³	4.1		5.3		6.7		8.7		12.5	
Density Range		kg/m³	61-69		81-89		100-115		130-150		185-215	
		lb/ft³	3.8-4.3		5.1-5.6		6.2-7.2		8.1-9.4		11.5-13.4	
Compressive Strength	ASTM D1621	MPa	0.55		1.02		1.55		2.31		4.40	
		psi	80		148		225		336		638	
Compressive Modulus	ASTM D1621 – 1973	MPa	45		71		107		170		317	
		psi	6480		10340		15570		24670		45977	
	ASTM D1621 - 2004	MPa	31		52		76		111		210	
		psi	4530		7610		11080		16100		30458	
Shear Strength	ASTM C273	MPa	0.68		1.09		1.45		1.98		2.95	
		psi	98		158		211		287		428	
Shear Modulus	ASTM C273	MPa	20		29		41		59		98	
		psi	2900		4240		5920		8600		14214	
Shear Elongation at break	ASTM C273	%	53%		58%		52%		43%		20%	
Tensile strength	ASTM D1623	MPa	0.81		1.62		2.11		2.85		4.29	
		psi	118		234		306		414		622	
Tensile modulus	ASTM D1623	MPa	44		72		109		176		334	
		psi	6440		10420		15880		25510		48443	
Thermal Conductivity	ASTM C518	W/mK	0.03		0.04		0.04		0.04		0.04	
HDT	DIN 53424	°C	110		110		110		110		110	
		°F	230		230		230		230		230	

Figure-A I-4   Gurit M Foam Core material properties

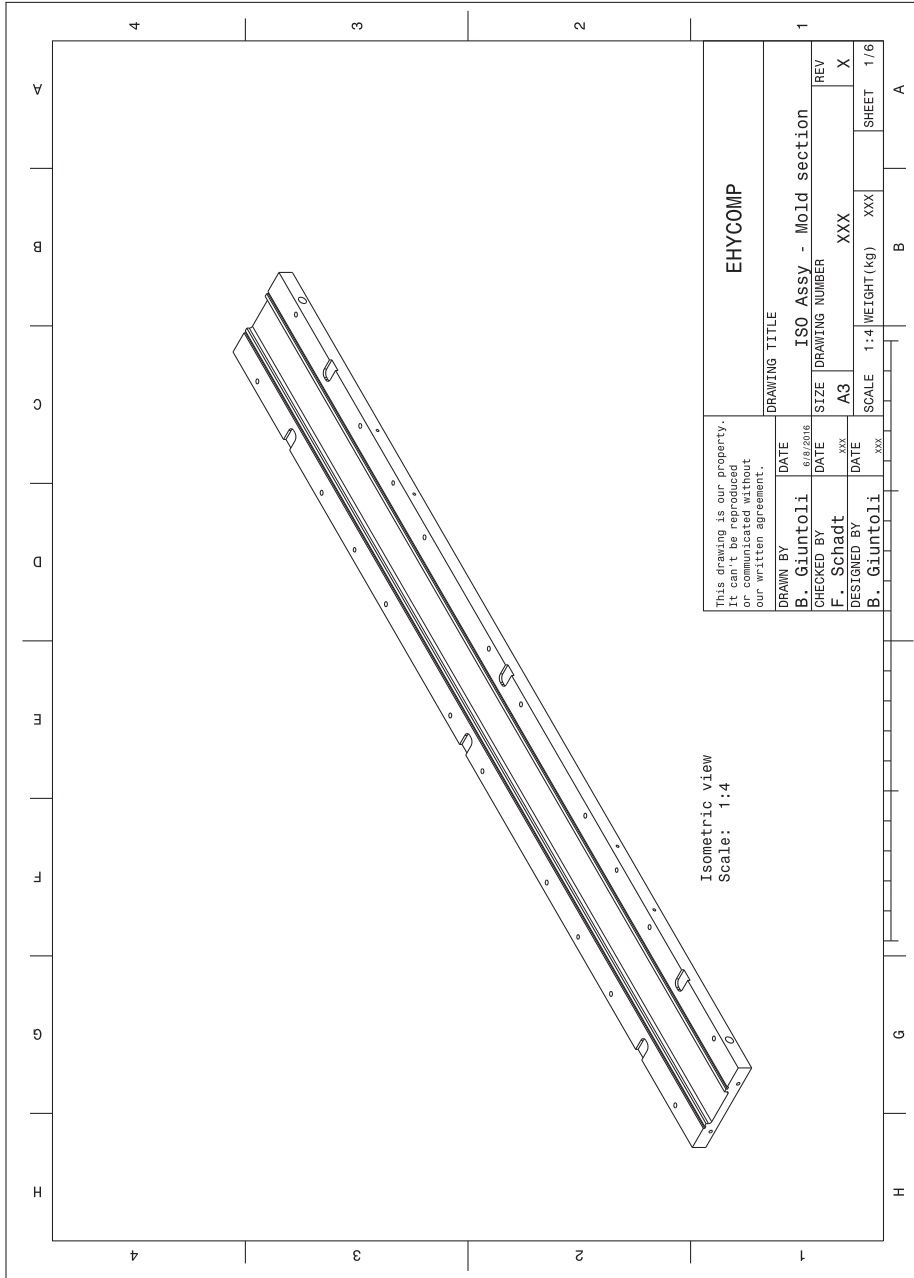# APPENDIX II

MOLD DRAWINGS FOR CAM
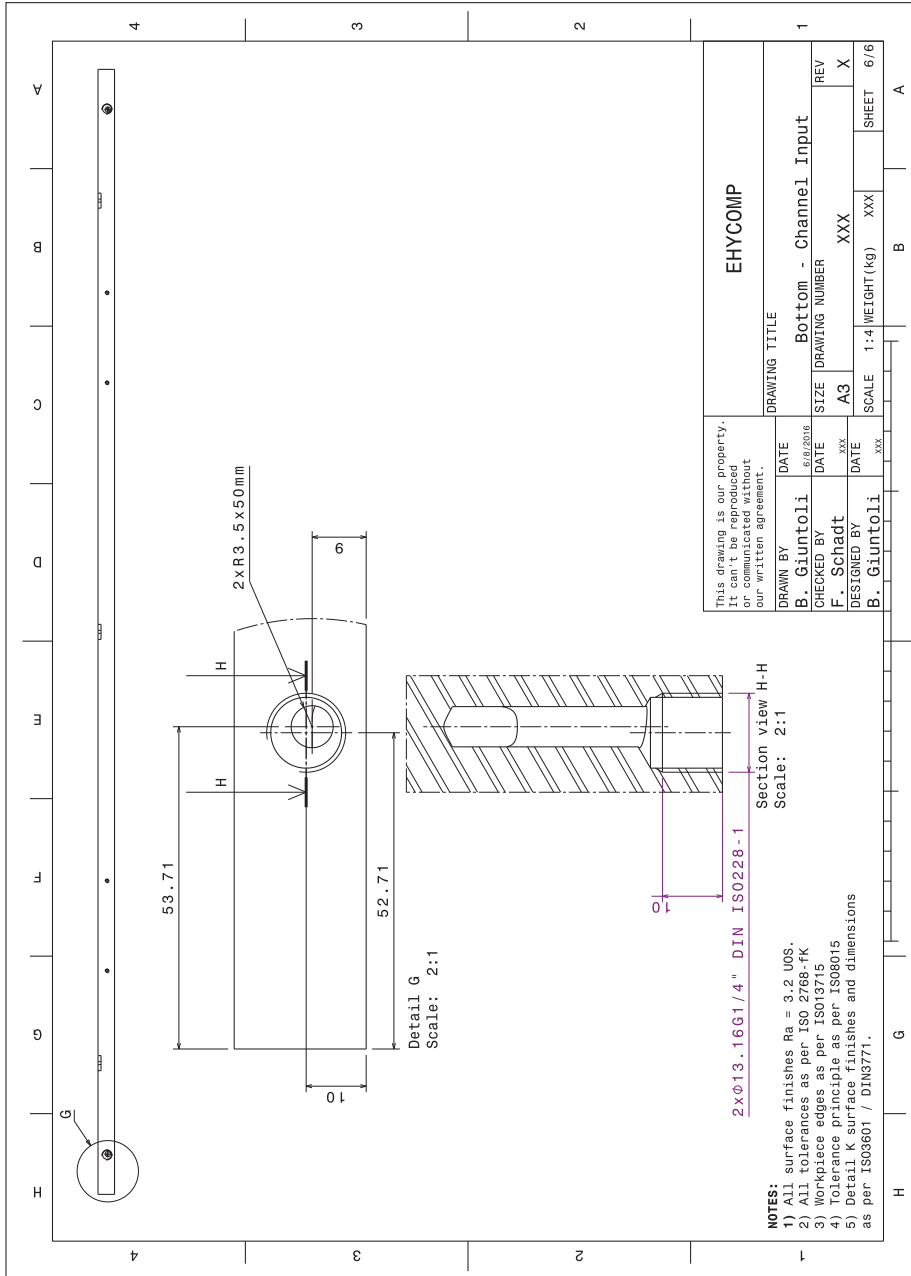

Figure-A II-1   Bottom Side ISO view

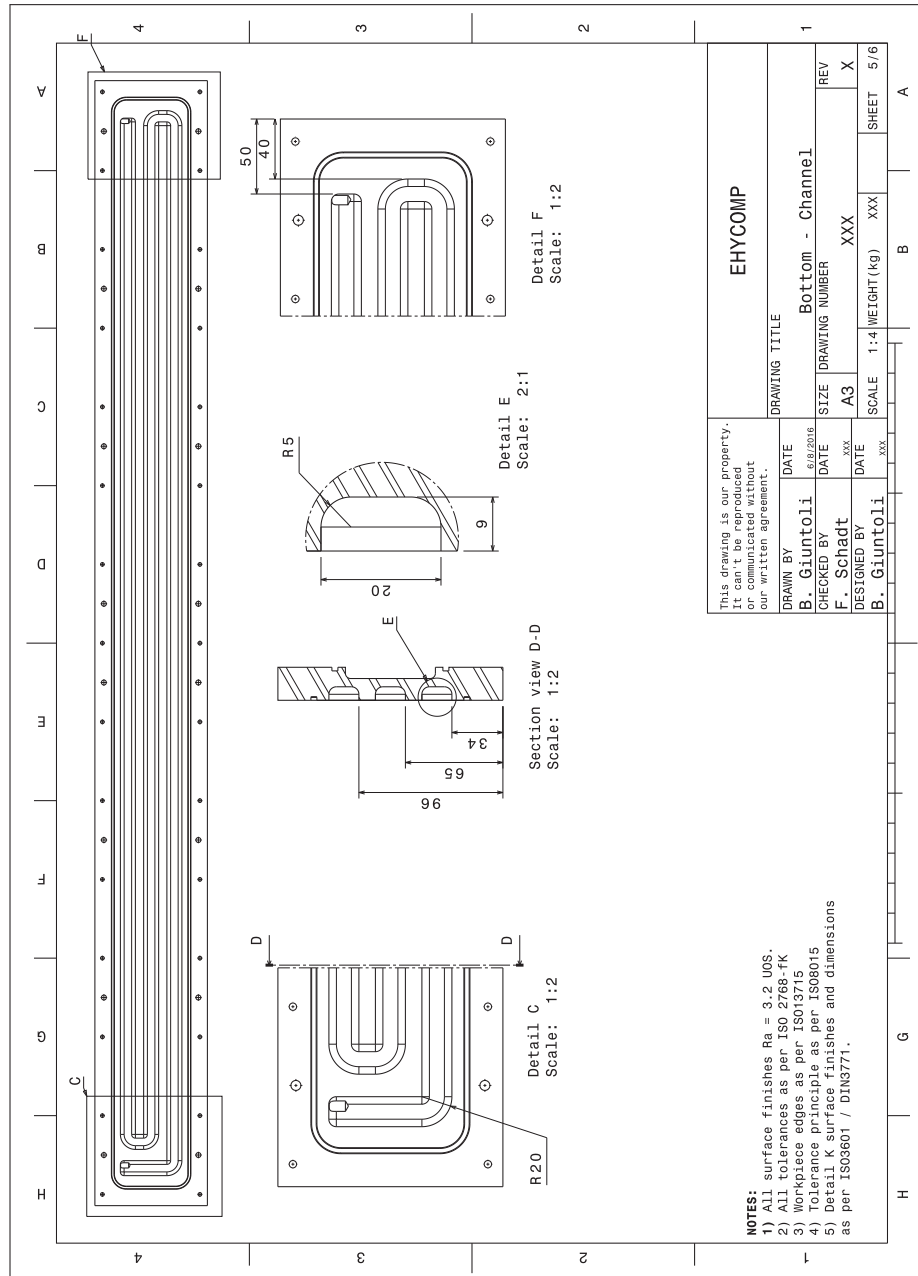Figure-A II-2 Bottom Side heating channel input

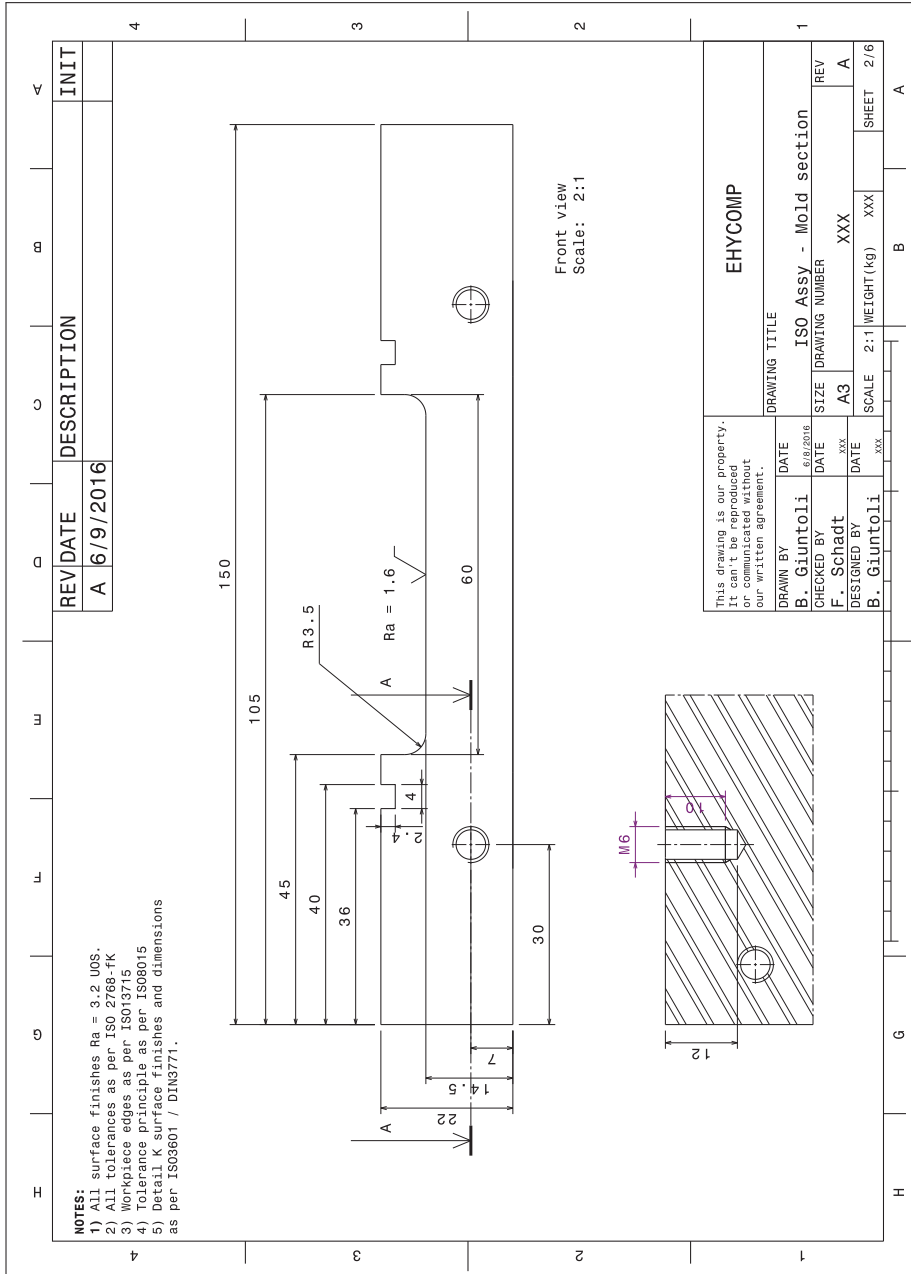Figure-A II-3　Bottom Side heating channel

120

Figure-A II-4   Bottom Side front view

121
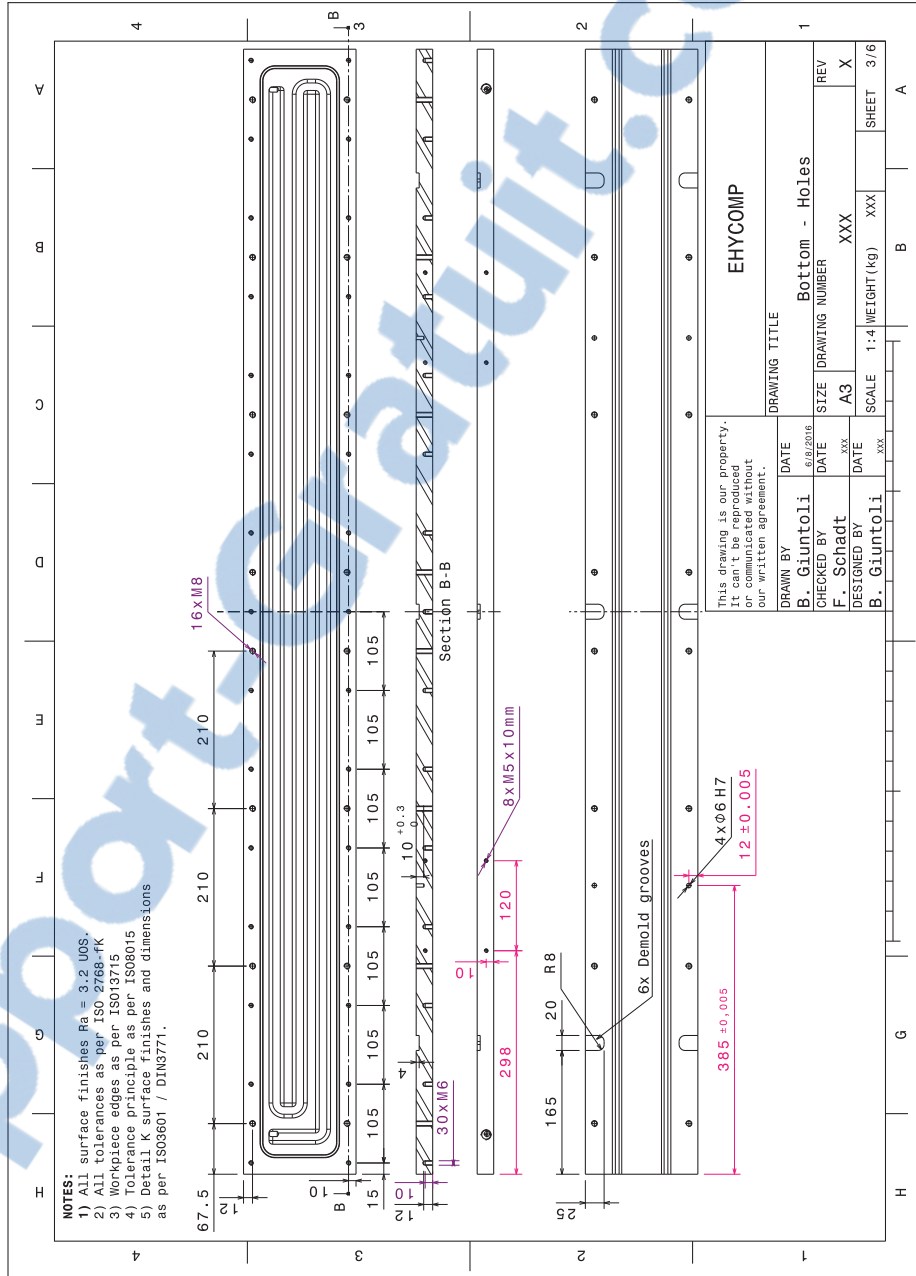
Figure-A II-5   Bottom Side channel closure plate holes

122
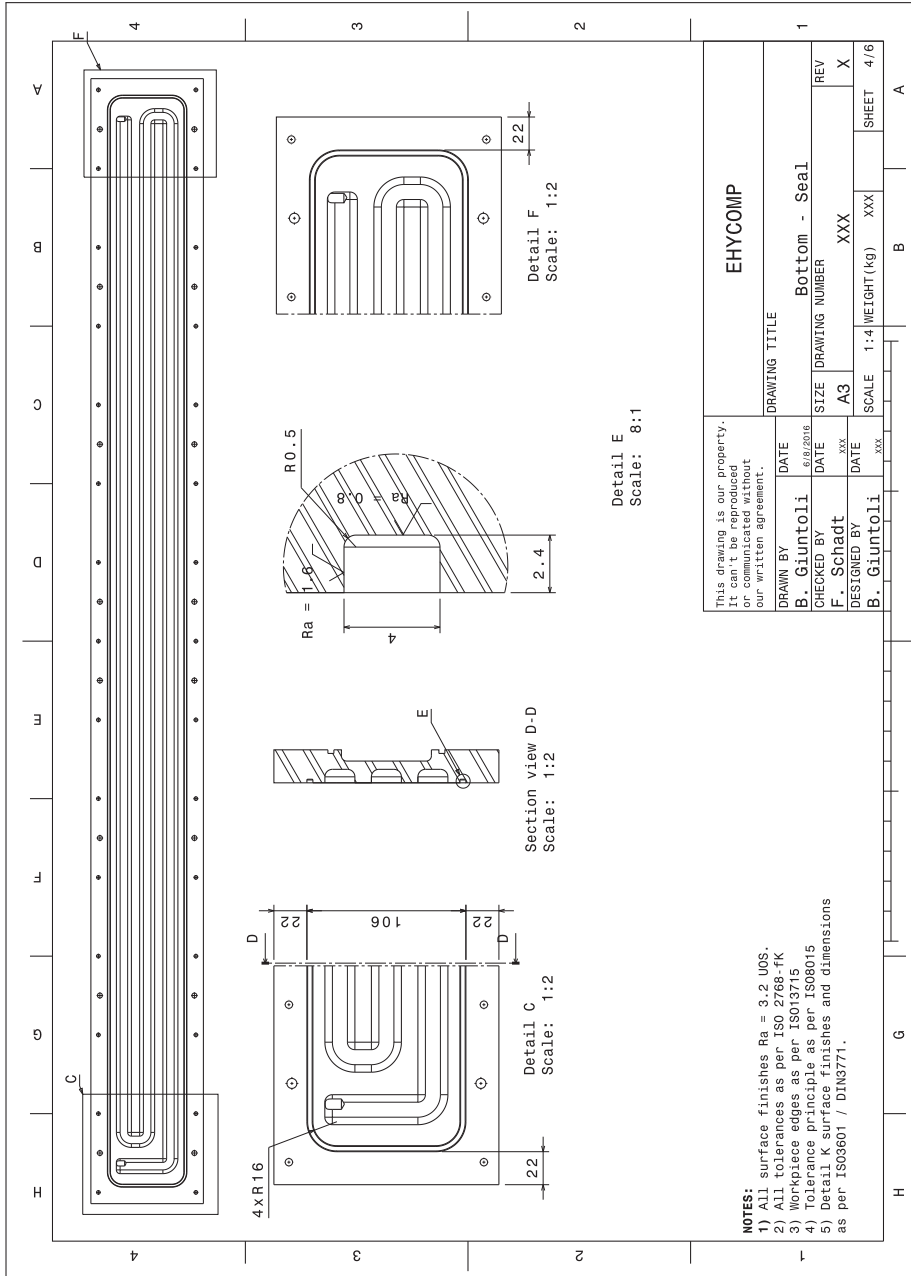
Figure-A II-6   Bottom Side channel sealing groove

Figure-A II-7   Top Side ISO view

124
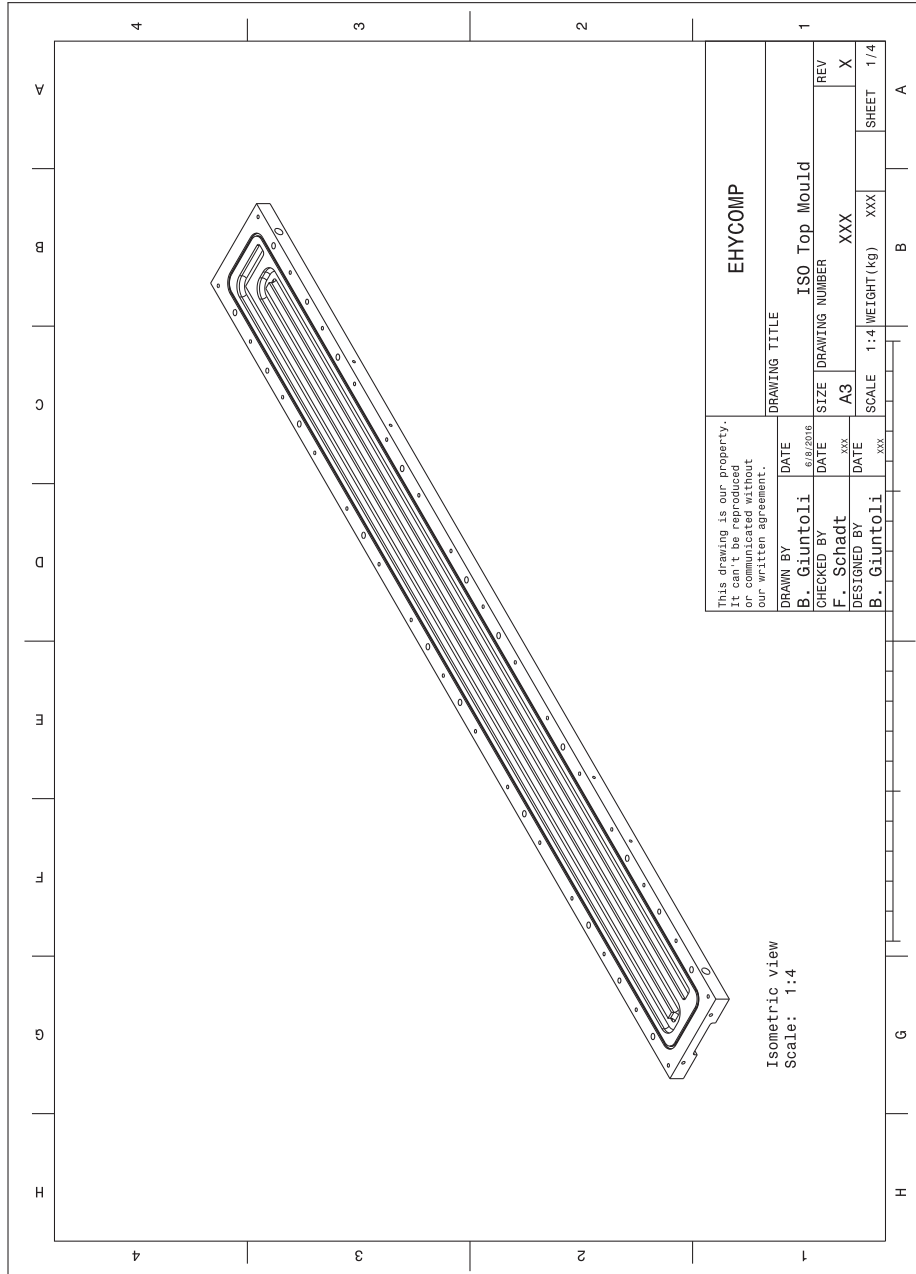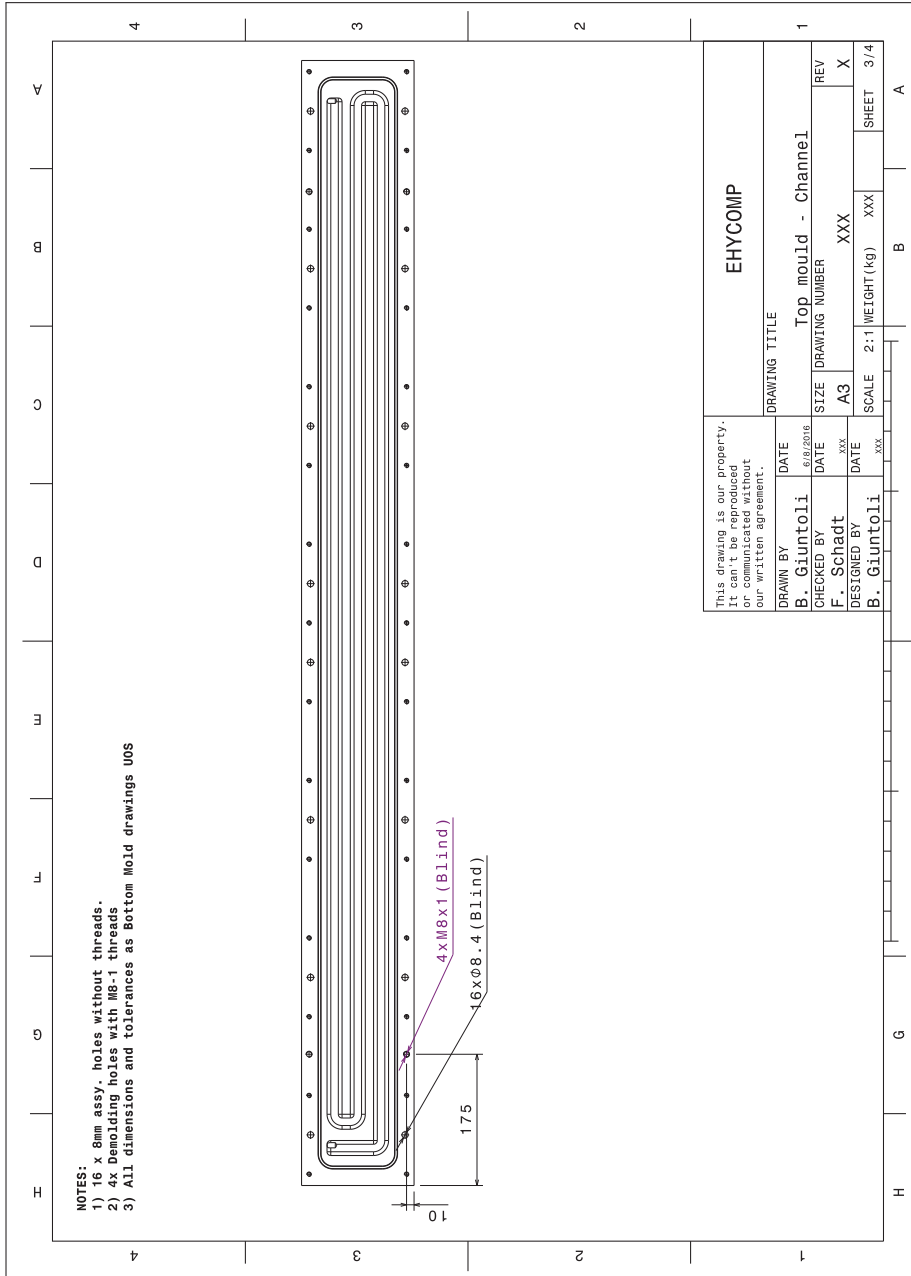

Figure-A II-8   Top Side channel closure plate holes
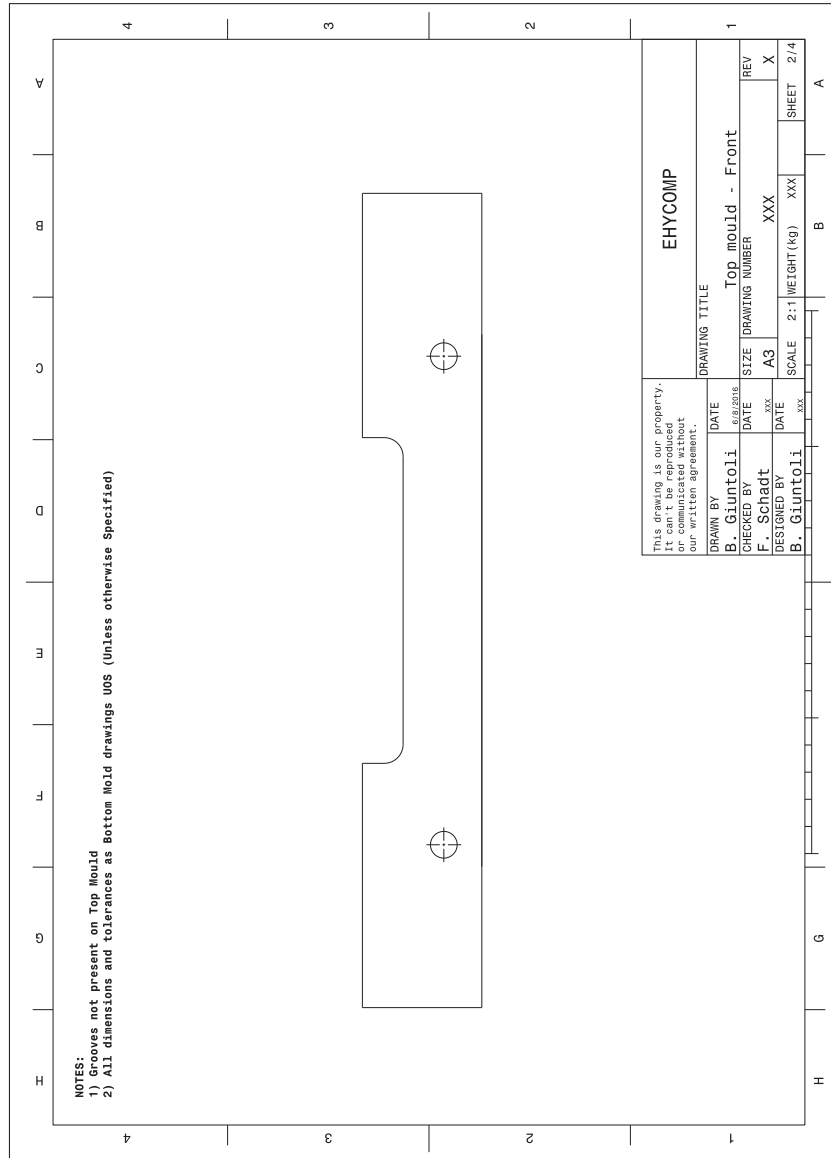
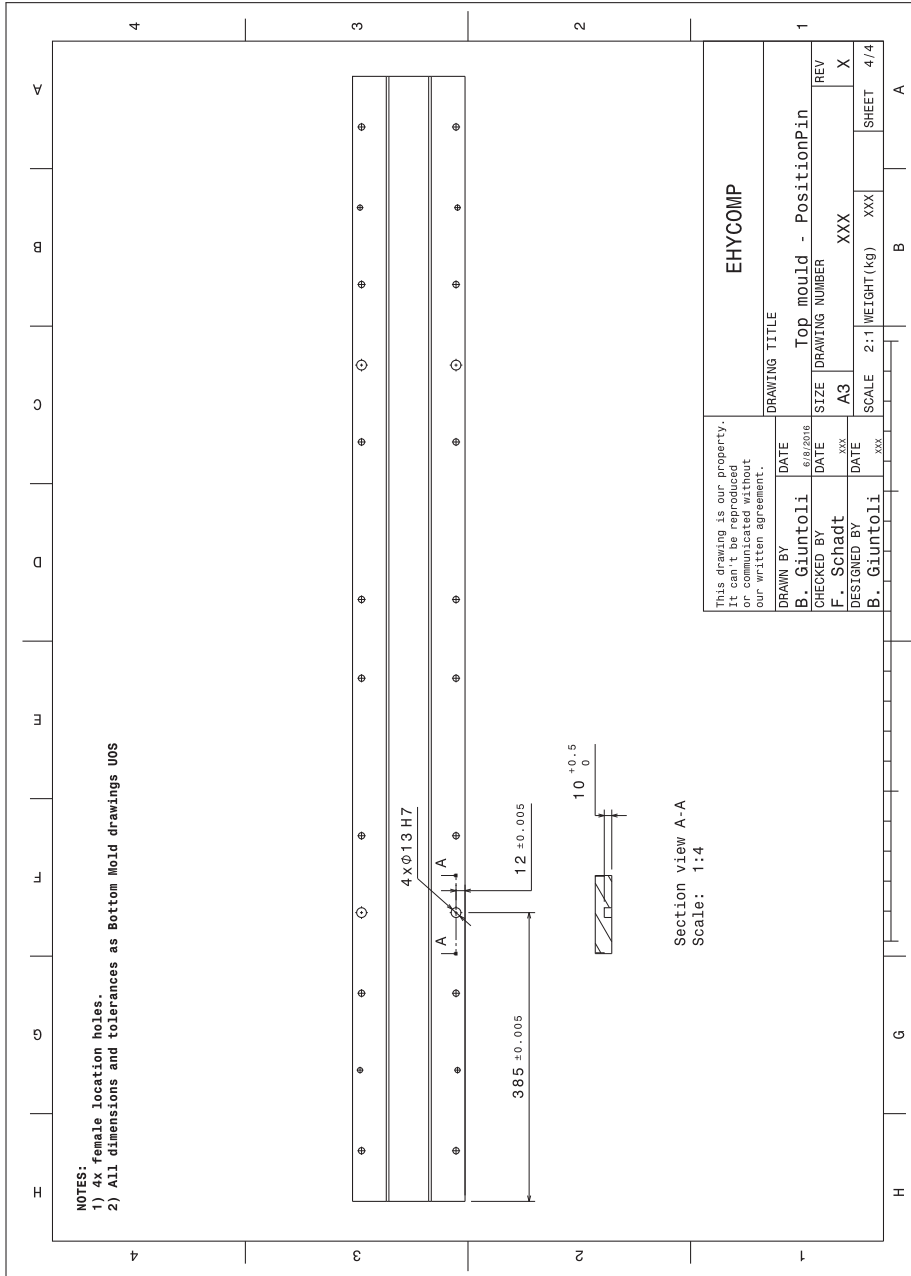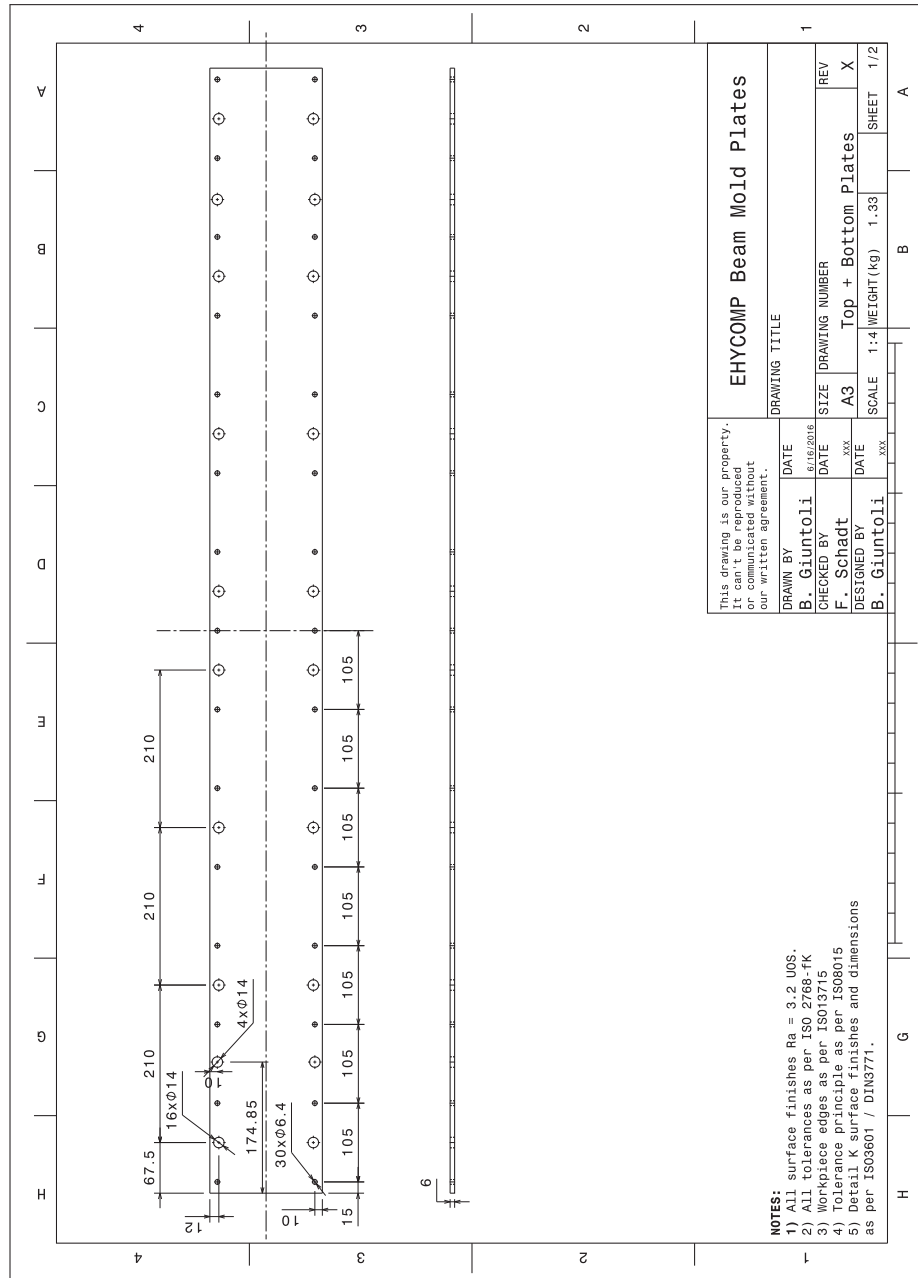Figure-A II-9　Top Side front view

126

Figure-A II-10   Top Side holes

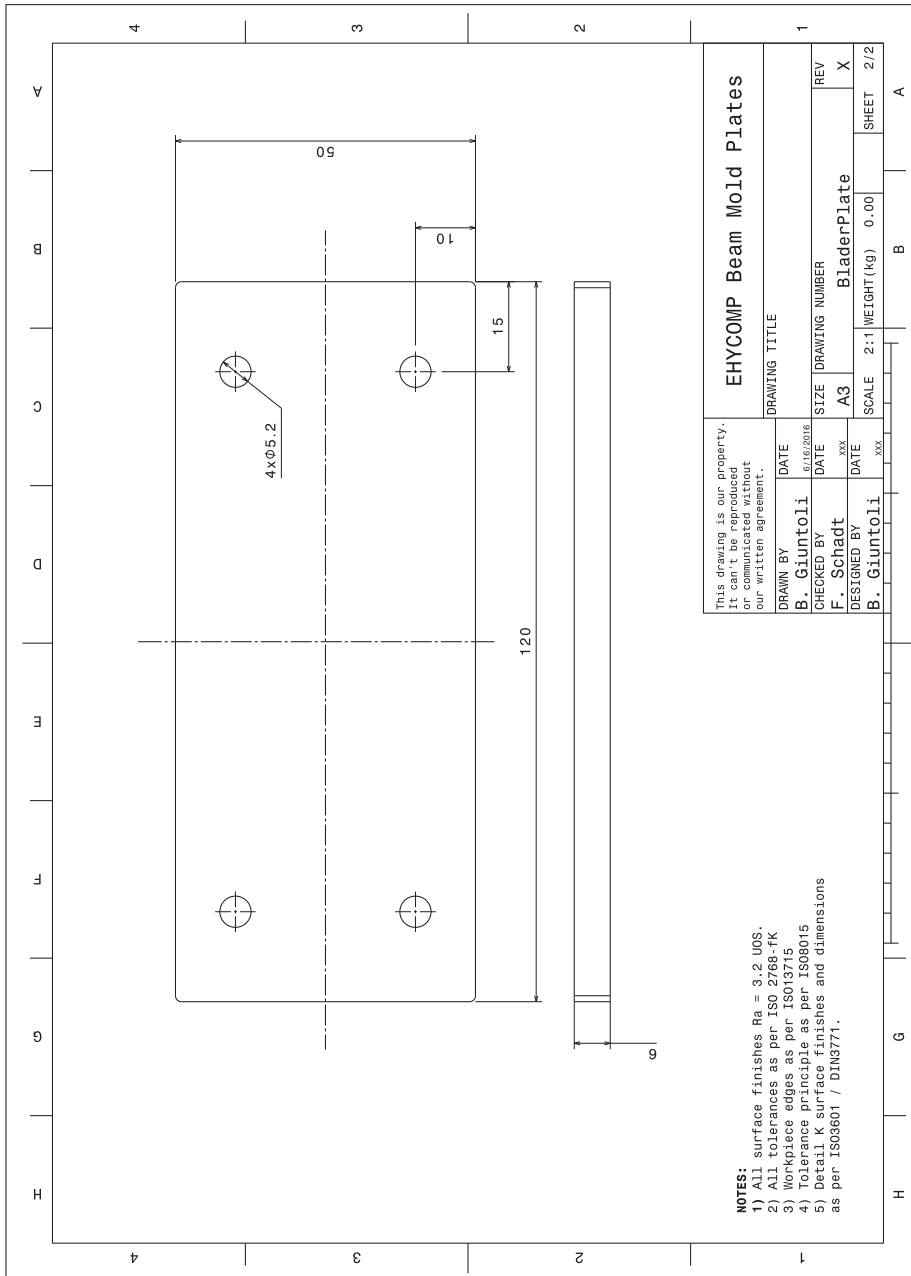Figure-A II-11   Channel Closing plate for Top and Bottom side heating

128

Figure-A II-12   Front and Back Mold Closing plate

WATER PHASES

Figure-A III-1   Water phases diagram. Source: Wikipedia

APPENDIX IV

NON-LINEAR BEAM EI TOOL CALCULATION MATRIX

Kx	Fxyz	Mxyz	GeoAng	GeoAngAbs	Fx	Fy	Mz	StrMax	StrSim	StrTol
1.8473e+04	[0,34.6536,0]	[0,0,0]	0.8200	0.8200	−893.9011	849.8605	773.5219	0.3000	0.3140	0.0750
1.7404e+04	[0,44.3337,0]	[0,0,0]	1.0700	1.8900	−844.8507	865.9381	690.2686	0.3000	0.2975	0.0750
1.4407e+04	[0,53.0563,0]	[0,0,0]	0.6300	2.5200	−800.0945	865.2488	605.8914	0.3000	0.3154	0.0750
1.2540e+04	[0,65.4960,0]	[0,0,0]	2.2400	4.7600	−731.9961	874.0649	522.0194	0.3000	0.3122	0.0750
1.1406e+04	[0,91.2051,0]	[0,0,0]	2.0600	6.8200	−669.9177	860.7044	437.8877	0.3000	0.2879	0.0750
8.4773e+03	[0,124.4623,0]	[0,0,0]	10.2500	17.0700	−485.0040	897.6024	356.3775	0.3000	0.3153	0.0750
1.0197e+04	[0,146.4435,0]	[0,0,0]	12.9900	30.0600	−275.6271	870.0598	272.8404	0.2000	0.2007	0.0750
6.8261e+03	[0,159.1950,0]	[0,0,0]	8.8500	38.9100	−139.5247	761.6585	193.1566	0.2000	0.2122	0.0750
5.0291e+03	[0,162.9103,0]	[0,0,0]	6.0600	44.9700	−59.8705	615.5038	124.9505	0.2000	0.1863	0.0750
2.7722e+03	[0,158.0111,0]	[0,0,0]	2.6000	47.5700	−27.5272	455.7056	71.5456	0.2000	0.1936	0.0750
1.2813e+03	[0,145.0820,0]	[0,0,0]	2.3400	49.9100	−7.4514	298.8716	33.8756	0.2000	0.1983	0.0750
1.0721e+03	[0,118.5298,0]	[0,0,0]	2.2000	52.1100	−0.0069	153.9700	11.2425	0.1000	0.0748	0.0750
1.0721e+03	[0,35.4403,0]	[0,0,0]	0	52.1100	5.9998e−13	35.4403	1.7720	0.1000	0.0015	0.0750

Figure-A IV-1   Non-Linear Beam EI Tool matrix results for 12kt. load-case

Kx	Fxyz	Mxyz	GeoAng	GeoAngAbs	Fx	Fy	Mz	StrMax	StrSim	StrTol
2.0950e+04	[0,0,0]	[0,0,0]	0.8200	0.8200	−1.6185e+03	19.5232	798.7263	0.3000	0.2859	0.0750
2.0934e+04	[0,0,0]	[0,0,0]	1.0700	1.8900	−1.6148e+03	111.2698	796.7739	0.3000	0.2855	0.0750
2.0126e+04	[0,0,0]	[0,0,0]	0.6300	2.5200	−1.6072e+03	191.8870	785.6470	0.3000	0.2928	0.0750
1.9495e+04	[0,0,0]	[0,0,0]	2.2400	4.7600	−1.5872e+03	317.1894	766.4583	0.3000	0.2949	0.0750
1.9131e+04	[0,0,0]	[0,0,0]	2.0600	6.8200	−1.5593e+03	434.2274	734.7393	0.3000	0.2880	0.0750
1.6979e+04	[0,0,0]	[0,0,0]	10.2500	17.0700	−1.4272e+03	763.4863	691.3166	0.3000	0.3054	0.0750
2.3375e+04	[0,0,0]	[0,0,0]	12.9900	30.0600	−1.1906e+03	1.0965e+03	614.9680	0.2000	0.1973	0.0750
1.9292e+04	[0,159.1950,0]	[0,0,0]	8.8500	38.9100	−974.2577	1.2925e+03	505.3221	0.2000	0.1965	0.0750
1.4673e+03	[0,162.9103,0]	[0,0,0]	6.0600	44.9700	0	3.9255e−15	384.0276	2	1.9629	0.0750
962.7696	[0,242.7423,0]	[0,0,0]	2.6000	47.5700	−103.0459	1.3383e+03	251.4031	2	1.9584	0.0750
5.1789e+03	[0,496.7380,0]	[0,0,0]	2.3400	49.9100	−30.6939	1.0999e+03	129.7151	0.2000	0.1879	0.0750
3.6063e+03	[0,460.3362,0]	[0,0,0]	2.2000	52.1100	−0.0541	603.9593	44.5603	0.1000	0.0927	0.0750
1.8847e+04	[0,143.6232,0]	[0,0,0]	0	52.1100	−2.3066e−13	143.6232	7.1812	0.1000	0.0028	0.0750

Figure-A IV-2   Non-Linear Beam EI Tool matrix results for 24kt. load-case

BIBLIOGRAPHY

3DS-Simulia. (2013). *Abaqus 6.13 documentation*. Dassault Systems.

Arrieta, A. F., Kuder, I. K., Rist, M., Waeber, T. & Ermanni, P. (2014). Passive load alleviation aerofoil concept with variable stiffness multi-stable composites. *Composite structures*, 116, 235 - 242. doi: http://dx.doi.org/10.1016/j.compstruct.2014.05.016.

Barbarino, S., Flores, E. I. S., Ajaj, R. M., Dayyani, I. & Friswell, M. I. (2014). A review on shape memory alloys with applications to morphing aircraft. *Smart materials and structures*, 23(6), 063001. Consulted at http://stacks.iop.org/0964-1726/23/i=6/a=063001.

Brailovski, V., Terriault, P., Georges, T. & Coutu, D. (2010). *Sma actuators for morphing wings*. doi: http://dx.doi.org/10.1016/j.phpro.2010.11.098.

Chamis, C. C. & Murthy, P. L. N. (1988). *Design procedures for fiber composite box beams* (ed. 1). United States: National Aeronautics and Space Administration (NASA).

Chudnovsky, V., Kennedy, D. & Mukherjee, A. (2006). Modeling flexible bodies in simmechanics and simulink. Consulted at https://ch.mathworks.com/.

Cismasiu, C. (2010). *Shape memory alloys*. Rijeka, Crotia: Sciyo.

Coda, A., Fumagalli, L. & Butera, F. (2009, 2). Smartflex niti wires for shape memory actuators. *State-of-the-art research and application of smas technologies*, 59(Advances in Science and Technology), 198–206. doi: 10.4028/www.scientific.net/AST.59.198.

Dado, M. & Al-Sadder, S. (2005). A new technique for large deflection analysis of nonprismatic cantilever beams. *Mechanics research communications*, 32(6), 692 - 703. doi: http://dx.doi.org/10.1016/j.mechrescom.2005.01.004.

F, B. & Jr., J. R. (2011). *Statics and Mechanics of Materials* (ed. 1). McGraw-Hill Education.

Gibson, R. (2012). *Principles of composite material mechanics* (ed. 3). Boca Raton, Fla: Taylor & Francis.

Holierhoek, J. G. (2007, January). Rigid Body Modeling of Wind Turbines for Aeroelastic Stability. doi: 10.2514/6.2007-210.

ISAF. (2010). International A Class Catamaran Rules. [Online; accessed 10-September-2015], Consulted at http://a-cat.org/.

Kimball, J. (2010). *Physics of sailing*. Boca Raton, Fla. London: CRC Taylor & Francis distributor.

Kollar, L. & Springer, G. (2003). *Mechanics of composite structures*. Cambridge New York: Cambridge University Press.

Kuder, I. K., Fasel, U., Ermanni, P. & Arrieta, A. F. (2016). Concurrent design of a morphing aerofoil with variable stiffness bi-stable laminates. *Smart materials and structures*, 25(11), 115001. Consulted at http://stacks.iop.org/0964-1726/25/i=11/a=115001.

Larsson, L., Eliasson, R. & Orych, M. (2013). *The principles of yacht design, 2nd ed.* McGraw-Hill.

Molenaar, D. P. (2003). *Cost-effective design and operation of variable speed wind turbines : closing the gap between the control engineering and the wind engineering community*. (Ph. D. thesis, Delft, the Netherlands).

Quintanilla, A. (2016). *Development of a fast shape memory alloy based actuator for morphing airfoils*. (Ph. D. thesis, Delft).

Rao, A. (2015). *Design of shape memory alloy (sma) actuators*. Cham: Springer.

Reddy, J. N. (1993). *An introduction to finite element methods* (ed. 3). Texas A and M University, College Station, Texas, USA 77843: McGraw-Hill Higher Education.

Runkel, F., Reber, A., Molinari, G., Arrieta, A. & Ermanni, P. (2016). Passive twisting of composite beam structures by elastic instabilities. *Composite structures*, 147, 274 - 285. doi: http://dx.doi.org/10.1016/j.compstruct.2016.02.080.

Schadt, F. (2016). Efficient hydrofoils with non-linear compliance - reference beams with non-linear compliance.

Schürmann, H. (2007). *Konstruieren mit faser-kunststoff-verbunden : mit 39 tabellen*. Berlin HeidelbergNew York, NY: Springer.

Sofla, A., Meguid, S., Tan, K. & Yeo, W. (2010). Shape morphing of aircraft wing: Status and challenges. *Materials and design*, 31(3), 1284 - 1292. doi: http://dx.doi.org/10.1016/j.matdes.2009.09.011.

Swanson, S. R. (1997). *Introduction to design and analysis with advanced composite materials*. Upper Saddle River, N.J: Prentice Hall.

Weinert, K. & Petzoldt, V. (2004). Machining of niti based shape memory alloys. *Materials science and engineering: A*, 378(1), 180 - 184. doi: http://dx.doi.org/10.1016/j.msea.2003.10.344. European Symposium on Martensitic Transformation and Shape-Memory.

Ziolkowski, A. (2015). *Pseudoelasticity of shape memory alloys : theory and experimental studies*. Oxford, UK: Butterworth-Heinemann is an imprint of Elsevier.